Architectures and System Design for Digitally-Enhanced Antenna Arrays

by

James David Stone Krieger

B.S., University of California at Santa Barbara (2000)
M.S., The Ohio State University (2005)

Submitted to the Department of Electrical Engineering and Computer Science
in partial fulfillment of the requirements for the degree of

Doctor of Philosophy in Electrical Engineering and Computer Science

at the

MASSACHUSETTS INSTITUTE OF TECHNOLOGY

February 2014

Author ....
Department of Electrical Engineering and Computer Science
October 28, 2013

Certified by ....
Gregory W. Wornell
Professor of Electrical Engineering and Computer Science
Thesis Supervisor

Accepted by ....
Leslie A. Kolodziejski
Chair, Committee on Graduate Students

Architectures and System Design for Digitally-Enhanced Antenna Arrays
by
James David Stone Krieger

Submitted to the Department of Electrical Engineering and Computer Science
on October 28, 2013, in partial fulfillment of the
requirements for the degree of
Doctor of Philosophy in Electrical Engineering and Computer Science

Abstract

Digital techniques have had longstanding use in both the operational control and signal processing efforts associated with phased array antennas. Fundamentally, these techniques have served to provide additional levels of convenience and performance over the fully analog counterparts, without specifically addressing the underlying design of the analog hardware aspects of the arrays. The class of digitally-enhanced hardware has recently emerged, wherein “digitally aware” design approaches are used for the purpose of alleviating the high cost and complexity of sophisticated analog devices.

Emergent trends in millimeter wave and low-terahertz circuit technology are enabling the prospect of physically small, yet electrically large antenna arrays for a host of exciting new communication, radar, and imaging applications. Still, the high cost of phased arrays remains a significant bottleneck to any widespread deployment in this regard. In light of this challenge, we propose two phased array architectures for which the notion of digital awareness plays a central role in their designs.

The Dense Delta-Sigma Array: Primarily motivated by advancements in low-cost fabrication, this design concept provides the opportunity to replace the expensive RF components required to control the individual array element excitations with inexpensive phase shifter components having particularly coarse resolution (as few as 2-bits). This is made possible by increasing the number of array elements for a given aperture beyond the nominal number associated with the standard half-wavelength spacing. This approach is inspired by Delta-Sigma data converters, which employ faster-than-Nyquist sampling with low quantization resolution.

The Sparse Multi-Coset Array: This design concept exploits the sparsity commonly found in typical environments to allow for target detection and imaging with significantly fewer array elements than prescribed by conventional half-wavelength spacing. The result is a structured periodic non-uniform array composed of a number of distinct subarrays known as cosets. This approach is inspired by multi-coset sampling, for which the average sampling rate may be reduced below the Nyquist convention when the spectral components within the overall bandwidth are limited to some number of sub-bands. In this approach, we view the underlying engineering design problem as one of compressive sensing.

In this thesis, we develop and apply the underlying mathematical principles and concepts of the dense and sparse arrays, taking into account the practical constraints and issues that make the system design, analysis, and performance evaluation rich from an engineering perspective.

Thesis Supervisor: Gregory W. Wornell
Title: Professor of Electrical Engineering and Computer Science

Acknowledgments

My time at MIT has been a life changing experience, and I owe many thanks to many people. Nearly every interaction I have had during my time here—from the courses I have taken to the group meetings and seminars to the numerous individual conversations—has left me feeling a little more complete.

I am particularly grateful to have had Greg Wornell as my adviser. I consistently found myself challenged in our research, and as I finish my time here I feel as though his guidance and direction have laid a foundation for a new way of thinking that I have only begun to explore. Plus, as large of a challenge as it must have been on his end, he always managed to keep me pushing forward when I felt like I didn't have it in me. Truly, thank you so much for everything.

I also want to thank my wonderful thesis committee: Charlie Sodini, Yuval Kochman, and Alan Fenn. Each of you brought unique insights and perspectives and I am all the better for it. I hope our paths continue to remain close for a long time.

MIT Lincoln Laboratory played a huge role in getting me to this point. I thank the Lincoln Scholars Committee for making all of this possible, Jeff Herd and Helen Kim for all of their support and guidance, and Leonard Parad. Extra special thanks to Dave Bruno and Glenn Brigham for making the experimental portions of this thesis possible.

It was a great experience getting to work with all of the present and past members of the Signals, Information, and Algorithms group, especially my on-again, off-again office-mate Da Wang, who put up with my endless questions about all manners of things. I particularly want to thank Tricia O'Donell and Janet Fischer for all their help with so much.

And of course, my love and thanks to my wonderful family: my fancy siblings Leah, Brian, and Ross; my dearest mother, Mum; and my Papa for being such a huge support during these past few months, always reminding me to breathe and telling me to "go do my homework". I love you all!

This work was supported in part by DARPA under Contract No. HR0011-06-1-0004, by the Semiconductor Research Corporation through the FCRP Center for Circuit and System Solutions (C2S2), and by the Department of the Air Force under Air Force Contract No. FA8721-05-C-0002. Opinions, interpretations, conclusions and recommendations are those of the authors and are not necessarily endorsed by the United States Government.

Contents

List of Figures

List of Tables

Chapter 1

Introduction

Digital techniques play a prominent role in nearly all modern phased array systems, enriching both their operational and signal processing capabilities in ways beyond the possibility of the original analog designs. The implementation of digital control over the amplitudes and phases of the array element weights permits the rapid electronic reconfiguration of the array pattern characteristics. The many developments in digital array processing have yielded numerous additional tools for the extraction of useful information that would be impossible or far less practical to implement through fully analog designs.

While these digital approaches complement the phased array system in a number of ways, these systems still rely on conventional front-end designs having a high level of precision in the complex signal weights at each of the individual elements. Put another way, while the algorithmic design must account for the specifics of the analog design, the array is designed without regard for the digital aspects of the system.

Recently, there has been an emergence of digitally-enhanced hardware designs motivated by the desire to bridge the gap to cooperative design approaches that emphasize a level of awareness regarding the utilization of digital techniques such that the requirements for analog device complexity can be relaxed. The existing integration of digital system blocks so common in phased arrays makes them natural candidates for such enhanced techniques. Further, as advances in circuit technologies at increasingly higher frequencies surface, new frontiers for the use of phased arrays become reality. Yet with the existing design conventions, the phased array is normally considered to be a prohibitively costly and complex antenna option, emphasizing the pressing need for a shift in perspective in order to address the challenges of making their widespread use a possibility. As such, this thesis presents two alternative phased array architectures that use digital perspectives in both design and operation. In both cases, the architecture moves beyond conventional design principles in a way that provides new opportunities for cost reductions while avoiding the limitations common to existing array design techniques.

1.1 Motivation

Since the development of phased array antennas, they have been the ideal choice for a vast range of applications ranging from point-to-point communication to remote sensing and more recently, to high resolution imaging systems, to name just a few. Unfortunately, the same design features that allow the performance and flexibility characteristics that make phased arrays desirable come at such high costs as to preclude their use in all but a relatively small number of highly sophisticated systems. Research efforts promoting the evolution of phased array designs aimed at overcoming this issue have been limited for several decades, resulting in a general acceptance of the impracticality of a more pervasive presence. However, as we look to the future, it becomes increasingly clear that the need to meet these design challenges must be acknowledged.

Recent advances in technology at the millimeter-wave and the low terahertz frequency ranges—in both the development of circuitry as well as lithography at these scales—has enabled the potential for a new generation of portable high-end and consumer electronics. Although size and fabrication issues are more manageable than ever before, the costs associated with the circuitry required for element level control remains a significant bottleneck to making this a reality. Though the goal of designing low-cost phased arrays is longstanding, these new possibilities motivate the need for novel perspectives.

1.2 Research Philosophy

Historically, the attempts in making the phased arrays more affordable have involved adjusting hardware designs. More recently, there has been growing interest in the design of "digitally enhanced" analog circuits to leverage digital techniques and the increasing availability of low-cost processing power to alleviate the need for high precision, high complexity analog blocks; see, e.g., [1] and references therein. This philosophy inspires the two novel array architectures that are the focus of this thesis.

Dense Delta-Sigma Phased Array

The most common of phased array designs use digital phase shifters at each element. A phase shifter having M-bits of resolution can be used to adjust the phase at an individual element by one of 2^M levels, with the exact shift implemented digitally by a dedicated processor. For a given beam pattern, this processor determines the ideal phase shift to be applied for each element, and then selects the nearest *quantized* phase shift from the available 2^M levels. Consequently, the level of quantization distortion in the overall array pattern increases as the precision of the phase shifters decrease. As such, most phased arrays use a minimum of 4- or 5-bits of resolution in order to keep this distortion at acceptably low levels.

The Delta-Sigma ($\Delta\Sigma$) phased array differs from conventional designs in three primary ways. Unlike conventional array designs, in which the elements are uniformly spaced by a distance $d_0 = \lambda/2$, where λ is the operating wavelength of the array, the $\Delta\Sigma$ array is *dense*: a greater number of elements are packed into a given aperture such that the uniform spacing is $d < d_0$. Instead of the high-precision components used to set the amplitude and phase adjustments to the signals at the array elements, or array weights, the $\Delta\Sigma$ array uses only 2-bit phase shifters, limiting the weights to only four possible values. The selection of the appropriate quantized phase shift no longer selects the "closest value" to the ideal phase shift.

It is well known from conventional array theory that this dense element spacing does not add to the array performance in the case of ideal weights. However, in practical settings where the array weights are quantized, this close element spacing affords additional flexibility in controlling the amount of distortion caused by this quantization. By making use of the digitally controlled analog architecture, the availability of inexpensive processing power is used to account for the effects of quantization by selecting the weights in a manner

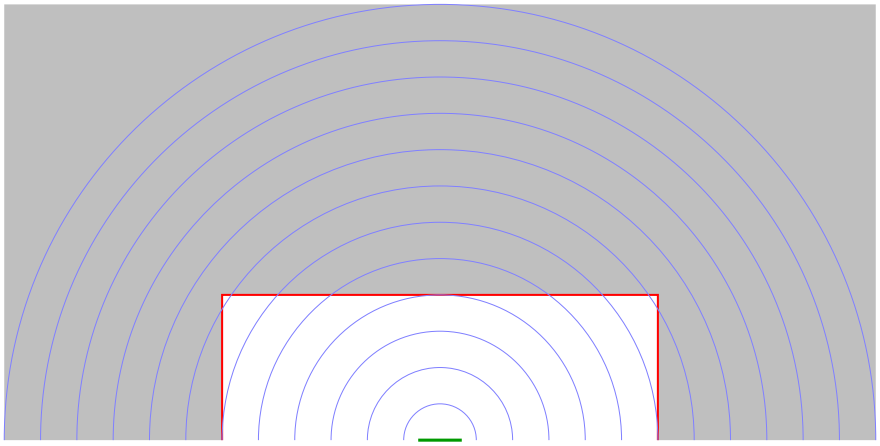

Figure 1-1: Illustration of range-dependent sparsity.

that uses neighboring elements to cancel out distortion. As the distance between the elements decreases, the effectiveness of this cancellation technique improves. As we will see, the distortion caused by the use of the 2-bit phase shifters can be made arbitrarily small.

Sparse Multi-Coset Imaging Array

In a traditional linear imaging array, when the elements are arranged with uniform element spacing $d_0 = \lambda/2$, where λ is the wavelength of the received signal, the image resolution improves in direct proportion to the number of elements N_0. In the multi-coset imaging array, the same aperture length $N_0 d_0$ uses $N < N_0$ elements to produce an image at the same resolution as the conventional imaging array. When fewer than N_0 elements are uniformly spaced by $d > d_0$, this leads to spatial aliasing, or grating lobes, producing images with copies of the targets appearing at additional incorrect locations. In the multi-coset array, the elements are positioned in a recurrent nonuniform arrangement in such a manner that the presence of such grating lobes can be avoided.

The ability to obtain the correct image using a reduced number of elements is based on the observation that target scenes are themselves sparse in most cases. That is, the image will contain a certain number of locations that are empty of any targets. While this is not necessarily the case when considering the fraction of directions in which targets are located, the existence of scene sparsity is apparent when one considers the ability to distinguish the distance to targets by sorting their responses into a number of range cells. In light of this, scene sparsity can be regarded as the portion of directions occupied by targets within each range cell. As a simple example, Figure 1-1 illustrates this effect. In the illustration, the array, shown in green, faces a large object, shown in grey, with the faces shown in red representing the surface of this object in the field of view of the array. The complete surface surrounds the array such that the scene taken as a whole exhibits no sparsity whatsoever. However, if the scene is sorted into separate range cells, as shown by the concentric blue half-circles, it is only the intersection of the red surface with the individual cells that defines the relevant level of sparsity.

The multi-coset architecture permits a reduction in the required number of elements to an array density ratio N/N_0 provided this relative density remains above the scene density over all range cells. Rather than using conventional imaging—a digital implementation of analog beamforming—the digital processing is enhanced through the use of an imaging algorithm that first examines the received signal data to determine the angular regions in which targets are located, and then utilizes the knowledge of this reduced angular subspace to solve for the image response within this region.

1.3 Related Work

This research builds on a number of contributions from a range of communities. In this section, we summarize some of the related works from the fields of antenna theory, signal processing, circuit design, and compressive sensing to provide context for the contributions of this thesis.

Cost Effective Array Designs and Delta-Sigma Applications

The developments in millimeter-wave technology have led to a resurgence of interest in practical phased array designs tailored to this new frequency regime; see, e.g., [2–7] and the references therein. Within the broader realm of ongoing research, some efforts are focused primarily on exploiting increasing levels of silicon integration, while other efforts primarily seek to exploit the increasing availability of inexpensive digital circuitry and processing. Moreover, some of the most promising efforts leverage both jointly.

In spite of recent progress, the components required for accurate phase control at each element in such arrays continue to be expensive, precluding the use of phased arrays in many otherwise compelling applications. Simply replacing high-end, high-resolution components with low-cost, coarsely discretized phase shifters in traditional designs sharply degrades performance, limiting the quality of the beams that can be formed by the array. As a result, addressing the need for adequate phase control in beamforming remains a key challenge in the pursuit of widespread deployment of millimeter-wave phased arrays.

There has been a variety of research exploring this issue. For example, some research has focused on characterizing the capabilities of phased array systems utilizing low resolution phase shifters to meet the needs of current and proposed millimeter-wave applications [8,9]. At the same time, other research has focused on developing novel approaches for sharing a smaller number of phase shifters (and other components) among antenna elements [10].

In this design, we explore a rather different approach. Specifically, instead of pursuing designs with a smaller number of accurate phase shifters, we develop a high-performance architecture based on efficient utilization of a larger number of coarse phase shifters. To accomplish this, we repurpose the established theory of delta-sigma analog-to-digital converters (ADCs) [11], applying it in the spatial domain to determine an appropriate phase for each of the densely packed elements to create a desired array pattern. In temporal domain $\Delta\Sigma$ as used in ADCs, coarsely discretized faster-than-Nyquist sampling, or *oversampling*, is used to force the quantization error to appear at higher frequencies than the original signal. This, in turn, allows the original signal to be retrieved by low-pass filtering, removing the undesired error. Exploiting a direct correspondence between temporal domain and spatial domain sampling, we observe that faster-than-Nyquist sampling in ADCs is the equivalent of sub-half-wavelength element spacing in uniform arrays. Moreover, the shaping of quantization noise into the high frequencies in ADCs is equivalent to the steering of beam pattern quantization error into the so-called invisible region of space, while leaving the intended pattern throughout the (visible) area of interest.

From a broader perspective, our architecture can be viewed as exploring potential attractive technology tradeoffs enabled by inexpensive digital processing. In particular, the architecture allows for making tradeoffs between phase shifter design complexity and denser antenna implementations. And with ongoing evolutions in antenna fabrication and integration technology, such tradeoffs may turn out to be quite favorable. For example, using modern lithography there is the potential to etch cost-effective dense arrays of patch antennas antennas, which with increasing levels of density effectively become simple printed dipoles. From this perspective, the $\Delta\Sigma$ architecture represents a generalization of the traditional phased array architecture that allows a designer, with specific implementation technology at his/her disposal, to choose from a spectrum of tradeoffs between array density on one hand, and analog circuit complexity on the other.

The $\Delta\Sigma$ data encoding process continues to be adapted for use in a growing number of fields and applications that exploit oversampling in the temporal domain in order to mitigate noise while using relatively simple sensors for measurement; see, e.g., [12–14]. Additionally, $\Delta\Sigma$ techniques have been applied to phased arrays and imaging arrays in a number of instances; see, e.g., [15–18]. However, these techniques have focused on the use of $\Delta\Sigma$ techniques in the more traditional temporal domain for such arrays, in contrast with our focus on exploiting spatial oversampling.

Spatial domain versions of $\Delta\Sigma$ have received attention in applications other than antenna array design; examples include image processing, wave computing, and pattern recognition [19, 20]. For instance, in the context of image processing, an approach known as error diffusion uses $\Delta\Sigma$ quantization to reproduce images from low-resolution but oversampled data. However, these methods are in the same spirit as the traditional application of $\Delta\Sigma$ principles in the temporal domain. In particular, they apply it to the data itself, whereas in our approach it is applied to the actual sensors/transducers, i.e., the antenna elements. Finally, in [21], a spatio-temporal $\Delta\Sigma$ quantization scheme is developed for transmit antenna arrays. While there are some superficial similarities to the methods described in this thesis, the goals are quite different, and how the $\Delta\Sigma$ methodology is exploited diverges sharply. In particular, whereas the architecture in [21] aims to reduce the temporal oversampling requirements of the time domain waveforms, ours seeks to produce specified antenna beam patterns with simpler structure and hardware.

Array Thinning and Multi-Coset Sampling

Recent advances in millimeter-wave technology, including the advent of terahertz complementary metal-oxide semiconductor (CMOS) circuits, have the potential to enable, for the first time, a host of low-cost imaging and “personal radar” applications. Indeed, at these higher frequencies, typical resolution requirements can be met with comparatively compact arrays, which are especially attractive for applications requiring some degree of mobility. Moreover, such arrays can be implemented with inexpensive integrated circuit and antenna technologies, and digital implementations.

However, with such technology comes significant new challenges, an important example of which is the large number of array elements typically required to construct a phased array in such applications. As an illustration, in a vehicle collision avoidance system, obtaining sufficient resolution might require an aperture of roughly 2 m. But in this case a traditional phased array operating at 100 GHz with half-wavelength element spacing would require roughly 1000 antennas, which is daunting to implement. Indeed, such arrays are costly and complex to design and calibrate, and, moreoever, since the system processing requirements scale in proportion to the number of elements, the needed computational bandwidth quickly becomes impractically large.

As a result, there is renewed interest in developing sparse antenna array architectures. Sparse arrays, characterized by average inter-element spacings of greater than one half of the operating wavelength, have been of interest throughout much of the history of phased arrays, garnering a great deal of attention in the early 1960's; see, e.g., [22] and references therein.

The design of general-purpose sparse arrays has typically entailed making basic performance tradeoffs. A well-known example is the use of "density tapering," which uses a gradually increasing spacing profile as one moves from the center toward the edges of the aperture. These arrays are representative of a class of "thinned" arrays that stretch the aperture associated with a given number of elements to achieve a desired resolution by narrowing the width of the main lobe without introducing additional grating lobes. However, this is obtained at the cost of a significant increase in the sidelobe level. In certain applications for which resolution is the key performance metric, these provide a useful design solution. However, in the context of imaging arrays this introduces an unacceptable noise floor.

Another class of sparse arrays, referred to as *limited scan* arrays, accommodate sparseness by constraining the field-of-view of the array to a commensurately narrow range of angles [23]. This may be accomplished through the use of lens or reflector systems designed to increase the directive properties of the array elements such that grating lobes are suppressed outside of the angular region of interest. However, such arrays must be rotated physically in order to provide wide angle coverage, requiring relatively static environments as well as increased mechanical complexity.

An extension of the limited scan array is seen in overlapped subarray antennas [24], in which the array elements are connected to multiple subarrays. Each subarray acts as an analog beamformer, suppressing signals outside of the desired sector. By connecting digital receivers to the subarrays, full coverage throughout the sector is accomplished in the digital domain. With this architecture, the number of required receivers decreases linearly with the size of the sector. In turn, full coverage can be achieved through a combination of element-level phase shifters and subarray-level digital receivers.

In this work, we take a different approach, whereby rather than constraining the functionality or performance of the array, we exploit structure in the scene being imaged. In particular, we seek to exploit sparsity in the scene to allow the number of antenna elements to be reduced, i.e., when the scene being imaged is sparse in an appropriate sense—even without knowing *where* it is sparse—then it is possible to commensurately reduce the number of elements in an imaging array. Moreover, such sparseness is quite common in typical applications.[1]

This approach also has a rich history. Consider, for example, the classical problem of direction-finding with multiple sources, for which the MUSIC algorithm [25], among others, was developed. In this case, it is possible to achieve high-resolution with relatively few antenna elements because of the sparse nature of the scene. Indeed, the number of elements required is typically on the order of the number of sources. Hence, the presence of structure in the environment allows the number of elements to be reduced.

---

[1] Note that in a typical scene while there are objects at some range in any particular direction, when we use enough bandwidth to sufficiently resolve range as well, we find significant sparseness in the range-azimuth plane.

For arrays containing just a few elements, the array design and image reconstruction can often be fairly straightforward and exploit classical techniques. However, for arrays of even a few dozen elements, such direct approaches quickly become computationally infeasible to design, and impractical to implement. As a result, there is a need to impose useful structure on the array to enable efficient design and processing.

There has been growing recent interest in nonuniform arrays with structure, and how such structure can be exploited by efficient array processing to support forms of sparse sensing; see, e.g., [26–32]. Ulimately, these developments leverage perspectives and techniques from the field of compressive sensing (CS) [33,34]. For example, the co-prime sampling technique in [28] develops a nonuniform design from a pair of uniform sparse samplers, allowing the exploitation of this underlying structure to enable efficient design and processing.

In our development, we focus on particular structured sparse antenna designs that are comparatively easy to design and for which efficient array processing algorithms can be developed to perform the image reconstruction. Specifically, we focus on "multi-coset" arrays, defined as comprising a collection of interleaved sparse uniform arrays such that the elements are laid out in a periodic nonuniform pattern over the aperture.

This special structure has important computational implications. In particular, as will become apparent, the complexity of the associated array processing for such arrays is effectively governed by the number of elements in one period of the array, not by the total number of elements—i.e., the complexity does not significantly depend on the number of periods of the pattern in the array. As a result, the practicality of our architecture is not limited to arrays consisting of only very small numbers of elements, as has historically often been the case with less judiciously structured nonuniform arrays. This array architecture, introduced in [26], follows from exploiting the close mathematical relationship between the problem of imaging from a discrete array, and that of reconstructing a bandlimited time-domain waveform from samples. Indeed, our architecture is the counterpart of multi-coset sampling [35].

1.4 Contributions and Thesis Structure

From a high level perspective, the translation to the spatial domain of the $\Delta\Sigma$ and multi-coset concepts results in a number of fundamental similarities in the analysis and development of the array designs. As the practical details of implementing these ideas into fully realized architectures are considered at a deeper level, the story diverges from that of the original time domain applications, highlighting important distinctions. The primary objectives of this research are to detail the repurposing of the underlying concepts and to create a framework to address the characteristics unique to phased array systems. To this end, the thesis is laid out as follows.

In Chapter 2 we describe the foundational array concepts related to the subsequent development of the design innovations in the proposed arrays. This includes a review of standard topics such as array patterns, beam scanning, and conventional design practices. Special attention is given to effects of mutual coupling on the formation of patterns and power efficiency due to the particular relevance of this topics to the densely populated $\Delta\Sigma$ array.

Chapter 3 begins the development of the $\Delta\Sigma$ array with an introduction of the notion of phase quantization in the excitation of array weights. Relating this to signal discretization in analog-to-digital converters, we extend the concept of $\Delta\Sigma$ ADCs to form the basis of the proposed design. Chapter 4 continues the development using the more evolved free excitation array model to include the effects of mutual coupling and power efficiency. Our analysis investigates the robustness of the $\Delta\Sigma$ beamforming technique under the potentially severe electromagnetic environment inherent to arrays of tightly packed elements. We then consider the effects of both the dense physical architecture as well as the $\Delta\Sigma$ quantization technique on the array efficiency, including the implementation of a scan impedance based matching network that provides the potential for wideband performance benefits compared with conventional designs. Then, in Chapter 5 we describe experimental measurements performed to validate the $\Delta\Sigma$ array development and analysis.

In Chapter 6 we switch our focus to the multi-coset array, describing the idea of beamforming in the context of image formation and defining the central concepts of how the sparsity and structure of the scene and array are characterized. This chapter details the two-stage image reconstruction algorithm for the sparse array, examines the specific manner in which the system is affected by noise, and introduces a computationally simple failure indication stage to the algorithm based on the concept of back projection error. Chapter 7 discusses the various considerations regarding the specific layout of the multi-coset array and presents a novel design technique shown to optimize the aggregate performance of the array in noisy environments. Following this design procedure, we use the idea of range-dependent sparsity alongside the combined reconstruction and failure detection algorithm, forming two dimensional images from synthesized radar data. Chapter 8 details the process of performing experimental measurements to demonstrate the robustness of our development in a practical setting.

Finally, in Chapter 9 we conclude with a discussion of our results and describe a number of interesting directions for future research.

Chapter 2

Conventional Phased Array Concepts

This chapter provides an overview of the basic characteristics of linear arrays needed for this thesis.

2.1 Linear Arrays of Isotropic Elements

Our development begins with the linear array geometry shown in Figure 2-1.

2.1.1 Array patterns

Consider N ideal isotropic elements arranged with uniform spacing d along the z axis as in Figure 2-1. For time-harmonic sources with angular frequency ω and associated free space wavelength λ, when the complex weights $\{w_n\}_{n=0}^{N-1}$ are applied to the array elements, the *beam pattern* in the direction given by $k_z = k\cos\theta$, where $k = 2\pi/\lambda$ is the spatial angular frequency of the waves and the angle θ is measured from the $+z$ axis, may be written as [36]

$$f(k_z) = \sum_{n=0}^{N-1} w_n e^{jnk_z d}. \tag{2.1}$$

The region of k_z-space corresponding to real values of θ, $\mathcal{V} = \{k_z : |k_z| \leq k\}$ is referred to as the *visible region*, or *real space*. Outside of this region, θ takes on purely imaginary values, and as such, $\mathcal{V}^\perp$ is referred to as *imaginary space*.

2.1.2 Beam scanning

The main beam is scanned to k_{z0} when a progressive phase shift across the array $\angle w_n = -nk_{z0}d$ coherently combines signals along this direction. Since the beam pattern is $2\pi/d$-periodic in k_z-space, the main beam direction may be uniquely specified for any k_{z0} in the alias-free region $\mathcal{V}_0 = \{k_z : |k_z| \leq \pi/d\}$. If $d > \pi/k$, $\mathcal{V}_0$ is a subset of $\mathcal{V}$, and it is possible to have an alias of the main beam within real space, known as a *grating lobe*.

The relative power density, or *power pattern*, of an array is given by $P(k_z) = |f(k_z)|^2$. For a transmitting array, this pattern represents the relative radiation intensity in the direction k_z. When a grating lobe is present in real space, a part of the power intended for

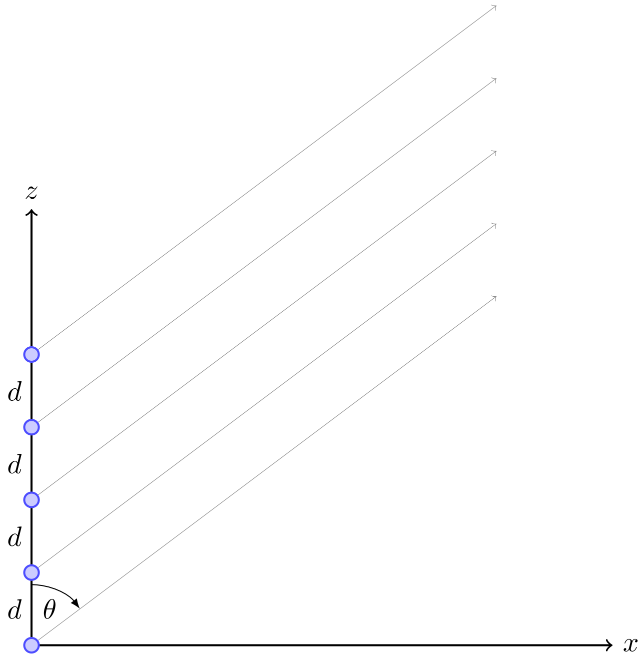

Figure 2-1: Uniform linear array geometry

the main lobe direction is instead transmitted to the grating lobe direction. For a receiving array, the power pattern gives the relative power gain of a signal arriving from k_z. With grating lobes, signals from unintended directions are amplified by the same level as the main lobe, leading to directional ambiguities and reduced signal-to-noise ratios.

An illustration of the effect of element spacing on the power pattern is shown in Figure 2-2 for uniform linear arrays of fixed length $L = 20\lambda$ scanned to $k_{z0} = k/2$ (at an angle of 30° from the broadside direction normal to the array). In each plot, a portion of imaginary space is shown to highlight the grating lobe behavior. For $d = \lambda/4$, the first main lobe alias lies well outside the visible region and does not appear within the displayed range of k_z. At a spacing of $d = \lambda/2$, we can see that the beam can be scanned nearly to the edge of the visible region before the first grating lobe begins to appear at the opposite edge. In the case of $d = \lambda$, an exact copy of the main lobe appears within $\mathcal{V}$ and we see that this is unavoidable at any scan angle k_{z0}.

As we see in Figure 2-2a, when $d < \pi/k$, $\mathcal{V}_0$ extends beyond the visible region. In this case, it is possible to scan the main lobe entirely outside of real space. In the transmit case, this has the physical interpretation that the array is attempting to direct power into imaginary space, and as a consequence very little power will actually propagate away from the array. The receiving array has an analogous interpretation: it is attempting to focus on signals coming from imaginary space, thus causing any signal from real space to be combined incoherently.

With no apparent benefit gained from choosing a particularly small element spacing, conventional array design generally dictates that the spacing be set at or just slightly less than $d_0 = \pi/k = \lambda/2$. Based on this convention, a linear array with aperture length $L = Nd$ is referred to as a standard uniform linear array when the number of elements is

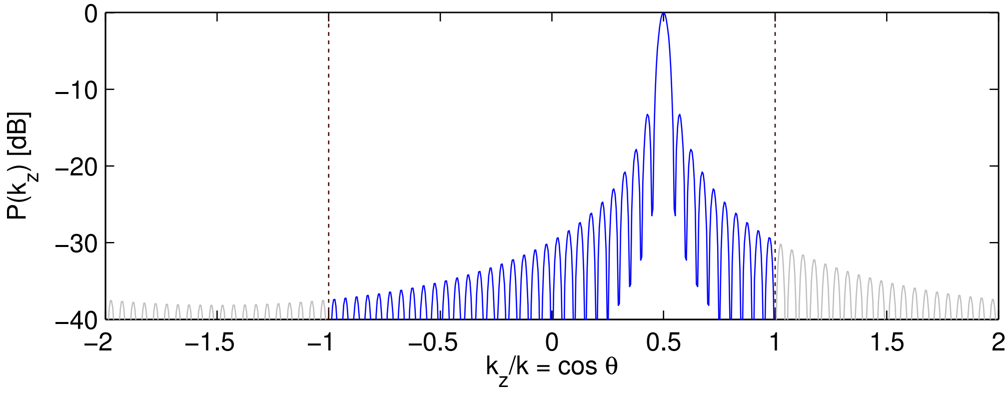

(a) $d = \frac{\lambda}{4} = \frac{\pi}{2k}$

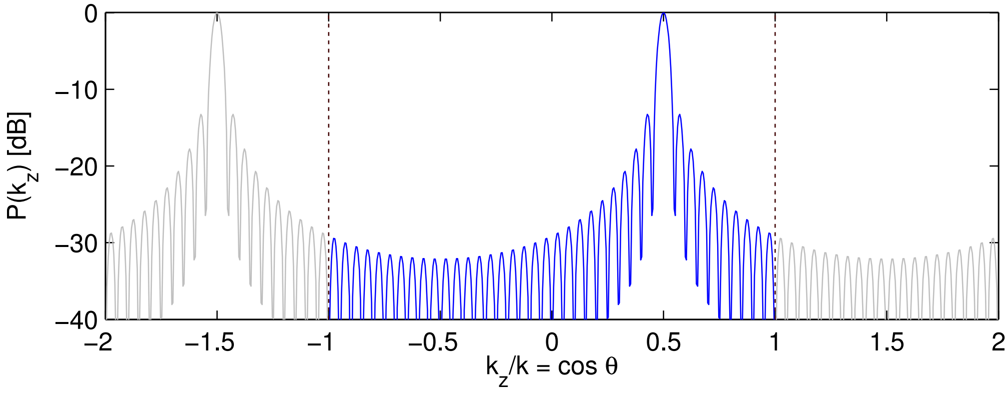

(b) $d = \frac{\lambda}{2} = \frac{\pi}{k}$

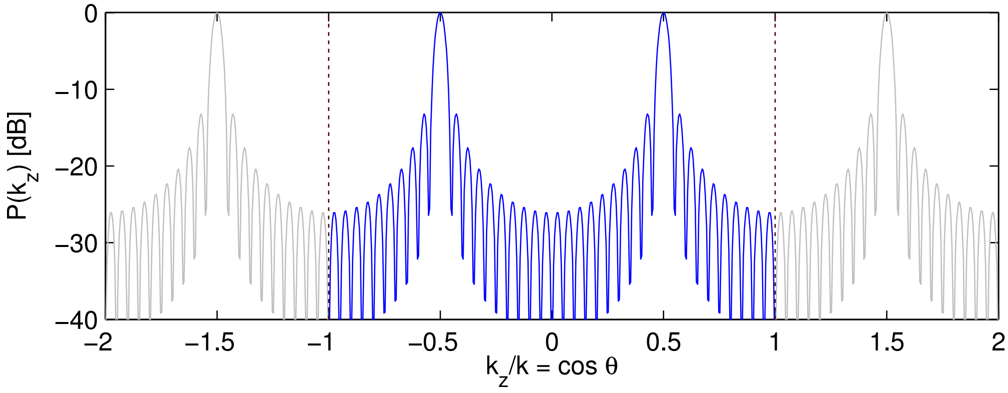

(c) $d = \lambda = \frac{2\pi}{k}$

Figure 2-2: Power patterns for $L = 20\lambda$ linear array scanned to $k_{z0} = k/2$. The edges of the visible region are marked with vertical dotted lines.

$N = N_0 = L/d_0$. When the same aperture is filled uniformly with more than N_0 elements, the resultant array is described as a dense array. As will be shown, while there is no benefit to using such an array with idealized components, a dense array has the potential to be useful for practical phased array implementation.

For our development, it is important to emphasize the distinction between the impacts of varying the array aperture size versus varying the number of array antennas, as these parameters are independently chosen in our architecture. To first order, the aperture size determines the fundamental pattern characteristics such as beamwidth and directivity. In a traditional array with element spacings near a half-wavelength, changing the aperture size is equivalent to changing the number of antennas. However, with the $\Delta\Sigma$ array architecture we focus on a fixed, but arbitrary array aperture within which the number of antennas is increased by reducing the element spacing throughout the aperture, resulting in a greater

2.2 Mutual Coupling

Physically, the array weights in (2.1) represent voltage or current excitations applied to the individual elements. For example, in an array of thin-wire dipoles, these weights are the currents across the terminals of the two dipole halves. Implicit in this expression for the beam pattern is the assumption of direct control over these terminal currents. This is known as the *forced excitation* model.

A more accurate representation of a practical array system is the *free excitation* model, characterized by the equivalent circuit shown in Figure 2-3. In this model, the weights $\{w_n\}$ represent the complex voltages generated by individual sources, each with internal impedance Z_0. The array is described as an N-port network with impedance matrix $\mathbf{Z} \in \mathbb{C}^{N \times N}$ such that $\mathbf{v} = \mathbf{Z}\mathbf{i}$ [37], where $\mathbf{v}$ and $\mathbf{i}$ are length-N vectors containing the voltages $\{v_n\}$ and currents $\{i_n\}$ at the terminals of the array elements. The terminal currents in Figure 2-3 are related to the weights $\mathbf{w} \in \mathbb{C}^N$ according to

$$\mathbf{w} = Z_0\mathbf{i} + \mathbf{v} = (Z_0\mathbf{I} + \mathbf{Z})\mathbf{i}, \tag{2.2}$$

where $\mathbf{I}$ is the $N \times N$ identity matrix. Defining the *coupling matrix* as $\mathbf{C} = (Z_0\mathbf{I} + \mathbf{Z})^{-1}$, such that $\mathbf{i} = \mathbf{C}\mathbf{w}$, the effects of the feed network and mutual coupling may be accounted for by replacing the w_n in (2.1) with $i_n = \sum_{m=0}^{N-1} C_{nm} w_m$. The resultant beam pattern with mutual coupling is then

$$f^{\mathrm{MC}}(k_z) = \sum_{n=0}^{N-1} \sum_{m=0}^{N-1} C_{nm} w_m e^{jnk_z d}. \tag{2.3}$$

The model described above is commonly used in traditional mutual coupling analysis—see, e.g., [38]. We may obtain a useful form for the purpose of our analysis by exploiting certain structure in the coupling. In particular, it is useful to express (2.3) in terms of the *embedded element patterns*, which are the patterns due to a unit excitation at a specified element while in the presence of the remaining array elements. While these will vary among the elements near the edges of the array, most elements behave similarly to the elements of an infinite array. In the infinite array model, the physical coupling environment is constant for all elements and as such, the coupling matrix $\mathbf{C}$ has a Toeplitz structure, with identical entries along each diagonal $c_p = C_{m+p,m}$. Thus, the complete coupling matrix may be represented by the set $\{c_p\}$, which we refer to as the infinite array *coupling coefficients*.

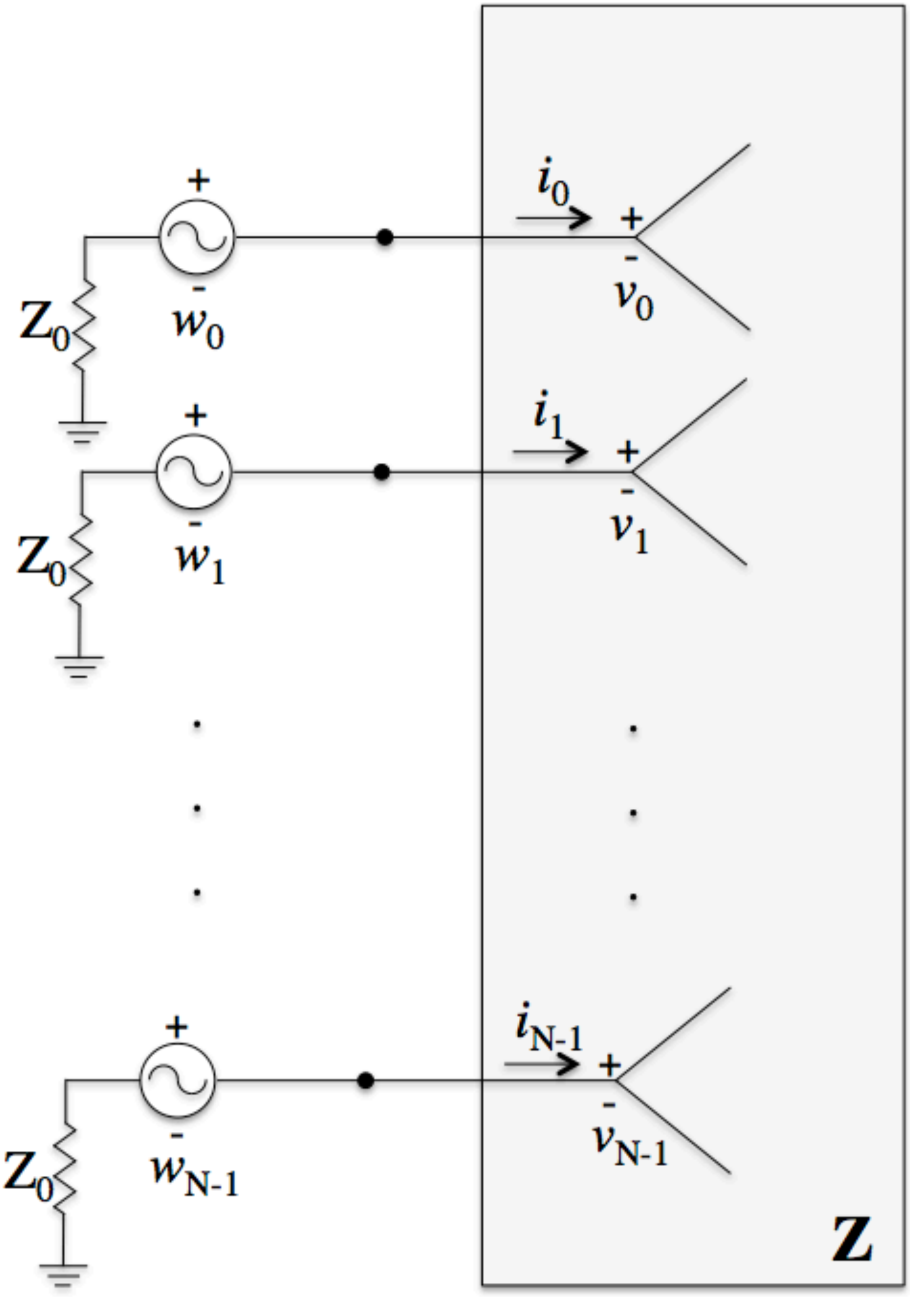

Figure 2-3: Equivalent circuit diagram for the antenna array. The beamformer output is described by a set of voltage sources $\{w_n\}$, each with internal impedance Z_0. The mutual coupling among the array elements is modeled as a N-port network with impedance matrix $\mathbf{Z}$.

Making the substitution $p = n - m$ in (2.3), the beam pattern for the infinite array is

$$\begin{aligned} f^{\mathrm{MC}}(k_z) &= \sum_m \sum_p c_p w_m e^{j(m+p)k_z d} \\ &= \sum_m w_m e^{jmk_z d} \sum_p c_p e^{jpk_z d} \\ &= f(k_z)\, f_c(k_z). \end{aligned} \tag{2.4}$$

In (2.4), we have rewritten the free excitation beam pattern (2.3) as the product of the forced excitation beam patterns due to $\{w_m\}$ and $\{c_p\}$, the latter, which we refer to as the *coupling pattern* of the array $f_c(k_z)$. From (2.4), we can see that the coupling pattern is the beam pattern of the array when a unit excitation is applied to the element located at the origin. Note that this is precisely the embedded pattern shared by all the array elements (up to a phase term). This useful factorization of the beam pattern allows for a convenient separation of the coupling effects from the simpler forced excitation relation used when mutual coupling is ignored.

2.3 Power Efficiency

Under perfect conditions, an array will radiate all the available power delivered by the source. When the power radiated by the array P_{rad} is less than the incident power sent from the source P_{inc}, the array is said to have a loss in the *power efficiency*

$$\eta = \frac{P_{\text{rad}}}{P_{\text{inc}}}. \tag{2.5}$$

If the array is composed of lossless materials, efficiency loss is due to impedance mismatches between the source and the array elements. Since the impedance of each element is the ratio of the voltage to the current across the element terminals, mutual coupling causes these mismatches to vary with each particular array excitation.

For a particular choice of source excitations $\mathbf{w}$, the power radiated by element n is $\mathrm{Re}\{i_n^* v_n\}$. The total power radiated is then

$$\begin{aligned} P_{\text{rad}} &= \sum_{n=0}^{N-1} \mathrm{Re}\{i_n^* v_n\} \\ &= \mathrm{Re}\{\mathbf{i}^\dagger \mathbf{v}\} \\ &= \mathbf{i}^\dagger \,\mathrm{Re}\{\mathbf{Z}\}\mathbf{i} \\ &= \mathbf{w}^\dagger (Z_0\mathbf{I} + \mathbf{Z})^{-1,\dagger}\, \mathrm{Re}\{\mathbf{Z}\}(Z_0\mathbf{I} + \mathbf{Z})^{-1}\mathbf{w}. \end{aligned} \tag{2.6}$$

The power efficiency will be maximized when the array is perfectly impedance matched such that $\mathbf{v} = \mathbf{Z}\mathbf{i} = Z_0\mathbf{i}$. Hence, the total available incident power can be deduced from (2.6) by noting that $P_{\text{inc}} = P_{\text{rad}}$ when $\mathbf{Z} = Z_0\mathbf{I}$, with the result

$$P_{\text{inc}} = \frac{1}{4Z_0}\mathbf{w}^\dagger \mathbf{w}. \tag{2.7}$$

Combining (2.6) and (2.7) with (2.5), we obtain, with some rearranging of terms, the following expression for the array efficiency in terms of the array excitations:

$$\eta = \frac{\mathbf{w}^\dagger(\mathbf{I} - \mathbf{S}^\dagger\mathbf{S})\mathbf{w}}{\mathbf{w}^\dagger\mathbf{w}} = 1 - \frac{\|\mathbf{S}\mathbf{w}\|^2}{\|\mathbf{w}\|^2}, \tag{2.8}$$

where $\mathbf{S} = (Z_0\mathbf{I} - \mathbf{Z})(Z_0\mathbf{I} + \mathbf{Z})^{-1}$ is the standard *scattering matrix* of the array [37].

Chapter 3

Delta-Sigma Quantization for Phased Arrays

In this chapter we consider the issue of pattern distortion caused by *phase quantization* in the excitation of phased arrays. Traditionally, the only recourse available for reducing this distortion has been to decrease the level of quantization error through the use of phase shifters with higher resolution, a primary driver of the high cost of phased arrays. The first of the two array designs proposed in this thesis employs an alternative approach for efficient quantization inspired by the *Delta-Sigma* modulation technique originally developed for use in analog-to-digital converters.

3.1 Traditional Delta-Sigma Quantization Concepts

In practice, the phases of the complex array weights are restricted to some finite set of quantized values defined by the resolution of the phase shifters used in the network connecting the array to the source. Phase shifters with M-bits of resolution can provide any of 2^M values uniformly distributed over the range $[0, 2\pi)$. For a desired excitation $w_n = a_n e^{j\phi_n}$, the realized excitation is $\hat{w}_n = Q[w_n] = a_n e^{j\hat{\phi}_n}$, where the quantization operator Q selects $\hat{w}_n$ such that the phase is the available value closest to ϕ_n. Consequently, this adds undesired distortion to the far-field beam pattern.

The issue of phase quantization in the excitation of array elements draws a close analogy to the difficulty that arises in the implementation of conventional analog-to-digital converters. At each sampling instance, the input signal x_i is mapped to one of a number of discretized values y_i. This introduces an additive error e_i, as shown by the equivalent circuit in Figure 3-1. To keep distortion levels low in the output signal, the circuits in this type of converter require high-accuracy analog components.

3.1.1 Oversampling

Consider a signal bandlimited to $0 \leq f < f_0$ sampled at frequency f_s. When f_s is greater than the Nyquist frequency $2f_0$, the signal is said to be oversampled by a factor defined as the *oversampling ratio* (OSR)

$$\text{OSR} = \frac{f_s}{2f_0}. \tag{3.1}$$

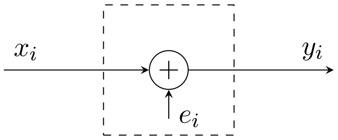

Figure 3-1: Sampled-data equivalent circuit of a conventional analog-to-digital converter.

At the sampling frequency f_s, all of the quantized signal power in y_i is contained within the frequency band $0 \leq f < f_s/2$. If the quantization error e is modeled as white noise, uncorrelated with the signal x, then the spectral density of the sampled noise is evenly distributed over this band, given by

$$E(f) = \sigma_e \sqrt{\frac{2}{f_s}}, \quad 0 \leq f < f_s/2, \tag{3.2}$$

where σ_e^2 is the mean-square value of e.

By oversampling, the signal-to-noise ratio of the output signal y is reduced through the use of a low-pass filter for frequencies above f_0, thereby retaining the entirety of the signal power while limiting the noise power to the portion that falls into the signal band

$$n_0^2 = \int_0^{f_0} E^2(f)df = \sigma_e^2 \left(\frac{2f_0}{f_s}\right) = \frac{\sigma_e^2}{\text{OSR}}. \tag{3.3}$$

This result shows that oversampling reduces the in-band noise in proportion to the oversampling ratio. As such, each doubling of the sampling frequency results in an increase of the signal-to-noise ratio of 3 dB.

3.1.2 Noise shaping

While simple oversampling does reduce in-band noise, a more efficient use of the increased expense of the higher sampling rate can be obtained through the use of *noise shaping.* For this, we will now describe the Delta-Sigma modulator, represented by the equivalent circuit shown in Figure 3-2.

The input signal x_i passes first through an integrator, shown in the equivalent circuit as the delay loop. The output of the integrator w_i then feeds to the quantizer, and the quantized output y_i is fed back and subtracted from the input signal. Whereas the output of the conventional analog-to-digital converter constantly tracks the input signal, this feedback forces the average value of the quantized output to track the average input. As these values differ, the error builds up in the integrator and in time will correct itself.

The input-output relation can be shown as follows. The integrator output is given by

$$\begin{aligned} w_i &= x_{i-1} - y_{i-1} + w_{i-1} \\ &= x_{i-1} - (w_{i-1} + e_{i-1}) + w_{i-1} \\ &= x_{i-1} - e_{i-1}. \end{aligned} \tag{3.4}$$

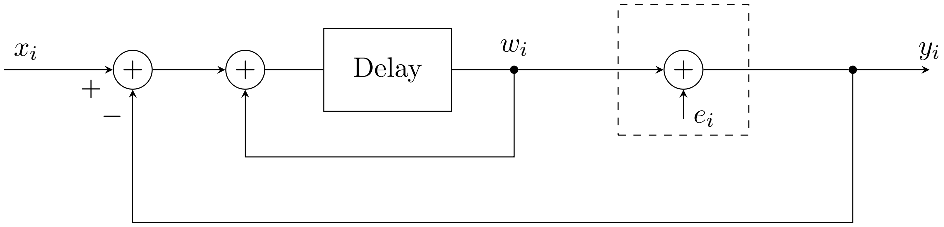

Figure 3-2: Equivalent circuit of the ΔΣ analog-to-digital converter.

This term is then quantized, adding error e_i to give

$$y_i = x_{i-1} + (e_i - e_{i-1})\,. \tag{3.5}$$

The resultant output contains the original (delayed) signal plus an effective error, which is in this case the first-difference of the quantization error:

$$n_i = e_i - e_{i-1}. \tag{3.6}$$

Employing the same white noise model for e as before, we can compare the power spectral densities of the ΔΣ and conventional data converters in order to see the noise shaping effect

$$\begin{aligned} |N(f)|^2 &= |E(f)|^2 \left|1 - e^{-j2\pi f/f_s}\right|^2 \\ &= \left(\frac{2\sigma_e^2}{f_s}\right) 4\sin^2\frac{\pi f}{f_s}. \end{aligned} \tag{3.7}$$

From this expression it can be seen that the noise is suppressed at low frequencies and increased at higher frequencies. This is illustrated in Figure 3-3 for OSR = 8. By applying a low-pass filtering of frequencies above f_0 to the output signal y_i (not depicted in Figure 3-2), only the noise to the left of the dashed line will remain.

The resultant in-band noise power for the ΔΣ quantization is

$$\begin{aligned} n_0^2 &= \int_0^{f_0} |N(f)|^2 df \\ &= \left(\frac{8\sigma_e^2}{f_s}\right) \int_0^{f_0} \sin^2\frac{\pi f}{f_s} df \\ &= \left(\frac{4\sigma_e^2}{f_s}\right) \int_0^{f_0} \left(1 - \cos\frac{2\pi f}{f_s}\right) df \\ &= \frac{4\sigma_e^2}{f_s}\left[f_0 - \frac{f_s}{2\pi}\sin\frac{2\pi f_0}{f_s}\right]. \end{aligned} \tag{3.8}$$

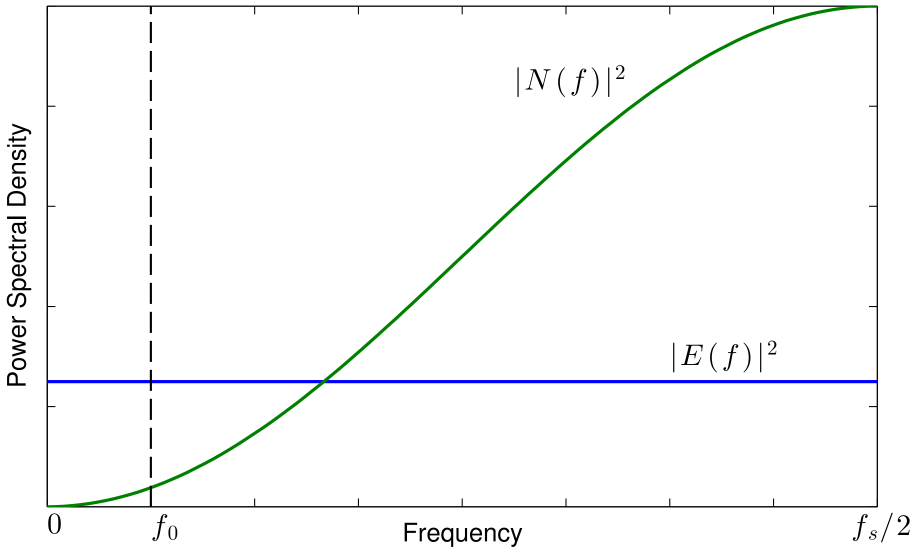

Figure 3-3: Power spectral density of the noise $|N(f)|^2$ from $\Delta\Sigma$ quantization compared with that of conventional quantization $|E(f)|^2$, OSR = 8.

For $f_s \gg f_0$, the small angle formula $\sin x \approx x - x^3/6$ applies, giving

$$\begin{aligned} n_0^2 &\approx \frac{4\sigma_e^2}{f_s}\left[f_0 - f_0 + \frac{1}{6}\frac{f_s}{2\pi}\left(\frac{2\pi f_0}{f_s}\right)^3\right] \\ &= \frac{\sigma_e^2\pi^2}{3}\left(\frac{2\pi f_0}{f_s}\right)^3 \\ &= \frac{\sigma_e^2\pi^2}{3}\,(\mathrm{OSR})^{-3}. \end{aligned} \tag{3.9}$$

So now, with the $\Delta\Sigma$ modulator, each doubling of the sampling frequency results in a gain of 9 dB—an improvement of 6 dB over when oversampling is used alone without the $\Delta\Sigma$ feedback structure.

3.2 $\Delta\Sigma$ Phased Arrays

We now return our attention to the problem of array phase quantization. As mentioned in the beginning of this chapter, for a desired excitation with phase $\phi_n = \angle w_n \in [0, 2\pi)$, the M-bit phase shifters restrict the actual excitations $\hat{w}_n$ to have quantized phase

$$\hat{\phi}_n \in \{0, \Delta\phi_M, 2\Delta\phi_M, \ldots, (2^M - 1)\Delta\phi_M\}, \tag{3.10}$$

where $\Delta\phi_M = 2\pi/2^M$ is the resolution of the phase shifter. Drawing a parallel to the sampling problem discussed in Section 3.1, the problem of array phase quantization is to determine a digital representation of an analog phase input.

While analog-to-digital converters sample a continuous signal in the temporal domain, an array samples a continuous aperture in the spatial domain. For this reason, it is preferable

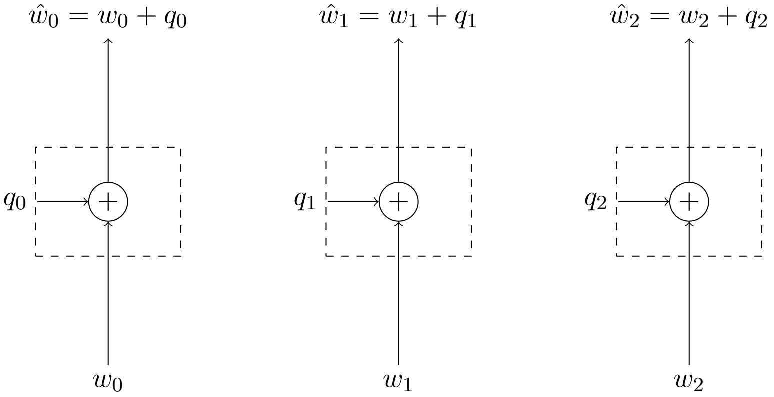

Figure 3-4: Equivalent circuit for conventional phase quantization.

to express the spatial sampling rate in terms of the array *density ratio*

$$R = \frac{1/d}{1/d_0} = \frac{d_0}{d}, \tag{3.11}$$

where $d_0 = \lambda/2$ is the conventional spacing between elements, such that

$$\frac{1}{d_0} = \frac{2}{\lambda} = \frac{k}{\pi} \tag{3.12}$$

is the spatial Nyquist (angular) frequency associated with far-field pattern $f(k_z)$ over the visible region of space $|k_z| < k$, as developed in Chapter 2.

In this section, we develop the ΔΣ phased array first by describing the relationship and mathematical similarities to the ΔΣ modulator. Later, we will explore the nature of this design directly from an array perspective.

3.2.1 Conventional phase quantization

Conventional phase quantization can be illustrated by the equivalent circuit in Figure 3-4. The similarity to the conventional analog-to-digital converter in Figure 3-1 is clear, with the multiple circuit blocks distinguishing the spatial sampling of the array. The M-bit phase shifter is represented by the phase quantization block, which adds quantization error q_n to the desired excitation weight w_n resulting in the phase-quantized output

$$\hat{w}_n = w_n + q_n. \tag{3.13}$$

Instead of the intended beam pattern, the array now has the quantized beam pattern

$$\begin{aligned}\hat{f}(k_z) &= \sum_{n=0}^{N-1} \hat{w}_n e^{jnk_z d} \\ &= \sum_{n=0}^{N-1} w_n e^{jnk_z d} + \sum_{n=0}^{N-1} q_n e^{jnk_z d}. \end{aligned} \tag{3.14}$$

The first term in (3.14) is the desired pattern $f(k_z)$ and the second term is the pattern distortion or *quantization error pattern*

$$f_q(k_z) = \hat{f}(k_z) - f(k_z) = \sum_{n=0}^{N-1} q_n e^{jnk_z d}. \tag{3.15}$$

Signal-to-quantization noise ratio

In Section 3.1, the noise power n_0^2 was used to characterize the effects of oversampling and noise shaping [cf. (3.3) and (3.9)]. For the analysis of the effect of quantization errors on arrays, the related *signal-to-quantization-noise ratio* (SQNR) will be used as a general measure of the relative pattern distortion

$$\mathrm{SQNR} = \frac{P_{\mathrm{signal}}}{P_{\mathrm{noise}}}. \tag{3.16}$$

The signal power P_{signal} refers to the power pattern magnitude in the desired scan direction due to the desired array weights,

$$P_{\mathrm{signal}} = |f(k_{z0})|^2 = \left(\sum_{n=0}^{N-1} |w_n| \right)^2, \tag{3.17}$$

while the noise power P_{noise} is the average noise power distributed throughout the visible region due to the quantization errors in the array weights

$$P_{\mathrm{noise}} = \frac{1}{2k} \int_{-k}^{k} |f_q(k_z)|^2 dk_z. \tag{3.18}$$

Although the value of P_{noise} will be a deterministic function of the specific array weights and the particular quantization levels, a more general interpretation of the noise power considers the expected value over some distribution of weights. In that sense, a white noise model for the quantization errors can be used, as was done for the analog-to-digital converter analysis. It is convenient to normalize the array weights such that the signal power remains fixed at $P_{\mathrm{signal}} = 1$, such that $\mathrm{SQNR} = 1/P_{\mathrm{noise}}$ and the quantization error model may be expressed as

$$E\left[q_m^* q_n\right] = \frac{\sigma_q^2}{N^2} \delta_{mn}, \tag{3.19}$$

where σ_q^2/N^2 is the average noise at the individual elements (fixing P_{signal}), and where

$$\delta_{mn} \triangleq \begin{cases} 1 & m = n \\ 0 & \text{otherwise.} \end{cases} \tag{3.20}$$

Using (3.15) in (3.18) and taking the expected value we obtain the following:

$$\begin{aligned} P_{\text{noise}} &= E\left[\frac{1}{2k}\int_{-k}^{k}\left|\sum_{n=0}^{N-1} q_n e^{jnk_z d}\right|^2 dk_z\right] \\ &= \frac{1}{2k}\int_{-k}^{k}\sum_{n=0}^{N-1}\frac{\sigma_q^2}{N^2}dk_z \\ &= \frac{\sigma_q^2}{N}. \end{aligned} \tag{3.21}$$

The noise power decreases linearly with N, a natural consequence of the averaging effect when the same amount of power is distributed over an increasing number of elements and the quantization terms combine incoherently in the far-field. For a fixed aperture length, $N = N_0 R$, where N_0 is the number of elements with uniform spacing d_0. Thus the SQNR can be written as

$$\text{SQNR} = \frac{N_0 R}{\sigma_q^2}. \tag{3.22}$$

The process of obtaining the result in (3.22) closely follows the analysis of the conventional analog-to-digital converter, with the similar conclusion that a doubling of the density ratio R yields a 3 dB improvement in the SQNR. However, a notable distinction in this case is that rather than necessitating a low-pass filtering of the noise spectrum above the signal band, this filtering occurs naturally as the close element spacing pushes a portion of the quantization noise pattern outside of the visible region while leaving P_{signal} unchanged.

3.2.2 ΔΣ phase quantization

As we saw with the data converters, it is possible to improve the efficacy of spatial oversampling through the use of noise shaping. The ΔΣ array phase quantization technique is analogous to the ΔΣ modulation described in Section 3.1.2. In this case, the purpose is to shape the quantization noise pattern to higher values of $|k_z|$ by implementing the phase quantization as shown by the equivalent circuit in Figure 3-5.

In this implementation, the feedback loop is represented by the difference between the input to the quantizer and its output. This difference is added to the quantizer input at the next element, achieving the effect of the integrator in the ΔΣ modulator. As before, the average value of the quantized output tracks the average input, and any persistent difference between these values accumulates in the feed forward path and eventually corrects itself. The input-output relation between the desired weight and the ΔΣ quantized weight is

$$\hat{w}_n = Q[w_n - q_{n-1}] = w_n - (q_n - q_{n-1}). \tag{3.23}$$

This result is mathematically equivalent to (3.5), the only exception being the one-step delay in the ΔΣ modulator implementation.

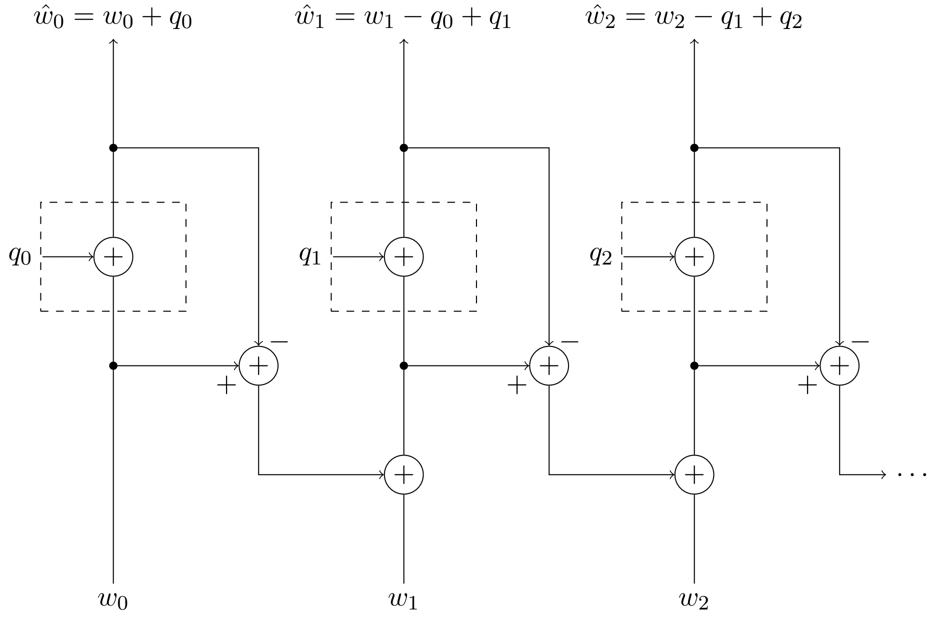

Figure 3-5: Equivalent circuit for $\Delta\Sigma$ phase quantization.

With the $\Delta\Sigma$ excitations, the quantization error pattern is given by

$$\begin{aligned} f_q(k_z) &= \sum_{n=0}^{N-1} (q_n - q_{n-1}) e^{jnk_z d} \\ &= \sum_{n=0}^{N-1} q_n e^{jnk_z d} - \sum_{n'=-1}^{N-2} q_{n'} e^{j(n'+1)k_z d} \\ &= (1 - e^{jk_z d}) \sum_{n=0}^{N-2} q_n e^{jnk_z d} + q_{N-1} e^{j(N-1)k_z d}. \end{aligned} \tag{3.24}$$

Here we see our first divergence from the $\Delta\Sigma$ modulator development: the finite aperture length of the array makes it such that only the first $N-1$ elements make appropriate use of the $\Delta\Sigma$ excitations, as the final element has no following element to which the error term is fed.

SQNR in $\Delta\Sigma$ arrays

The SQNR for the $\Delta\Sigma$ array can be analyzed using the framework developed in Section 3.2.2 by replacing the quantization error pattern in (3.21) with (3.24). To begin, we can ignore the finite aperture effect and assume that the summation in (3.24) is taken over all

N elements in order to keep the relation to the analog-to-digital converters clear.

$$\begin{aligned}P_{\text{noise}} &= E\left[\frac{1}{2k}\int_{-k}^{k}\left|1-e^{jk_zd}\right|^2\left|\sum_{n=0}^{N-1} q_n e^{jnk_zd}\right|^2 dk_z\right] \\ &= \frac{1}{2k}\int_{-k}^{k}\left(4\sin^2\frac{k_zd}{2}\right)\sum_{n=0}^{N-1}\frac{\sigma_q^2}{N^2}dk_z \\ &= \frac{2\sigma_q^2}{N}\frac{1}{2k}\int_{-k}^{k}(1-\cos k_zd)\,dk_z \\ &= \frac{2\sigma_q^2}{N}\left[1-\frac{1}{kd}\sin kd\right]. \qquad (3.25)\end{aligned}$$

For $d \ll \pi/k$, we use the small angle approximation for the sine term to obtain

$$P_{\text{noise}} \approx \frac{2\sigma_q^2}{N}\left[1-\frac{1}{kd}\left(kd-\frac{1}{6}(kd)^3\right)\right] = \frac{\sigma_q^2}{N}\frac{k^2d^2}{3}. \qquad (3.26)$$

The first term in this result σ_q^2/N is the noise power for the conventional phase quantization. The second term is proportional to R^{-2} since $d = d_0/R$, and we see that as with the $\Delta\Sigma$ modulator, the noise shaping reduces the noise by an extra 6 dB with each doubling of the array density, in addition to the 3 dB improvement due to the averaging effect.

We can include the finite array effect directly by scaling the above result by a factor of $(N-1)/N$ to account for the fraction of the total power that goes to the final element, which adds an additional σ_q^2/N^2 to the final expression

$$P_{\text{noise}} = \frac{N-1}{N}\frac{\sigma_q^2\pi^2}{3N_0}R^{-3} + \frac{\sigma_q^2}{N_0^2}R^{-2}, \qquad (3.27)$$

where $k = \pi/d_0$ was substituted to highlight the similarity to (3.9). In principle, as R grows very large, the effect of the $\Delta\Sigma$ cancellations will continue to eliminate the noise due to the rest of the array to the point that the noise caused by this single element becomes the dominant source of quantization noise. However, in nearly all practical settings this edge contribution will be negligible. As an example, for an array of length $L = 2\lambda$ ($N_0 = 4$), a density ratio of $R = 12.9$ is required for the two terms in (3.27) to be comparable in magnitude.

3.3 Delta-Sigma Implementation

When designating the complex array weights, a beam-steering computer (BSC) computes the desired weights and sends a control signal to the phase shifters indicating which of the 2^M quantized phase shifts to apply to the incoming or outgoing signal. This may be performed in an analog sense, where the the steering signal takes any value—not necessarily confined to the same discrete set as the phase shifter—and the phase shifter applies the closest possible shift. Alternatively, the computer can communicate directly to the phase shifter using an M-bit message corresponding to which of the quantized shifts is to be applied.

The $\Delta\Sigma$ array uses 2-bit phase shifters and a uniform amplitude $\hat{a}$ for the weight of each array element, and as such these weights take one of only *four* possible values:

$$\hat{w}_n = Q[w_n - q_{n-1}] \in \{\frac{\hat{a}}{\sqrt{2}}(1+j), \frac{\hat{a}}{\sqrt{2}}(1-j), \frac{\hat{a}}{\sqrt{2}}(-1-j), \frac{\hat{a}}{\sqrt{2}}(-1-j)\}. \tag{3.28}$$

One benefit of this architecture is that it allows the bulk of the operational complexity to be performed digitally. The BSC determines the $\Delta\Sigma$ weights according to the following simple algorithm.

```
function weights_ds = quantize_delta_sigma(weights,amplitude)

weights_ds = zeros(size(weights));
q_ds = zeros(size(weights));

weights_ds(1,:) = amplitude*quantize2bits(weights(1,:));
q_ds(1,:) = weights_ds(1,:)-weights(1,:);

for nn = 2:length(weights(1,:))
    weights_ds(nn,:) = amplitude*quantize2bits(weights(nn,:)-q_ds(nn-1,:));
    q_ds(nn,:) = weights_ds(nn,:)-weights(nn,:)+q_ds(nn-1,:);
end

%%
function output = quantize2bits(input)

output = (sign(real(input)) + 1j*sign(imag(input)))/sqrt(2);
```

Last, we need to determine how to set $\hat{a}$ relative to the magnitude of the desired weights $a_n = |w_n|$. This same issue arises in determining the quantization levels in the $\Delta\Sigma$ ADC. There is no known "best" solution in terms of optimizing the output SQNR for a given input, yet there is an answer to the problem of ensuring *stability*. For the case of 1-bit $\Delta\Sigma$ quantization of a real-valued bounded input signal $|x[n]| < a$ for all n, output stability is guaranteed for quantized output levels $y[n] = \pm b$ when $b \geq 2a$ [11].

In the case of the $\Delta\Sigma$ array, we have the additional consideration of the array efficiency, as described in Section 2.3. From (2.7), the power sent to each element is proportional to $|w_n|^2$. Considering the case $a_n = a$ for all n, if we choose to follow the stability guarantee—for both real and imaginary components—we have $\hat{a} = 2\sqrt{2}a$, and as a result it would take 8 times the power to obtain approximately the same pattern. Fortunately, the stability guarantee requirement is overly strict in nearly all cases. Further, the digital implementation of the $\Delta\Sigma$ weights allows the BSC to determine an appropriate value of $\hat{a}$ and can adjust when necessary to avoid any unbounded situations.

The value of $\hat{a}$ plays a role beyond ensuring stability. It also affects how closely the quantization errors hold to the white noise model given by (3.19). This can be illustrated with an example to show how the SQNR dependence on the density ratio also depends on $\hat{a}$. Using numerical simulations, exact values of P_{noise} were determined over a range of density ratios for the case of a length $L = 20\lambda$ linear array of ideal isotropic elements, designed to scan uniformly throughout real space with uniform amplitude weighting for all elements. At each value of R the desired array weights were normalized to fix the peak signal at $P_{\text{signal}} = 1$,

$$a_n = \frac{1}{N} = \frac{1}{40R}. \tag{3.29}$$

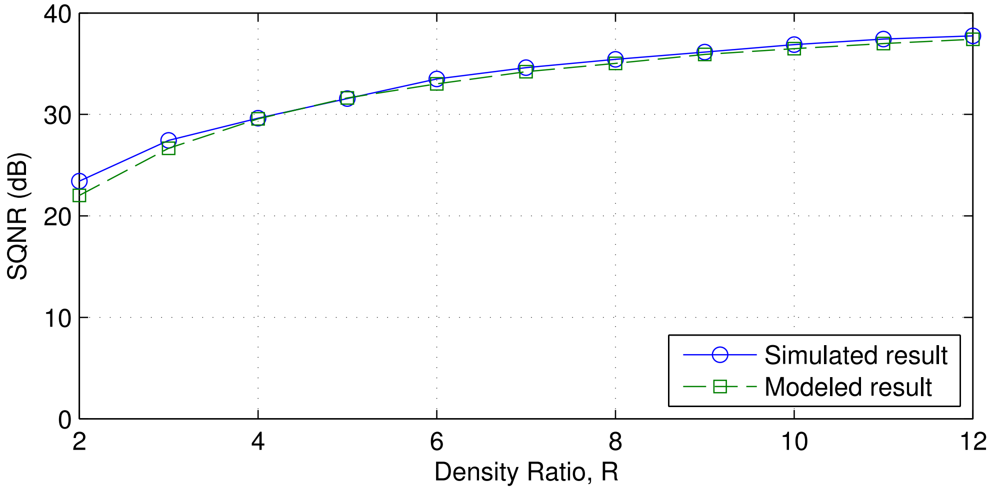

Figure 3-6: $\Delta\Sigma$ SQNR results for uniform amplitude scanning array of length $L = 20\lambda$.

For the case of uniform amplitude weighting, we can express the relative amplitude of the $\Delta\Sigma$ weights as

$$\gamma = \frac{\hat{a}}{a}, \tag{3.30}$$

so that the incident power to the array is simply γ^2 times greater for the $\Delta\Sigma$ weights than for the desired weights. For this example, we use $\gamma = 1.26$. The noise power was calculated directly from (3.18) by averaging the noise power over the visible region at a given scan angle, then evaluating the mean value over 500 scan angles. In addition, the predicted value of P_{noise} from (3.27) was calculated from the resultant sample values of σ_q^2 for each R. With the array weights properly normalized, these results were inverted, yielding the simulated and predicted SQNR at each R, as depicted in Figure 3-6, which shows close agreement between the two curves. However, if we compare the SQNR at $R = 2$ to $R = 4$, we see an improvement of 6 dB, 3 dB less than our analysis predicted would be associated with a doubling of the array density. From $R = 4$ to $R = 8$, we see even less of an increase, indicating the likely culprit is not the small angle approximation used to obtain the R^{-3} dependence. The actual cause is due to the sample value of σ_q^2 evaluated within the simulations, which happens to be increasing with R—in disagreement with the assumption that w_n and q_n are independent. We will return to this discussion in Chapter 4.

3.4 Phase Errors

In addition to the effects of quantization, a number of other factors can cause pattern distortions. These include errors in the amplitudes and phases of the array weights, positioning and orientation errors, element pattern variations, and inoperative or missing elements. To a certain degree, it is possible to compensate for systematic errors through careful calibration. Even so, the presence of some level of random errors is unavoidable. Such errors can lead to decreased directivity, increased sidelobe levels, and shifts in the main beam location from the desired scan angle [39].

A statistical analysis of these errors and their effects may be found in most standard texts concerning arrays (e.g., [23, 40, 41]). In this section we limit our attention to random phase errors in order to facilitate a practical comparison of the quantization noise in $\Delta\Sigma$ and conventionally quantized phased arrays.

The issue of phase errors becomes increasingly important at higher frequencies as the effect of mild changes in the signal path lengths can result in significant changes in the phase. As phase errors increase, the utility of high-resolution phase shifters lessens. For some perspective, consider the 5-bit phase shifter with phase resolution of $2\pi/2^5$ radians ($11.25°$). At a frequency of $f = 100$ GHz, a change in the feed path of slightly less than 0.1 mm yields a phase error equal to the resolution of this phase shifter.

The difficulties beyond the issue of phase quantization in ensuring accurate phase control at high frequencies have important implications to the $\Delta\Sigma$ array design. Namely, the $\Delta\Sigma$ array is more suited to deal with such errors for two reasons. First, the performance of the array is inherently less dependent on accurate phase control; and second, the pattern distortion due to these phase errors naturally decreases for dense arrays as a result of the averaging effect.

By adding random gaussian phase errors to the SQNR simulations performed in the previous section, a comparison can be made between the conventional and $\Delta\Sigma$ arrays, yielding the results shown in Figure 3-7.

3.5 Array Theory Perspective

Our development thus far has built upon the mathematical similarities between the notions of sampling in the temporal and spatial domains. Alternatively, it is illustrative to examine this design directly from the principles of antenna array theory. To understand the mechanism by which the $\Delta\Sigma$ array reduces pattern distortion, we consider a simple two-element array with opposing excitation weights $w_0 = 1$ and $w_1 = -1$. From (2.1), the beam pattern is

$$f(k_z) = 1 - e^{jk_z d}, \tag{3.31}$$

and the associated power pattern

$$P(k_z) = 4\sin^2(k_z d/2) \tag{3.32}$$

vanishes at $k_z = 0$, increasing monotonically to peak values at $k_z = \pm\pi/d$. For standard spacing $d = d_0 = \lambda/2$, this places the peaks at the edges of the visible region $\mathcal{V}$. The power pattern of (3.32) is shown for $d = d_0$, $d_0/2$, and $d_0/4$ in Figure 3-8. As the spacing is decreased, the peaks are steered outside of $\mathcal{V}$, while at the same time flattening the pattern inside. In the limit as $d \to 0$, the array becomes increasingly similar to a single antenna with a weighting of zero and $P(k_z)$ becomes vanishingly small. In the $\Delta\Sigma$ array, the original array weights in (3.23) behave as intended, but the quantization *errors* combined with the purposely subtracted terms at the neighboring elements behave like this two-element array, and their contributions to the array pattern throughout real space diminishes as the spacing between elements is decreased.

The relation of the $\Delta\Sigma$ array to the two-element array patterns can be seen in the example patterns shown in Figure 3-9. In each plot, the desired and $\Delta\Sigma$ quantized patterns are shown for scan direction $k_{z0} = k/22$. Comparing the two patterns for the case of $R = 1$, we can see that the distortion falls under an envelope that increases away from the origin throughout the visible region in a manner consistent with the behavior of the $\lambda/2$ spaced

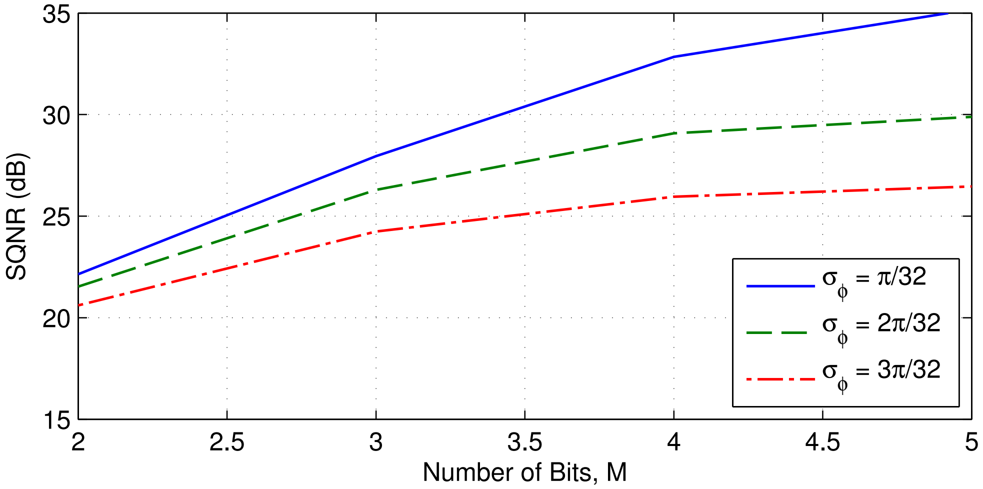

(a) Conventional M-bit quantization

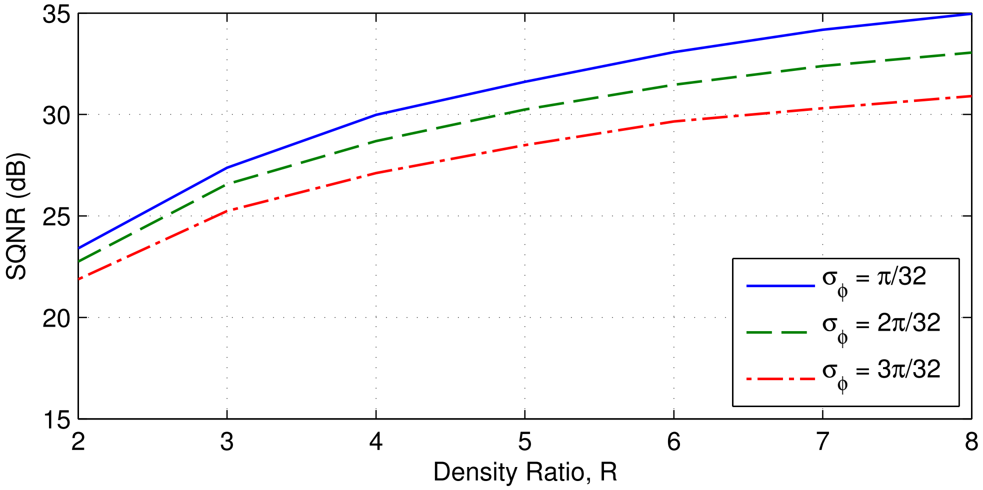

(b) $\Delta\Sigma$ 2-bit quantization

Figure 3-7: Comparison of effects of random phase errors with standard deviation σ_ϕ radians on SQNR for (a) conventional quantization and (b) $\Delta\Sigma$ quantization.

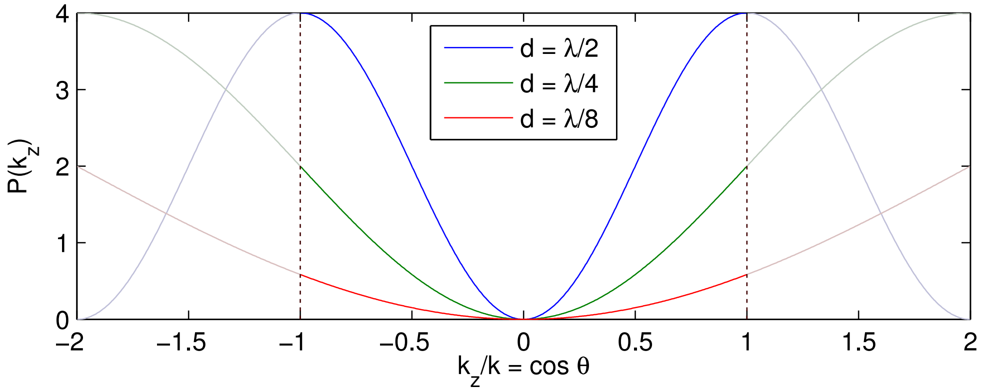

Figure 3-8: Power pattern for a two-element array with excitation weights $w_0 = 1$ and $w_1 = -1$. The edges of the visible region are marked with vertical dotted lines.

pattern of Figure 3-8. Similarly, the behavior of the $\Delta\Sigma$ array continues to accord with the general behavior of the two-element array as the spacing is decreased.

Comparing (3.31) with the first additive term in (3.24), we can interpret the quantization error pattern as the array pattern corresponding to array weights given by $\{q_n\}$—with the isotropic elements replaced by elements having patterns given by (3.31). As such, the $\Delta\Sigma$ error passing scheme shown in Figure 3-10 can be visualized in terms of the pattern associated with the $\Delta\Sigma$ *kernel*, composed of the two opposite excitations seen in Figure 3-11. This perspective will be useful in the following section.

3.6 Delta-Sigma Planar Arrays

Extensions of the $\Delta\Sigma$ quantization technique to planar arrays may be grouped roughly into two categories of design approaches. The simpler approach is to design the two-dimensional array such that elements are spaced closely along a single dimension in order to exploit the $\Delta\Sigma$ cancellation of the quantization errors, thus allowing for standard element spacing along the other dimension. A more interesting approach can be applied to arrays of elements that may be closely spaced along both dimensions. As an example, consider an electrically small patch antenna with an impedance match to account for the non-resonant element size. In contrast to the 1-D $\Delta\Sigma$ scheme, where the quantization error imposed at each element is subtracted in whole at the input of the neighboring element, a 2-D scheme may be employed that subtracts a fraction of the quantization error along each dimension. In this case, the 2-D counterpart to Figure 3-10 is illustrated in Figure 3-12, which shows the quantization error for each element being passed to the right by a factor α and being passed upward by a factor β, where $\alpha + \beta = 1$, and the $\Delta\Sigma$ quantized excitation is given by

$$\hat{w}_{m,n} = Q\left[w_{m,n} - \alpha q_{m-1,n} - \beta q_{m,n-1}\right] = w_{m,n} - \alpha q_{m-1,n} - \beta q_{m,n-1} + q_{m,n}. \tag{3.33}$$

For a planar rectangular array with excitation weight w_{mn} applied to the element at

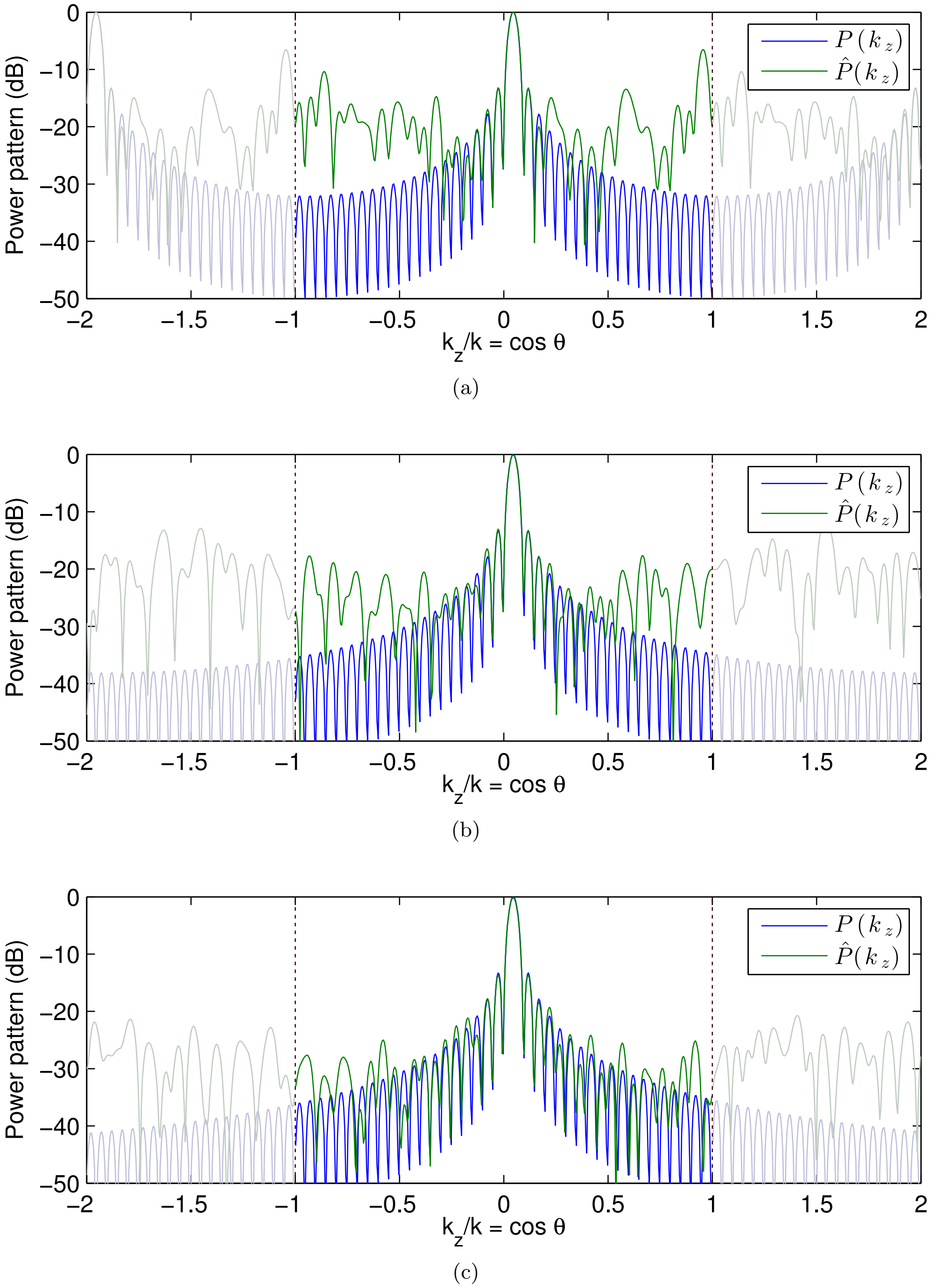

(a)

(b)

(c)

Figure 3-9: Power patterns $P(k_z)$ (ideal weights) and $\hat{P}(k_z)$ ($\Delta\Sigma$ weights) for arrays of length $L = 20\lambda$ scanned to $k_{z0} = 0.045k$ for density factors (a) $R = 1$ (b) $R = 2$ and (c) $R = 4$.

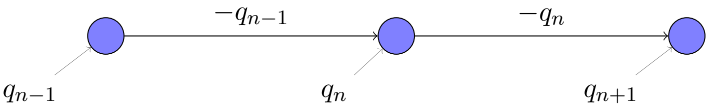

Figure 3-10: 1-D error passing.

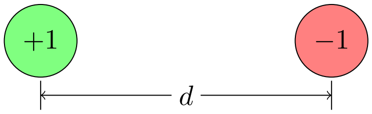

Figure 3-11: 1-D error kernel.

location $x = md$ and $y = nd$, the pattern is

$$f(k_x, k_y) = \sum_{n=0}^{N-1} \sum_{m=0}^{M-1} w_{mn} e^{j(mk_x + nk_y)d}, \tag{3.34}$$

where $k_x = k \sin\theta \cos\phi$ and $k_y = k \sin\theta \sin\phi$ denote the direction over the half-sphere given by $k_x^2 + k_y^2 \leq k^2$. Using the error terms from (3.33), the quantization error pattern associated with Figure 3-12 is

$$f_q(k_x, k_y) = \sum_{n,m} (q_{m,n} - \alpha q_{m-1,n} - \beta q_{m,n-1}) e^{j(mk_x + nk_y)d}. \tag{3.35}$$

Ignoring edge effects in this analysis, the above can be manipulated to obtain the following form

$$f_q(k_x, k_y) = \left(1 - \alpha e^{jk_x d} - \beta e^{jk_y d}\right) \sum_{n,m} q_{m,n} e^{j(mk_x + nk_y)d}. \tag{3.36}$$

As with the linear array, this expression can be used to find the expected value of P_{noise} by integrating $E\left[|f_q(k_x, k_y)|^2\right]$ over the half-sphere. Like before, the result will be determined by the terms preceding the summation, which represents the equivalent kernel pattern associated with the $\Delta\Sigma$ scheme in Figure 3-12. By symmetry, the resultant noise power will be minimized for $\alpha = \beta = 1/2$, in which case the $\Delta\Sigma$ kernel is as shown in Figure 3-13, with the kernel power pattern shown for a density ratio of $R = 4$ ($d = \lambda/8$) as seen in Figure 3-14. Compared to the linear array kernel pattern given by the $d = \lambda/8$ curve in Figure 3-8, which has peak value in visible space of $P(k_z = k) = 0.59$, the peak value for this 2-D result is reduced by a factor of approximately 1/2. This result is intuitive, as this passing scheme separates the error into orthogonal element pairs, which can be seen by considering the “+1” element of the 2-D kernel as the superposition of two “+1/2” excitations, each

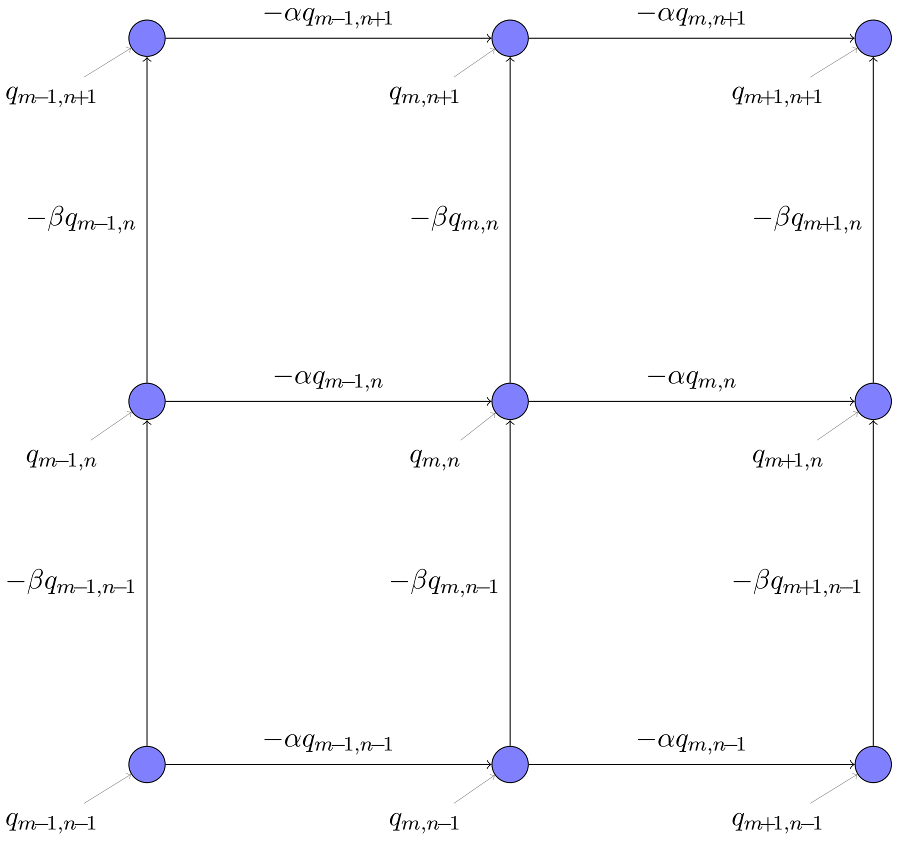

Figure 3-12: 2-D error passing.

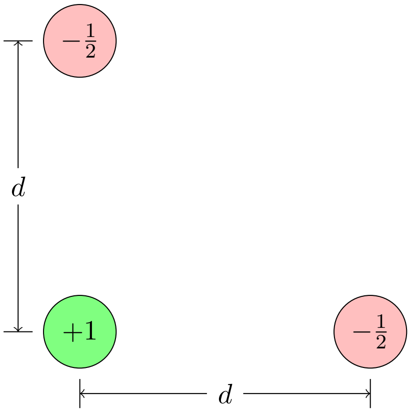

Figure 3-13: 2-D error kernel associated with Figure 3-12.

with opposing terms along distinct axes.

In Figure 3-14, the noise shaping is notably more effective on the symmetry axis given by $k_x = k_y$ than for $k_x = -k_y$. This behavior is to be expected from the underlying kernel geometry, and suggests the possibility of other, perhaps more optimal $\Delta\Sigma$ error passing techniques. One such alternative is shown in Figure 3-15. In this passing scheme, the error is subtracted equally to both the upward and right side neighbor, and then added to the the element diagonally across in order to compensate for the extra subtracted term, resulting in a symmetric $\Delta\Sigma$ kernel. The kernel power pattern in this case is shown in Figure 3-16 for $R = 4$.

The relative noise power (normalized by σ_q^2 and the total number of elements MN) for both 2-D $\Delta\Sigma$ kernels is shown in Figure 3-17. At very small density ratios, the advantage of separating the quantization error into orthogonal terms results in better noise power performance for the first $\Delta\Sigma$ kernel type, evidenced by the 3 dB difference between the curves at $R = 1$. However, the symmetrical second type quickly outperforms the first, with the noise power decreasing with R^4 as opposed to R^2 in the first case.

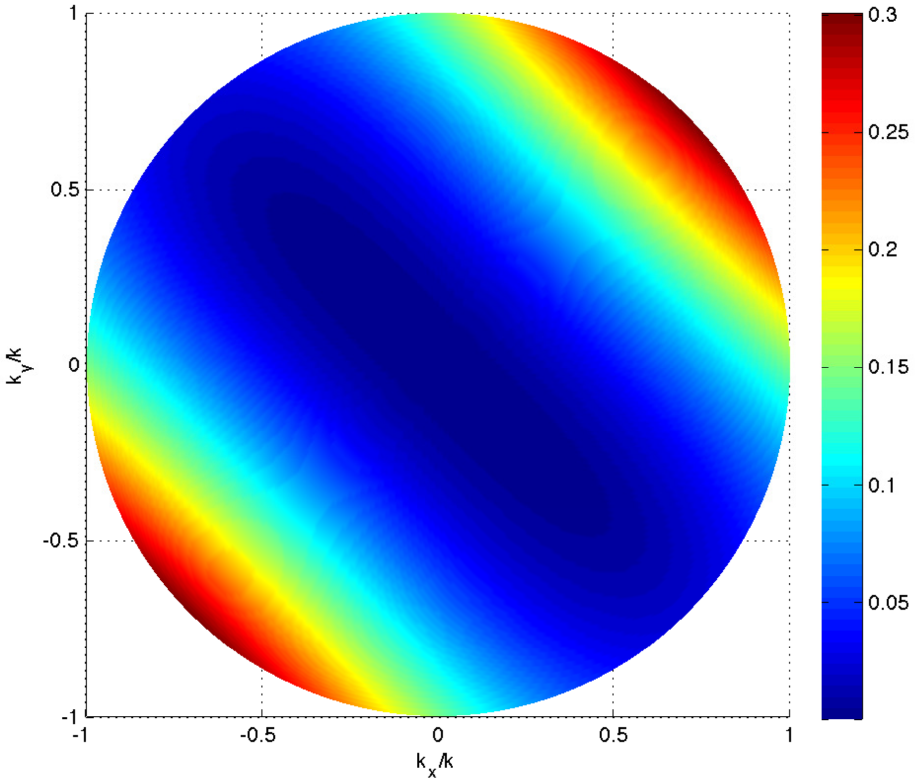

Figure 3-14: 2-D $\Delta\Sigma$ kernel pattern for $R = 4$.

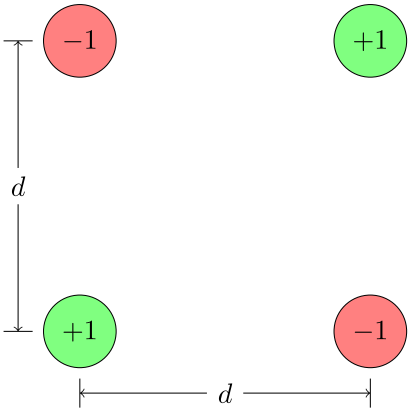

Figure 3-15: Alternative symmetric 2-D error kernel.

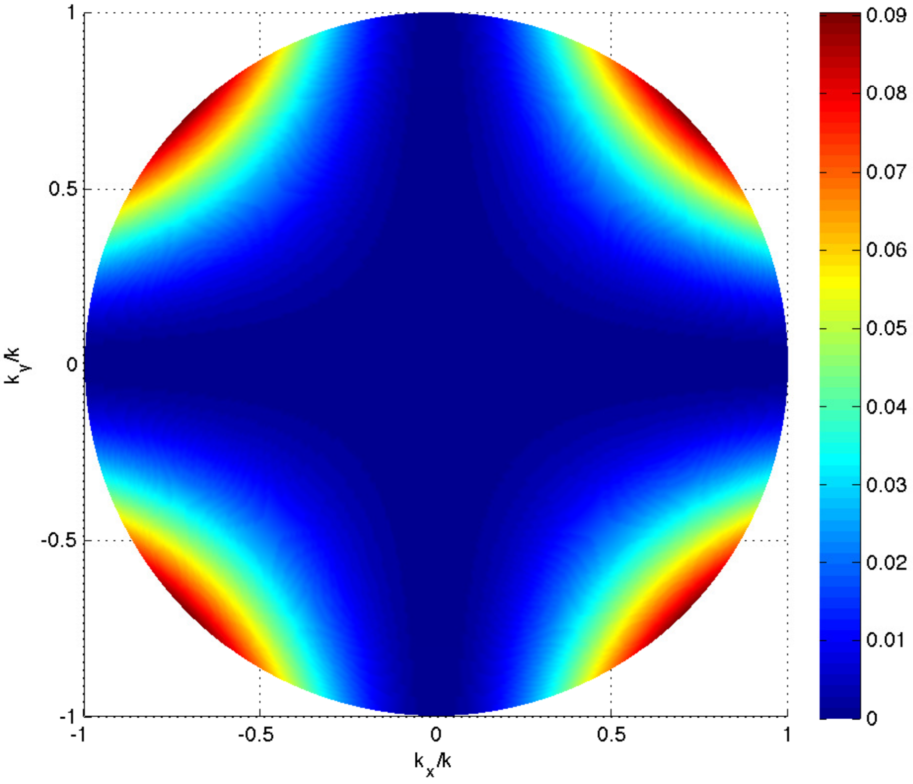

Figure 3-16: Alternative 2-D $\Delta\Sigma$ kernel pattern for $R = 4$.

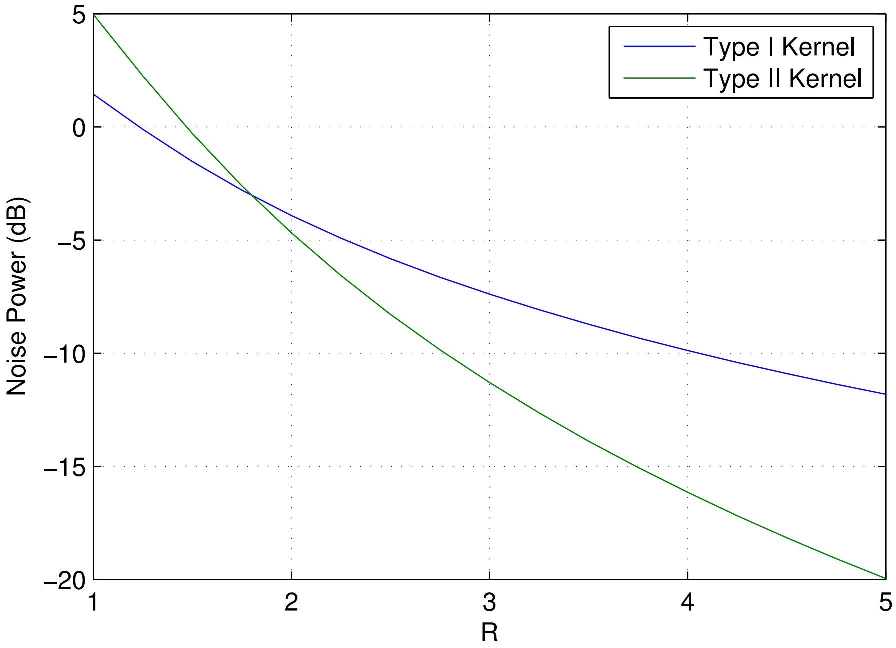

Figure 3-17: Relative noise power for both 2-D $\Delta\Sigma$ kernels.

Chapter 4

Mutual Coupling Effects

In the design of a dense array, the close proximity of the elements makes it particularly important to understand and account for the effects of mutual coupling. The results presented in Chapter 3 were determined based on the forced excitation model. We now will consider the more realistic free excitation model and determine whether the $\Delta\Sigma$ array continues to perform as desired. Our treatment in this chapter first examines the effect of mutual coupling on the $\Delta\Sigma$ array pattern. Following the analysis approach described in Chapter 2, we will initially consider the infinite array case and treat the edge effects due to finite array lengths separately. In the latter portion of this chapter, we turn our attention to the $\Delta\Sigma$ array efficiency performance and the ability to design an effective impedance matching network. To this end, we use the narrowband perspective to provide a detailed description of the mechanisms that affect the $\Delta\Sigma$ array efficiency and then continue with a demonstration of the wideband performance benefits over conventional array designs.

4.1 Mutual Coupling in Dense Arrays

Recall from (2.4) that under the free excitation model, the beam pattern of the infinite array can be decoupled into the product of the corresponding forced excitation pattern $f(k_z)$ and the coupling pattern $f_c(k_z)$, which is an inherent property of the array, independent of the particular excitations. Consequently, the $\Delta\Sigma$ beam pattern in any direction $\hat{f}^{\mathrm{MC}}(k_z)$ may be thought of as the $\Delta\Sigma$ beam pattern analyzed in Section 3.2.2 multiplied by a proportionality constant given by the coupling pattern. From this viewpoint, the interactions among the array elements—regardless of spacing—should have a problematic effect only if $f_c(k_z)$ generally tends to be of greater magnitude in the regions of real space for which the $\Delta\Sigma$ pattern distortions are the most extreme, that is, towards larger values of $|k_z|$. Further, the likelihood of this being the case may be addressed intuitively by considering the forced excitation idealization as a special case of the free excitation model with coupling coefficients $c_p = \delta_{p,0}$, corresponding to $f_c(k_z) = 1$. More generally, we expect c_p to decay smoothly with $|p|$. Based on a standard result from Fourier analysis [42], this more gradual decay of the coupling coefficients implies that $f_c(k_z)$ should decrease away from the origin, unlike the “flat” coupling pattern associated with forced excitation model. This observation suggests that mutual coupling has the effect of actually *suppressing* the most troublesome pattern distortions located near the extents of the visible region.

To simulate the effects of mutual coupling, the model given by Wasylkiwskyj et al. [43] for the mutual impedance of two thin-wire dipole antennas was used. In this model, the system impedance is normalized such that $Z_0 = 1$ and the impedance matrix entries are given by

$$Z_{mn} = \begin{cases} 1 & m = n \\ H_0^{(2)}(kd|n-m|) & m \neq n, \end{cases} \tag{4.1}$$

where $H_0^{(2)}(\cdot)$ is the zeroth-order Hankel function of the second kind. While the analysis in [43] is specific to the case of two isolated thin-wire dipoles, the results apply rather directly to our array setup. Indeed, the presence in the array environment of the additional open-circuited dipoles in the determination of the impedance matrix elements has negligible effect as the two separated dipole halves are far from resonant and appear relatively transparent to the electromagnetic fields.

Using (4.1), the coupling matrix $\mathbf{C}$ was determined for the array of length $L = 20\lambda$ with density ratio $R = 4$. For an array of this size, the entries of the coupling matrix corresponding to an element near the center of the array are nearly identical to the non-trivial coupling coefficients $\{c_p\}$ of an infinite array element. The magnitudes of these values $|c_p|$ are shown in Figure 4-1a versus the element separation index p. The associated coupling pattern $f_c(k_z)$ is shown in Figure 4-1b, in which we see the expected decrease away from the origin, with particularly sharp drop-offs beyond $|k_z/k| = 0.9$.

To illustrate the overall effect of mutual coupling, the pattern calculations performed to create Figure 3-9 were repeated based on the free excitation model using (2.3) with coupling matrix entries determined by (4.1). The quantization error patterns for both the forced and free excitation models, $f_q(k_z)$ and $f_q^{\mathrm{MC}}(k_z)$, are shown in Figure 4-2 for $R = 1$, 2, and 4. In each of the three cases, the distortion near the edges of the visible region, where $\Delta\Sigma$ noise shaping alone is least effective, is decreased when the calculation accounts for mutual coupling, as implied by Figure 4-1b.

While the infinite array analysis explains the effect of mutual coupling near the edges of visible space, the slight increase in the pattern distortion near the origin seen in the case of $R = 4$, for example, is not accounted for by this approach, as the infinite array analysis predicts no modification along this direction. From this observation, we may surmise that edge effects have slightly greater significance due to mutual coupling. This result is unsurprising since in the case of the finite array, the embedded element patterns in actuality exhibit more variations for the elements near the array edges. As a result, the opposing $\Delta\Sigma$ quantization errors do not cancel quite as effectively as elements with identical embedded patterns. However, these effects appear to be relatively benign, appearing only when the pattern distortion is decreased to about 30 dB below the main lobe level.

When the SQNR calculations used to generate Figure 3-6 are repeated for the free excitation model, the results are as shown in Figure 4-3. The simulated results for the forced excitation model are also shown to illustrate that the effects of coupling add only a small amount of additional error, consistent with the above discussion.

4.2 Narrowband Efficiency

The power efficiency of the $\Delta\Sigma$ array is affected by both the increased array density and the unique nature of the $\Delta\Sigma$ excitations. We begin with a description of a simple yet effective approach for maintaining acceptable array efficiencies for general dense scanning arrays, and then apply this concept specifically to the $\Delta\Sigma$ array.

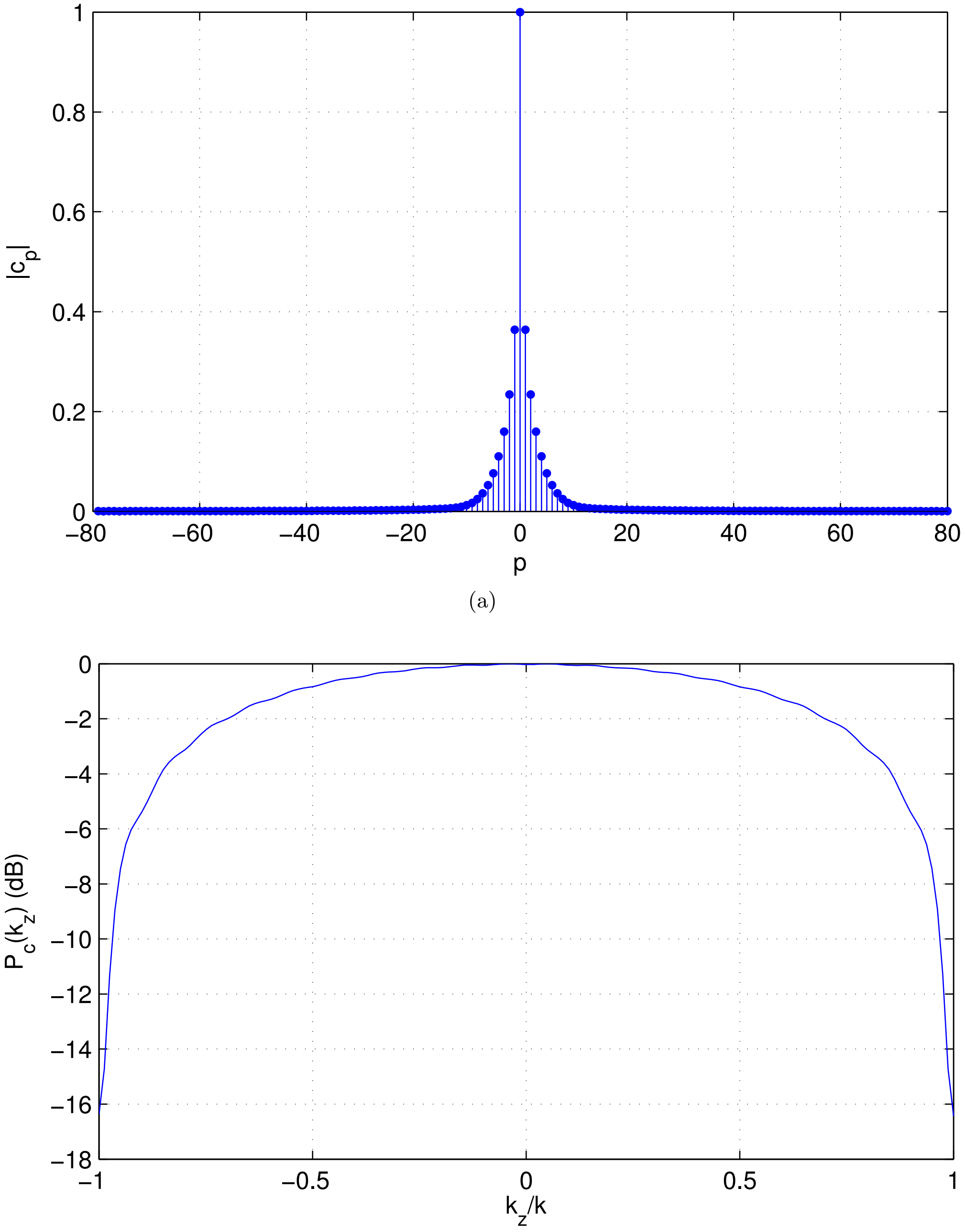

(a)

(b)

Figure 4-1: (a) Magnitude of the coupling coefficients $\{c_p\}$ for a central element in an array of length $L = 20\lambda$, with $R = 4$. (b) Power pattern response $P_c(k_z) = |f_c(k_z)|^2$ for an array excited by the coupling coefficients.

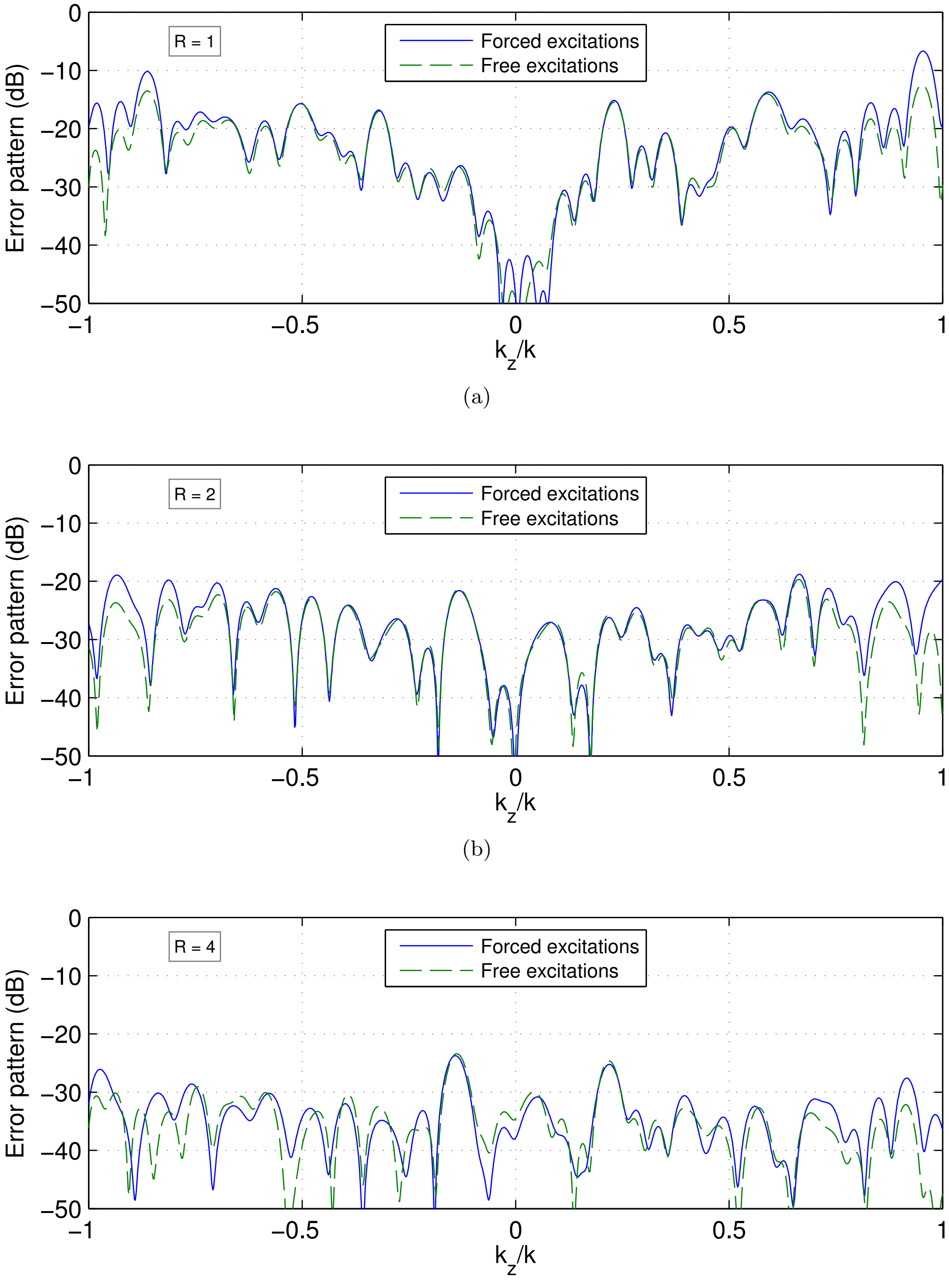

(a)

(b)

(c)

Figure 4-2: Quantization error (power) patterns for the $\Delta\Sigma$ array of length $L = 20\lambda$ using both the forced and free excitation models with density ratios (a) $R = 1$ (b) $R = 2$ and (c) $R = 4$.

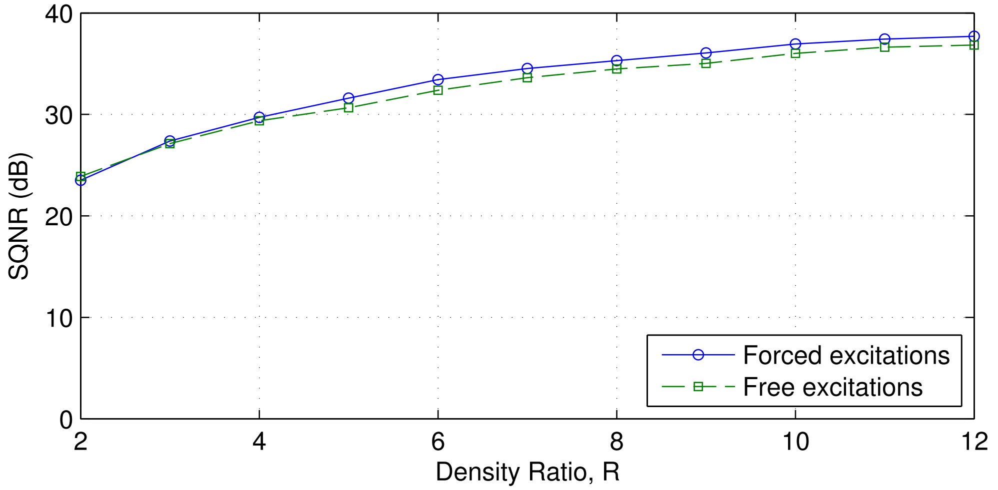

Figure 4-3: Comparison of SQNR versus density ratio R for $\Delta\Sigma$ arrays based on the forced and free excitation models. $L = 20\lambda$.

Impedance Matching for Dense Arrays

Impedance mismatch losses can be reduced by placing a matching network between the source and the array. For a single antenna, a perfect match may be obtained by using a series reactance and a quarter-wavelength of transmission line to match the imaginary and real parts of the antenna impedance, respectively, to the source impedance. With a phased array, the presence of mutual coupling makes matching much more complicated, necessitating the use of complex matching networks to avoid efficiency losses. Examples include the use of dynamically varying components that modify the network characteristics for every set of array excitations or a web of interconnections between the array elements.

A far more practical alternative is based on the notion of *scan impedance*, defined as the effective impedance (sometimes referred to as the active impedance) of each element when scanned to a particular direction k_{z0} [41]

$$Z_n^{\text{scan}}(k_{z0}) = \frac{v_n(k_{z0})}{i_n(k_{z0})}. \tag{4.2}$$

For the particular set of excitations corresponding to scan angle k_{z0}, it follows that $\mathbf{v}(k_{z0}) = \mathbf{Z}\,\mathbf{i}(k_{z0}) = \mathbf{Z}^{\text{scan}}(k_{z0})\mathbf{i}(k_{z0})$, where $\mathbf{Z}^{\text{scan}}(k_{z0})$ is a diagonal matrix with entries given by (4.2). Because of this, the scattering matrix at this scan angle can also be replaced by substituting $\mathbf{Z}$ with $\mathbf{Z}^{\text{scan}}(k_{z0})$ such that

$$\mathbf{S}^{\text{scan}}(k_{z0}) = \left(\mathbf{Z}^{\text{scan}}(k_{z0}) - Z_0\mathbf{I}\right)\left(\mathbf{Z}^{\text{scan}}(k_{z0}) + Z_0\mathbf{I}\right)^{-1}. \tag{4.3}$$

Since for each scan angle the matrix in (4.3) is diagonal, it may be decoupled into N scalar equations of the form

$$\Gamma_n^{\text{scan}}(k_{z0}) = \frac{Z_n^{\text{scan}}(k_{z0}) - Z_0}{Z_n^{\text{scan}}(k_{z0}) + Z_0}, \tag{4.4}$$

with the *scan reflection coefficient* $\Gamma_n^{\text{scan}}(k_{z0})$ for element n (at scan angle k_{z0}) corresponding to the nth diagonal entry of $\mathbf{S}^{\text{scan}}(k_{z0})$. This term captures the effective ratio of the signal returned back along the feed line to the original signal w_n. Because the scan reflection coefficient is a function of $Z_n^{\text{scan}}(k_{z0})$, which includes the effects of coupling for all N array elements, this reflection is in reality a superposition of both the incident signal at the element as well as the coupled signals from the other $N-1$ elements. As such, (2.8) can be expressed as the array *scan efficiency*

$$\begin{aligned}\eta^{\text{scan}}(k_{z0}) &= 1 - \frac{\left\|\mathbf{S}^{\text{scan}}(k_{z0})\mathbf{w}(k_{z0})\right\|^2}{\left\|\mathbf{w}(k_{z0})\right\|^2} \\ &= 1 - \frac{\sum_{n=0}^{N-1}\left|\Gamma_n^{\text{scan}}(k_{z0})w_n(k_{z0})\right|^2}{\sum_{n=0}^{N-1}\left|w_n(k_{z0})\right|^2}. \qquad (4.5)\end{aligned}$$

Using the scalar equivalent for the element impedance in (4.2), it is possible to match each element such that $Z_n^{\text{scan}}(k_{z0}) = Z_0$ in the same way one would match a single antenna. However, since this scan impedance is only valid at k_{z0}, when the beam is scanned to any other angle, the change in scan impedance results in a loss of efficiency. As element spacing decreases, it is to be expected that mutual coupling effects become more prevalent, yet these effects are not necessarily disadvantageous to the power efficiency. In fact, as the array scans from one direction to another, the incremental phase change between neighboring elements is inversely proportional to their spacing, and thus we can expect the scan impedance to be *less* sensitive to changes in the scan direction. This motivates the use of *scan impedance matching*, in which the array is matched to the scan impedance in one specified direction. This sub-optimal matching technique is applied with the expectation that the scan impedance does not vary greatly over the entire range of potential scan angles. Based on the above observation, this implies that this very simple approach is particularly well suited for use with dense arrays.

To develop the idea, the scan impedance matching approach was applied to an array of length $L = 20\lambda$ using the impedance matrix values obtained from (4.1) for several density ratios. The scan impedances of the unmatched array elements were calculated using (4.2) for the broadside scan direction of the array, $k_{z0} = 0$, and an individual matching network consisting of a series reactance and a quarter-wave transmission line was applied at each element to match these impedances to the normalized system impedance $Z_0 = 1$. The resulting average matched scan impedances are shown in Figure 4-4 for both a standard ($R = 1$) and dense ($R = 2$) array. At $k_{z0} = 0$, both arrays have scan impedances with real parts equal to the system impedance Z_0 and zero imaginary parts, corresponding to a perfect match. However, away from broadside, the standard array scan impedance exhibits a greater sensitivity to changes in scan angle than seen for the dense array, as expected.

Efficiency Effects Due to ΔΣ Weights

In addition to the effect of the increased element density on the power efficiency, we must consider the effect of using the ΔΣ weights instead of the ideal array weights. In particular, we characterize the fractional reduction of the ΔΣ array efficiency $\hat{\eta}$ from the efficiency η of the equivalent array excited by ideal (unquantized) weights

$$\rho = \frac{\eta}{\hat{\eta}}. \qquad (4.6)$$

Consider an array with the matching network in place, some set of ideal weights $\{w_n\}$ with associated ΔΣ weights $\{\hat{w}_n\}$, and assume that the array is sufficiently dense such that

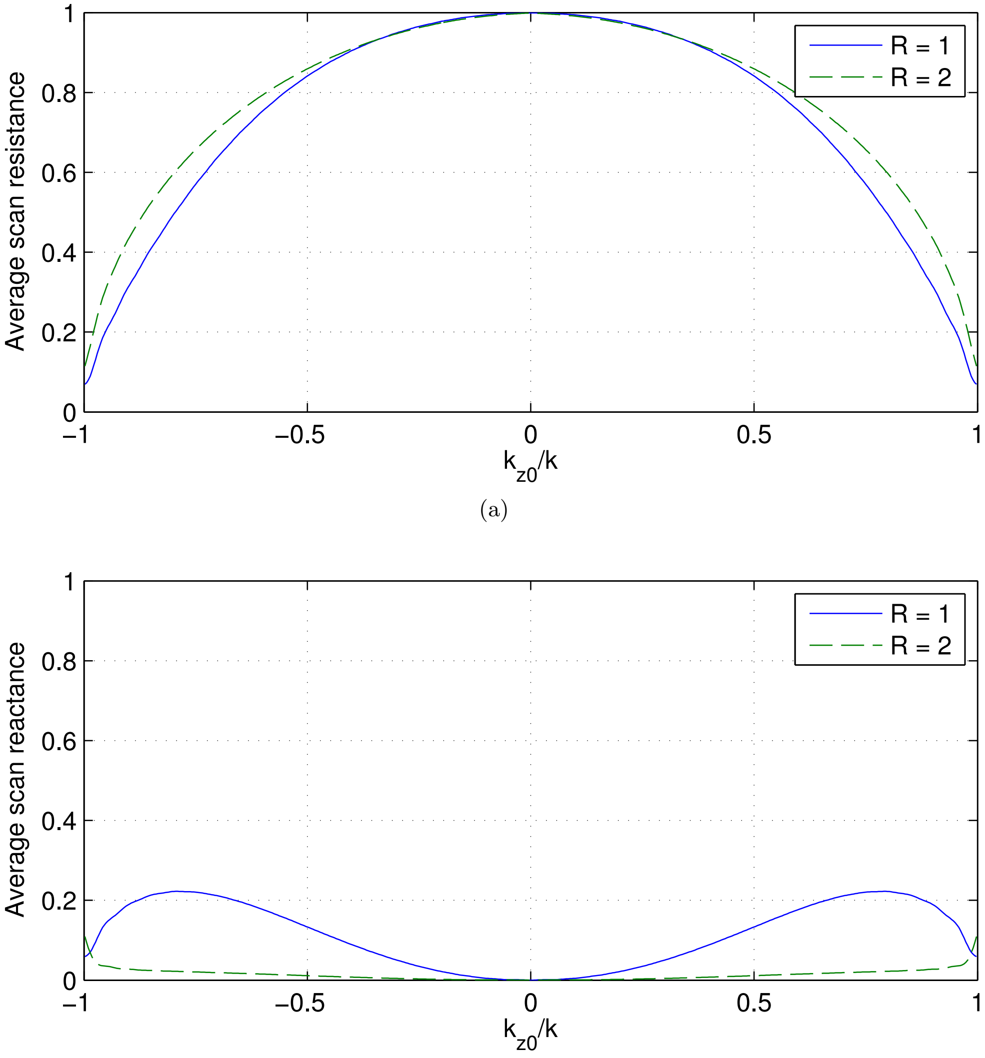

(a)

(b)

Figure 4-4: (a) Real part and (b) imaginary part of the average scan impedance of elements in an array of length $L = 20\lambda$, for density ratios $R = 1$ and $R = 2$. Calculations include scan impedance matching network designed for perfect match to $Z_0 = 1$ at $k_{z0} = 0$.

the beam patterns are nearly identical. Since the total power radiated is proportional to the power pattern integrated over real space, it follows that $\hat{P}_{\text{rad}} \approx P_{\text{rad}}$. To obtain similar patterns, the ratio of the magnitudes of the $\Delta\Sigma$ weights to those of the ideal weights, $\gamma = \hat{a}/a$, must be greater than unity in order to steer the pattern distortions into imaginary space. Therefore, from (2.7) it follows that $\hat{P}_{\text{inc}} > P_{\text{inc}}$. Using the definition of the power efficiency in (2.5), we can estimate the efficiency loss in the case of low pattern noise as

$$\rho_{\text{est}} = \frac{\hat{a}^2}{a^2} = \gamma^2 > 1. \tag{4.7}$$

Put simply, the $\Delta\Sigma$ excitations as expressed in (3.23) radiate the same amount of power as in the case of the ideal excitations due to the w_n terms, while the quantization terms q_n radiate zero power once their beam pattern contributions are effectively steered from real space. Hence, we can expect the efficiency of the $\Delta\Sigma$ array to be less than that of an identical array excited with ideal weights. The exact amount depends on the choice of γ, which as we will discuss shortly, also plays a role in how quickly the $\Delta\Sigma$ pattern converges to the desired pattern.

For example, in the patterns and SQNR results presented thus far, the $\Delta\Sigma$ weights were determined by setting $\gamma = 1.26$. When the quantization noise is relatively small, such as in Figure 3-9(c), the power radiated using both the ideal and $\Delta\Sigma$ weights is nearly identical, while the total power incident on the array is a factor of $\gamma^2 \approx 1.59$ greater in the $\Delta\Sigma$ case.

Eq. (4.7) implies we should expect to see a reduction in the $\Delta\Sigma$ power efficiency of γ^2, corresponding to a 2 dB power efficiency loss. Exact efficiency results calculated for $R = 4$ are shown as a function of scan angle for both the ideal and the $\Delta\Sigma$ weights in Figure 4-5. These results were calculated directly from (2.8) with a scan impedance match network tuned to a perfect match for the ideal weights at $k_{z0} = 0$. We first note from the ideal excitation results that the scan impedance matching works quite well for the dense array, with nearly negligible efficiency losses for scan angles throughout the region $|k_{z0}| \leq 0.5k$ (corresponding to ±60° from the array broadside). Further, the predicted power efficiency reduction of 2 dB shows a very good agreement with the $\Delta\Sigma$ array results. The fluctuations seen in the $\Delta\Sigma$ results are due to varying levels of pattern noise for different scan angles, which affect the assumption that the radiated power is equal to that of the ideal weights. Similar calculations for increased density ratios had less variations, since the quantization noise was lower throughout the visible region.

Inclusion of a matching network has the additional effect of altering the coupling matrix $\mathbf{C}$ relating the free excitations to the currents across the terminals of the array elements. As such, it is necessary to revisit the SQNR performance of the $\Delta\Sigma$ array to reflect these changes. Analysis of the combined network (see 4.A for a detailed derivation) yields the matched coupling matrix

$$\mathbf{C}_M = -j\left(\mathbf{Z}_t + Z_0\mathbf{Z}_t^{-1}(\mathbf{Z} - j\mathbf{X}_s)\right)^{-1}, \tag{4.8}$$

where $\mathbf{Z}_t$ is a diagonal matrix containing the characteristic impedances of the quarter-wave transmission lines used to match the real part of the element impedances and $\mathbf{X}_s$ is a diagonal matrix containing the reactances of the components used to match the imaginary part of the element impedances.

When the matched coupling matrix is used in place of the original coupling matrix in the SQNR calculations, the results are as shown in Figure 4-6. Interestingly, the matching

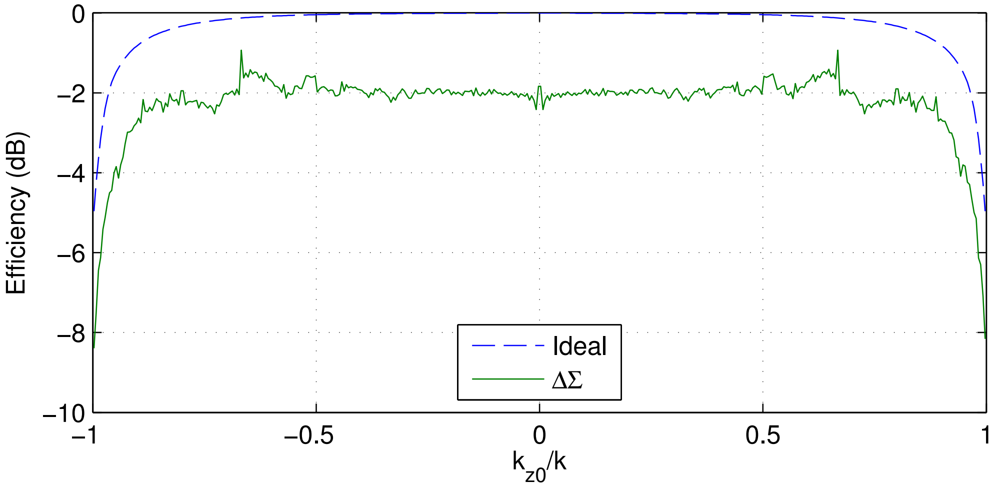

Figure 4-5: Power efficiency as a function of scan angle k_{z0}, $L = 20\lambda$, $R = 4$, with scan impedance matching network designed for perfect match at $k_{z0} = 0$. Results for the $\Delta\Sigma$ array obtained by setting $\hat{a} = 1.26a$ such that the nominal efficiency is within approximately 2 dB of the ideal result.

network appears to have the added benefit of improving the ability of the $\Delta\Sigma$ array to produce desired beam patterns. Closer inspection of the embedded element patterns with and without the matching network verifies that the matched array embedded element patterns show considerably less variation near the edge of the array than in the unmatched case. This observation supports the earlier conjecture that such variations were responsible for the slight decrease in the SQNR for the unmatched free excitations seen in Figure 4-3.

Based on (4.7), it may be tempting to select an arbitrarily low value for γ in order to minimize efficiency losses. However, since this estimate is obtained by assuming that $\hat{P}_{\text{rad}} = P_{\text{rad}}$, it is necessary to determine the array efficiencies directly from (2.8) to obtain the exact dependence of ρ on the choice of γ. Exact values of ρ were calculated for different density ratios R with the value of γ varying from 1 to $\sqrt{2}$ (0 to 3 dB estimated power efficiency loss). Figure 4-7 shows the resulting nominal value of ρ, averaged over uniformly distributed scan angles, over the range of γ. These results demonstrate that as γ approaches unity, the exact efficiency loss values are quite different that the estimated loss found using (4.7). This indicates not only that the efficiency loss cannot be made arbitrarily small, but also that small values of γ result in greater pattern distortion, thereby affecting the SQNR as well as ρ.

The results in Figure 4-7 also demonstrate that the relationship between the $\Delta\Sigma$ array efficiency and γ depends on the particular value of R. Specifically, the value of γ at which each curve intersects with the estimated result increases with R, implying that it may be necessary to accept additional efficiency loss to obtain the maximum achievable SQNR as the density ratio of the $\Delta\Sigma$ array is increased. This interpretation is verified by the results shown in Figure 4-8, in which the SQNR for the $L = 20\lambda$ array is plotted against the efficiency loss ρ as γ is varied over the same range as in Figure 4-7 for a number of density ratios. The horizontal dashed grey line shows the SQNR of a standard array of the same length utilizing the same two-bit phase shifters used in the $\Delta\Sigma$ array. As would be expected, this value represents a lower bound on the $\Delta\Sigma$ results for low density ratios.

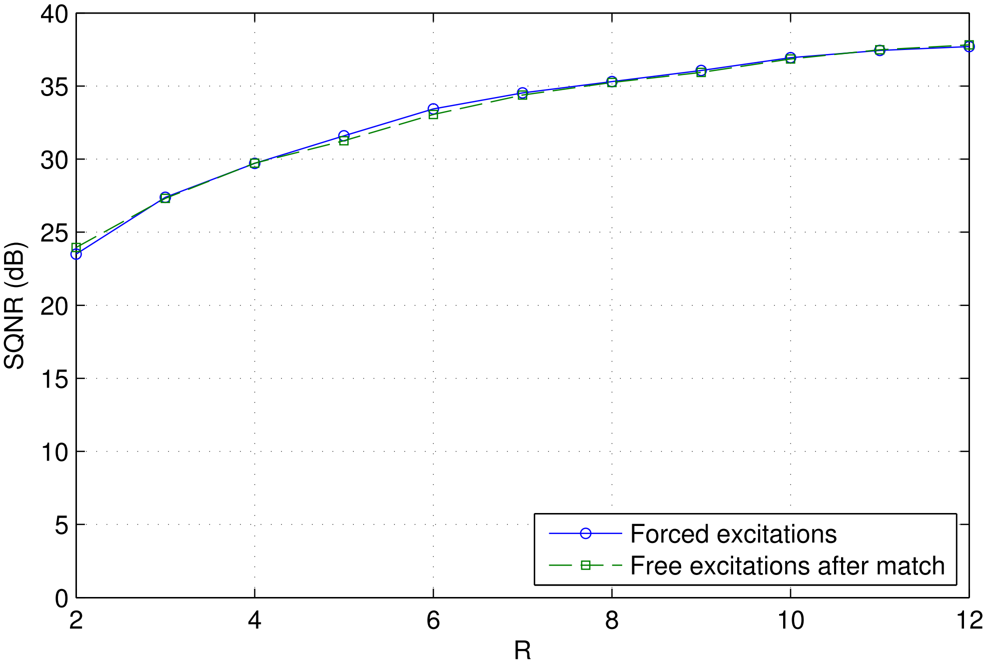

Figure 4-6: SQNR dependence on density ratio R for $\Delta\Sigma$ arrays using forced excitations and free excitations with matching network designed for ideal match at $k_{z0} = 0$. Array length $L = 20\lambda$.

The asymptotic limit shared by all values of R as ρ decreases, shown by the slanted light grey dashed line, represents the maximum signal-to-quantization-noise level $\text{SQNR}_{\rho}^{\max}$ that can be obtained for a specified efficiency loss, regardless of how large the density ratio is. Comparison of the results in Figure 4-8 with those generated for other array lengths show both dashed lines having a vertical shift proportional to the fractional change in length. This is to be expected, based simply on the linear change in the number of elements in both cases. Since the vertical shift maintains the slope of the line representing the $\text{SQNR}_{\rho}^{\max}$, found by a linear fit to be $\Delta\text{SQNR}_{\rho}^{\max}(\text{dB})/\Delta\rho(\text{dB}) = 10.8$, we may express the dependence of $\text{SQNR}_{\rho}^{\max}$ on both ρ and L (in linear scale) as

$$\text{SQNR}_{\rho}^{\max} = 2.3\rho^{10.8}L. \tag{4.9}$$

Similarly, we define $\text{SQNR}_{R}^{\max}$ as the maximum SQNR achievable for a given density ratio. This can be expressed in a similar fashion as in (4.9), i.e.,

$$\text{SQNR}_{R}^{\max} = cR^{\alpha}L \tag{4.10}$$

for some c. However, the complex dependence on the array edge effects, the specific value of γ, and a constraint on the efficiency loss to somewhat reasonable values given by $\rho \leq 2$ causes the exponent α to vary from about 2 at lengths of just a few wavelengths to about 2.5 at $L = 20\lambda$, increasing slowly for greater lengths. A more appropriate indication of the behavior of $\text{SQNR}_{R}^{\max}$ can be found from the relation given by (3.27), in which the array length $L = N_0 d_0$ and associated edge effects are treated explicitly, while the effect

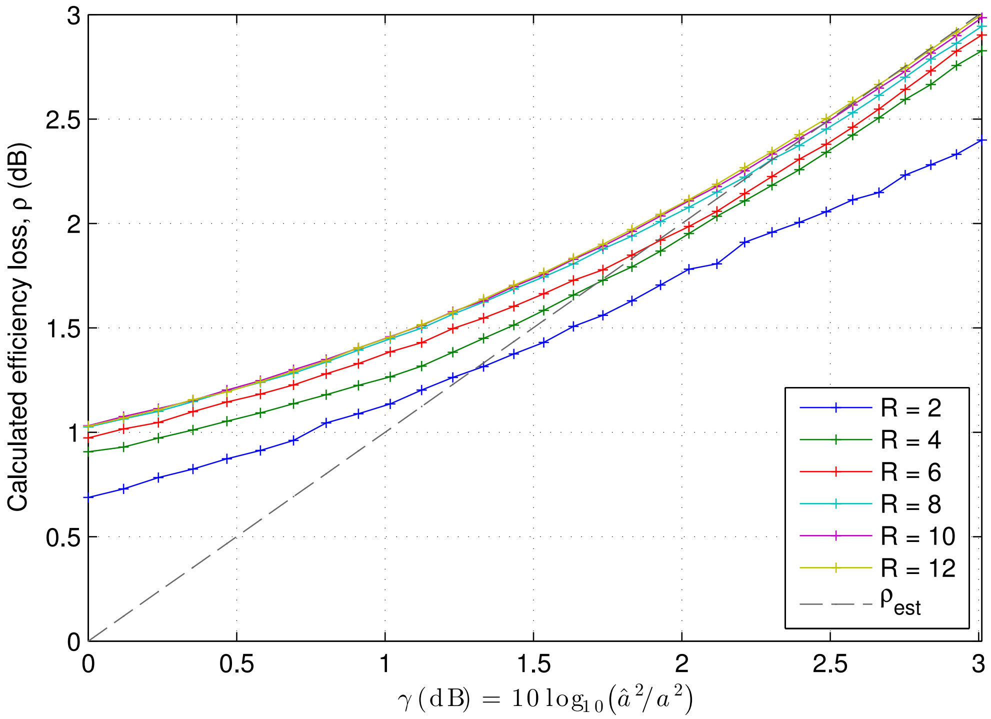

Figure 4-7: Nominal power efficiency loss versus the ratio of the $\Delta\Sigma$ and ideal array weight magnitudes $\gamma = \hat{a}/a$. The dashed grey line shows the corresponding estimated value of ρ given by (4.7).

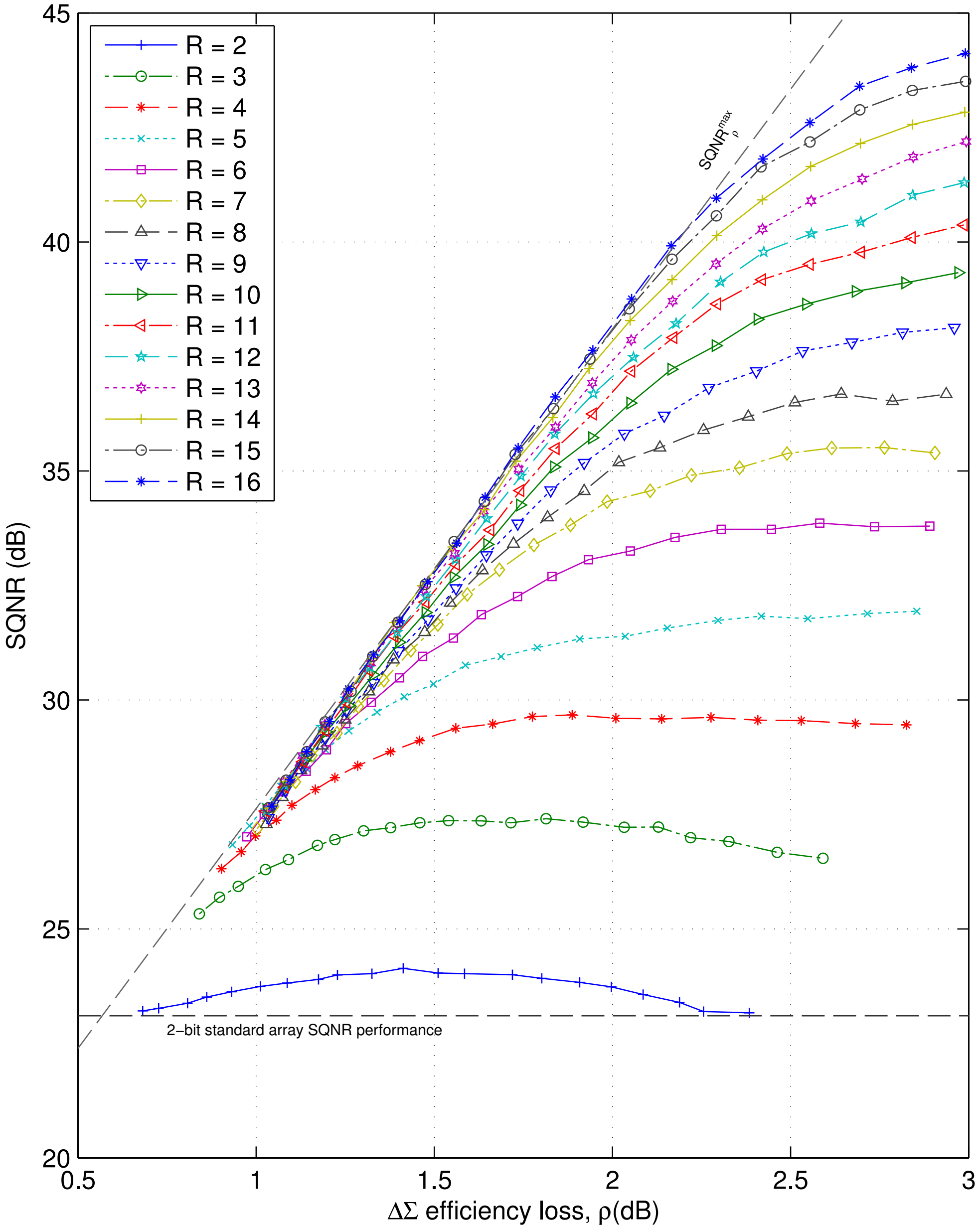

Figure 4-8: SQNR versus power efficiency loss for the length $L = 20\lambda$ array.

Table 4.1: Comparison of several array configurations for $\Delta\Sigma$ arrays of length $L = 20\lambda$.

R	N	γ	SQNR (dB)	ρ (dB)
2	80	1.07	23.6	0.9
3	120	1.09	26.8	1.2
4	160	1.15	28.9	1.4
5	200	1.19	30.7	1.6
6	240	1.23	32.6	1.8

of γ is captured by the average quantization excitation noise σ_q^2. From simulated results, at lengths greater than $L = 4\lambda$, the calculated value of $\text{SQNR}_R^{\text{max}}$ is closely approximated using the result given by (3.27) with $\sigma_q^2 = 0.9$.

While the particular aspects of the intended application of any system ultimately governs the relative value of such important metrics as hardware costs, pattern precision, and power efficiency, the results shown in Figure 4-8 clearly suggest that each particular density ratio has some range of natural operating points, outside of which the tradeoff required to improve one metric requires an unreasonable sacrifice with regard to the other. As an example, consider the curve corresponding to $R = 4$ at the point where $\rho = 1.4$ dB. In the neighborhood surrounding this operating point, the choice of γ may be adjusted to accommodate an improvement in either the SQNR or the power efficiency at a reasonable cost with regard to the other. However, such costs increase rapidly as the curve approaches either of the maximum SQNR asymptotes described above. As such, if it appears necessary to operate near one of these boundaries, this simply suggests that selecting an alternative density ratio is likely to be a more efficient use of resources. Several candidate designs for $R = 2$ to $R = 6$ are illustrated in Table 4.1 in which the particular choices of γ correspond to operational points close to the center of this natural tradeoff range for each density ratio.

4.3 Wideband Performance

The impedance characteristics of densely packed arrays are less sensitive to changes in frequency. As a result, a dense array can be utilized as a means of obtaining a greater operational bandwidth than would be achieved with a standard array. However, this benefit is typically not exploited due to the additional costs associated with the increase in the number of array elements. This observation provides a separate motivation for the $\Delta\Sigma$ array, namely, a low cost approach for building dense arrays. Further, while the narrowband efficiency analysis described in Section 4.2 indicates an unavoidable loss for the $\Delta\Sigma$ array when compared to a standard array, a wideband view tells a different story.

In order to investigate this frequency dependent behavior, the mutual impedance between two parallel thin-wire dipoles of the same length l with spacing d along the same axis is modeled using [41]

$$Z = \frac{15}{S^2} \sum_{m=-2}^{2} \sum_{n \in \{-1,1\}} A_m \exp[-jknml/2] E(k\beta) \tag{4.11}$$

where

$$\beta = \sqrt{(ml/2)^2 + d^2} - nml/2 \tag{4.12}$$

and

$$\begin{aligned} A_{-2} &= A_2 = 1, \\ A_{-1} &= A_1 = -4\cos kl/2, \\ A_0 &= 2(1 + 2\cos^2 kl/2), \\ S &= \sin kl/2 \end{aligned}$$

and $E(\cdot)$ is the exponential integral ($Ei(x) = Ci(x) - jSi(x)$). The frequency dependence is contained in $k = 2\pi/\lambda$.

The impedance matrix $\mathbf{Z}$ is formed and a matching network is designed for scan direction $k_{z0} = 0$ at the center frequency f_0 by first determining the scan impedances

$$Z_n^s = \frac{v_n}{i_n} = \frac{\sum_m Z_{nm} i_m}{i_n} \tag{4.13}$$

with $i_n = \exp jnk_{z0}d = 1$, then connecting series reactances $X_{s,n} = \mathrm{Im}(Z_n^s)$ and quarter-wave transmission line with characteristic impedance $Z_{t,n} = \sqrt{\mathrm{Re}(Z_n^s)Z_0}$ resulting in the new matched impedance matrix

$$\mathbf{Z}_m = (\cos\alpha\mathbf{I} + j\sin\alpha(\mathbf{Z} - j\mathbf{X}_s)\mathbf{Z}_t^{-1})^{-1}(j\sin\alpha\mathbf{Z}_t + \cos\alpha(\mathbf{Z} - j\mathbf{X}_s)) \tag{4.14}$$

with $\mathbf{Z}_t$ and $\mathbf{X}_s$ both diagonal and $\alpha = \frac{\pi f}{2f_0}$.

Numerical simulations were run for an array of length $L = 20\lambda$ to calculate the average scan efficiency using both ideal (unquantized) excitations and $\Delta\Sigma$ excitations. Referring to the results shown in Figure 4-9, the standard array ($R = 1$) with ideal excitations is relatively narrow band, having a 3 dB fractional bandwidth of about 17%, while for the dense ($R = 4$) ideal excitation case this rises well above 50%. For the $\Delta\Sigma$ case, the excitations were chosen with a quantization amplitude corresponding to a nominal loss of about 1.5 dB. As such, its performance falls below the standard array case at the center frequency f_0. However, the variation with frequency is quite similar to the ideal case with the resulting bandwidth being about 45% — nearly three times greater than the standard dipole array.

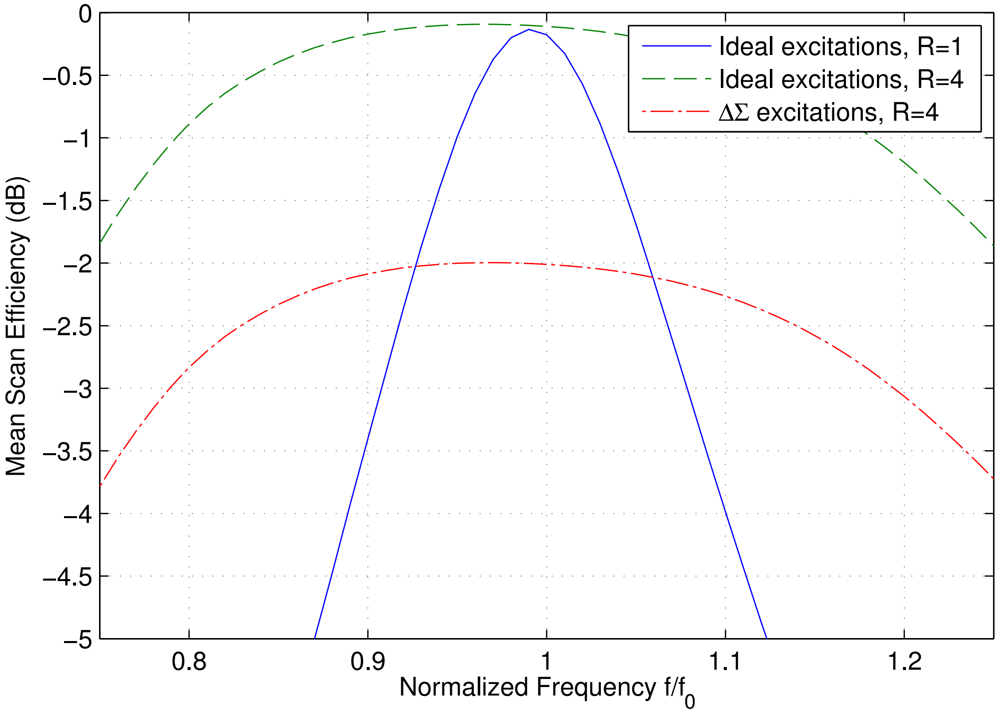

Figure 4-9: Wideband efficiency performance results from numerical simulations for array length $L = 20\lambda$.

4.A Matched Array Coupling Matrix Derivation

Referring to Figure 2-3, the matching network at element n is introduced by connecting a quarter wavelength transmission line with characteristic impedance Z_{tn} to source w_n, followed by a series reactance $-jX_{sn}$, which in turn connected to the antenna terminals. Following standard microwave network analysis (see, e.g., [37] for additional details), the voltage and current at the input to the network are related to the voltage and current at the antenna terminals by

$$\begin{aligned} v_n^{in} &= jZ_{tn}i_n && (4.15)\\ i_n^{in} &= jZ_{tn}^{-1}(v_n - jX_{sn}i_n), && (4.16) \end{aligned}$$

and to the source excitations by

$$w_n = v_n^{in} + Z_0 i_n^{in}. \tag{4.17}$$

Letting $\mathbf{w}$, $\mathbf{v}^{in}$, $\mathbf{i}^{in}$, $\mathbf{v}$, and $\mathbf{i}$ be length-N complex vectors associated with the above scalar quantities, and similarly organizing the the match network quantities into $N \times N$ diagonal matrices $\mathbf{Z}_t$ and $\mathbf{X}_s$, these relations may be combined to include the complete array

$$\begin{aligned} \mathbf{v}^{in} &= j\mathbf{Z}_t\mathbf{i}, && (4.18)\\ \mathbf{i}^{in} &= j\mathbf{Z}_t^{-1}(\mathbf{v} - j\mathbf{X}_s\mathbf{i}), && (4.19)\\ \mathbf{w} &= \mathbf{v}^{in} + Z_0\mathbf{i}^{in}. && (4.20) \end{aligned}$$

As the matching network will not effect the impedance relations occurring outside of the array, the original impedance relation $\mathbf{v} = \mathbf{Zi}$ remains valid. Using this additional relationship, we can make the following operations

$$\begin{aligned} \mathbf{w} &= j\mathbf{Z}_t\mathbf{i} + jZ_0\mathbf{Z}_t^{-1}(\mathbf{v} - j\mathbf{X}_s\mathbf{i})\\ &= j\left(\mathbf{Z}_t + Z_0\mathbf{Z}_t^{-1}(\mathbf{Z} - j\mathbf{X}_s)\right)\mathbf{i}. && (4.21) \end{aligned}$$

Having eliminated all other voltage and current terms, this last expression may be rewritten as $\mathbf{i} = \mathbf{C}_M\mathbf{w}$, where

$$\mathbf{C}_M = -j\left(\mathbf{Z}_t + Z_0\mathbf{Z}_t^{-1}(\mathbf{Z} - j\mathbf{X}_s)\right)^{-1}. \tag{4.22}$$

Chapter 5

Delta-Sigma Measurements

Measurements were taken to demonstrate the practical viability of the $\Delta\Sigma$ array with the objective of showing that $\Delta\Sigma$ beamforming behaves in a manner consistent with our development and analysis. The test array, shown in Figure 5-1, and measurement facilities were made available by MIT Lincoln Laboratory.

To facilitate the ability to compare any number of parameters, our measurements included the individual element patterns as well as the mutual coupling between each pair of elements, given by the array S-parameters. From these, it is possible to determine the beamformed pattern and power efficiency for arbitrary excitations. In order to keep the number of measurements at a manageable level, the measurements were limited to a single column of elements. From the measured results we examined the beamformed patterns for both the ideal and $\Delta\Sigma$ excitations at a number of scan directions and used these results to determine whether the dependence of the 2-bit $\Delta\Sigma$ quantization technique on the density ratio behaved in a manner constant with the analysis developed in the preceding chapters.

5.1 Measurement Description

The 12 element by 12 element array was originally designed to provide coverage over a scan region of ±25° in both azimuth and elevation over an operational bandwidth of 6-18 GHz. In order to utilize this existing hardware as a dense array, our measurements were performed below the intended frequency bandwidth over the band from 4 to 6 GHz. The uniform spacing between the array elements is $d_0 = 200$ mil, corresponding to a $\lambda/2$ spacing at $f_0 = 14.76$ GHz. With this element spacing, our results represent a density ratio that varies from $R = 2.46$ at 6 GHz to $R = 3.69$ at 4 GHz.

For these measurements, the array was attached to a conductive ground plane and mounted on a gimbaled post in an anechoic antenna measurement chamber, as shown in Figure 5-2. To obtain the pattern within the plane containing the 12x1 column of elements, the array was rotated 90° from the layout shown in Figure 5-1. (This choice was made due to a damaged connection in a single element in both of the central horizontal rows of the array.)

A separate set of measurements was taken for each of the 12 elements. In each case, the test element was connected to measurement facility hardware with the remaining 11 elements match-terminated with a 50 Ω load – the appropriate match connection to allow for the use of superposition from which the beamforming capability of the array will be analyzed.

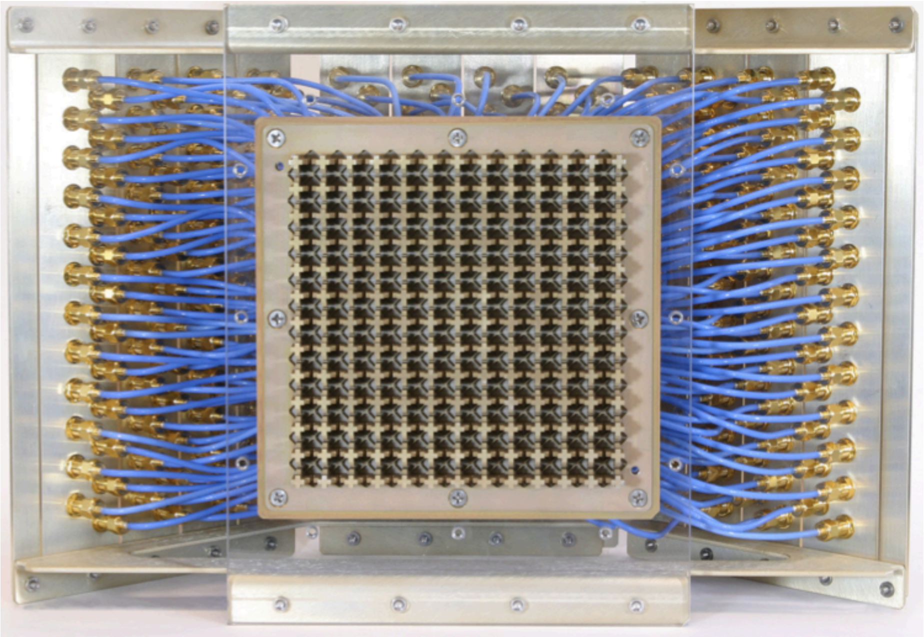

Figure 5-1: 12 x 12 array used for measurements.

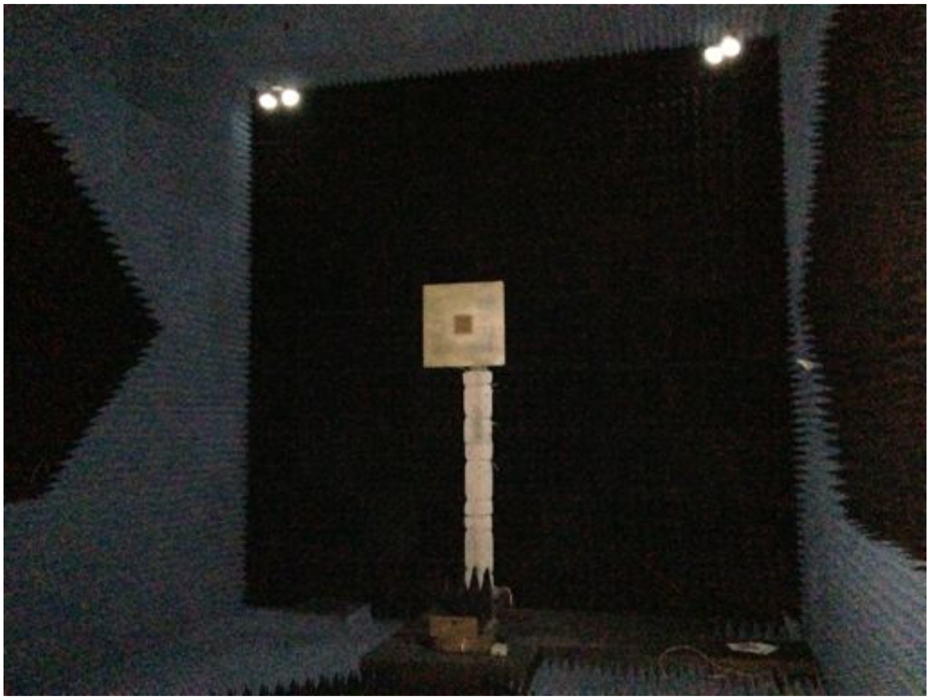

Figure 5-2: Mounted test array in anechoic antenna measurement chamber.

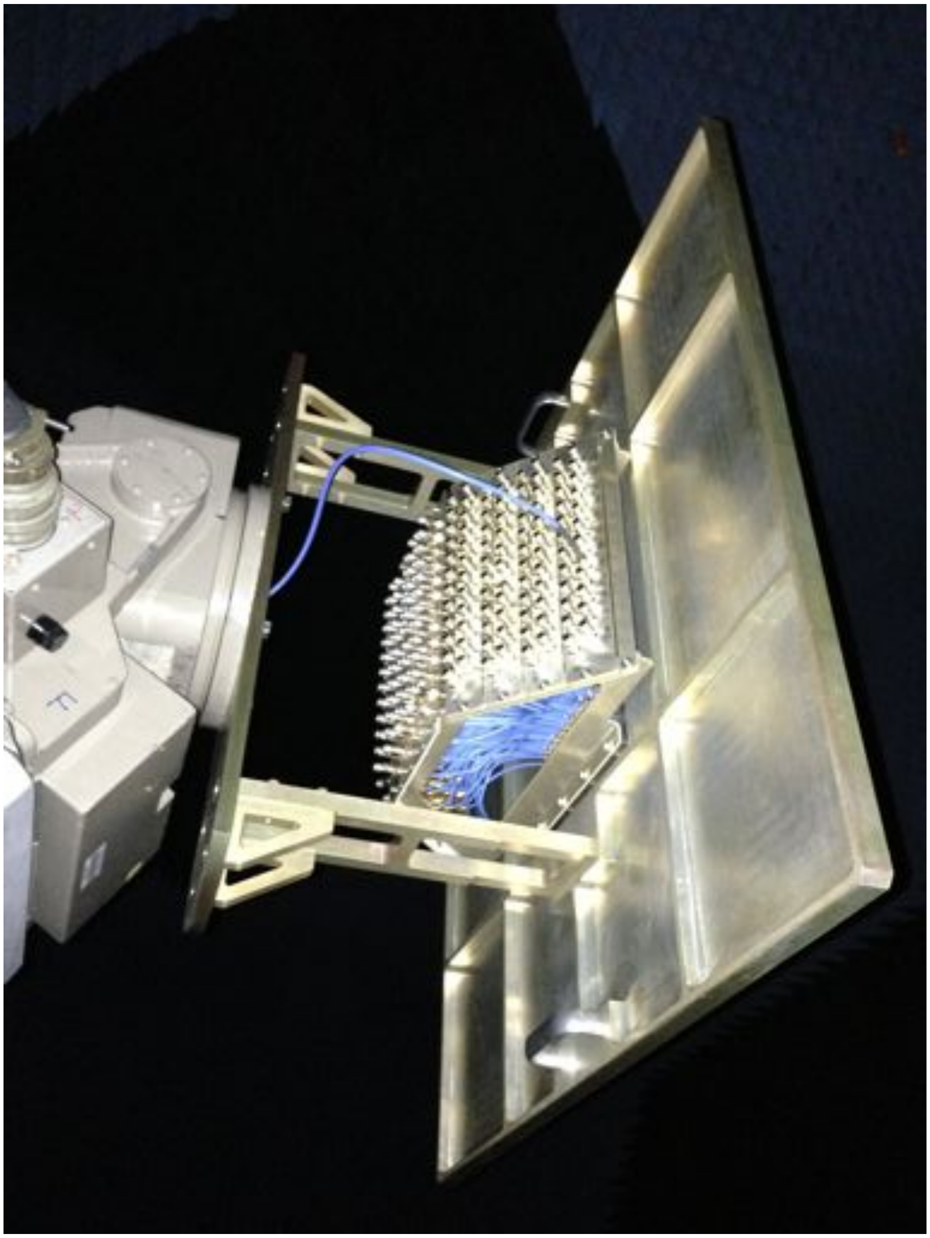

Figure 5-3: Single element gain measurement connection.

Prior to these measurements, a calibration antenna was mounted to determine the signal attenuation and phase variations over our measurement bandwidth. With this calibration the measurement was able to record the element *gain* pattern as well as the element phase pattern. The gain pattern is proportional to the power pattern of the array, but it is a more useful metric in a practical sense, as it accounts for both the directive properties of the beam pattern as well as the power efficiency of the array.

The raw measured element gain and phase patterns for the 12 elements at f =4, 5, and 6 GHz are shown in Figures 5-4, 5-5, and 5-6. In each case, the legend refers to the patterns of the upper half of the array, elements 1 through 6, shown as solid lines. Elements 7 to 12 are shown as dashed lines with each element having the same color as its symmetric counterpart (e.g. elements 1 and 12 both shown in red). The units of gain, dBi, specifies the gain as compared to the hypothetical isotropic antenna.

From these gain patterns, it is clear to see that the array elements are not originally intended for use at these frequencies. In particular, many of the patterns are strongest in directions more than 60° from the array broadside. However, this is not troublesome for our present purpose of demonstrating $\Delta\Sigma$ beamforming. On the other hand, the variations between the patterns of adjacent elements will affect the ability to cancel the quantization errors. In fact, while the patterns at 4 GHz have particularly poor gains at broadside, they are the most consistent from element to element, implying that this frequency is more favorably suited than the higher frequencies for effective error cancellation in this sense. It is also worth noting that the behavior of the phase patterns differs from the linear phase responses associated with isotropic elements. Consequently, the phases required for coherent beamforming need be adjusted accordingly, as will be discussed in the following section.

5.2 Analysis and Results

For a given set of element weights w_n and element patterns with gain $G_n(\theta)$ and phase $\varphi_n(\theta)$, the combined array gain is given by (see Appendix 5.A for details)

$$G(\theta) = \frac{|\sum_n w_n \sqrt{G_n(\theta)} e^{j\varphi_n(\theta)}|^2}{\sum_n |w_n|^2}. \tag{5.1}$$

When scanning the main beam to θ_0, instead of the linear phase progression that was used in the case of the arrays of isotropic elements, it is preferable to apply the *conjugate phase match* to the element phase pattern at the specified scan angle. In particular, we apply the (normalized) uniform amplitude array weights

$$w_n = \frac{1}{N} e^{-j\varphi(\theta_0)}, \quad n = 0, 1, \ldots, N-1. \tag{5.2}$$

As discussed earlier, the $\Delta\Sigma$ quantized weight selection algorithm requires both the set of weights $\{w_n\}$ and the fixed magnitude of the quantized weights $|\hat{w}_n| = \hat{a}$. For the case of uniform amplitude array weights, as in (5.2), this was specified by the amplitude ratio $\gamma = \hat{a}/a$, where $a = |w_n| = 1/N$ in this case. Recall that the choice of γ was manifest as a trade off between the array efficiency and the SQNR, and that we used $\gamma = 1.26$ in the numerical simulations, unless otherwise noted. This was chosen to yield good SQNR performance over a wide range of density ratios, while holding the $\Delta\Sigma$ efficiency loss to about 2 dB.

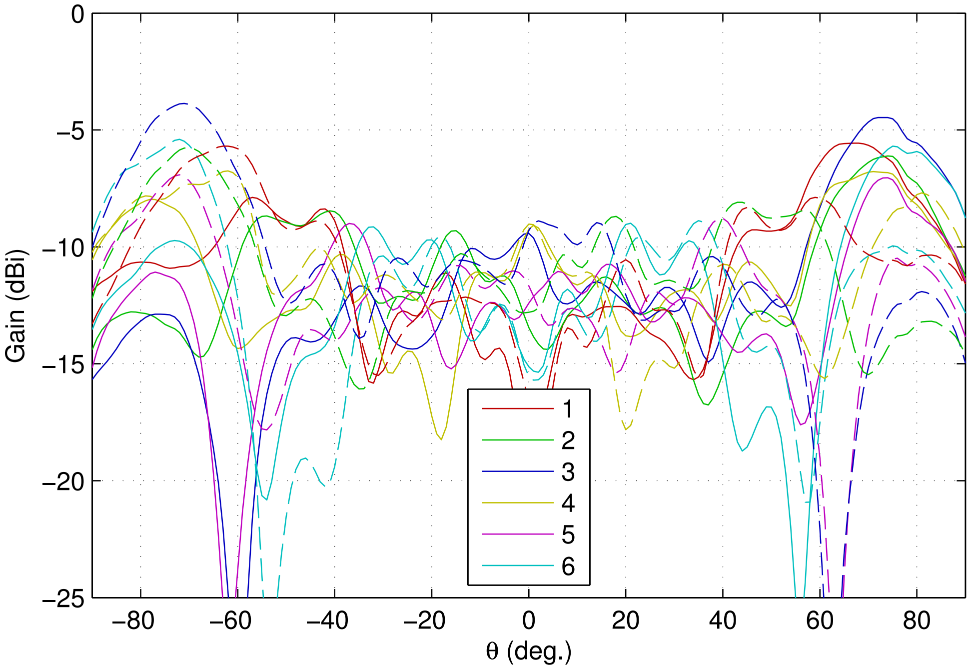

(a)

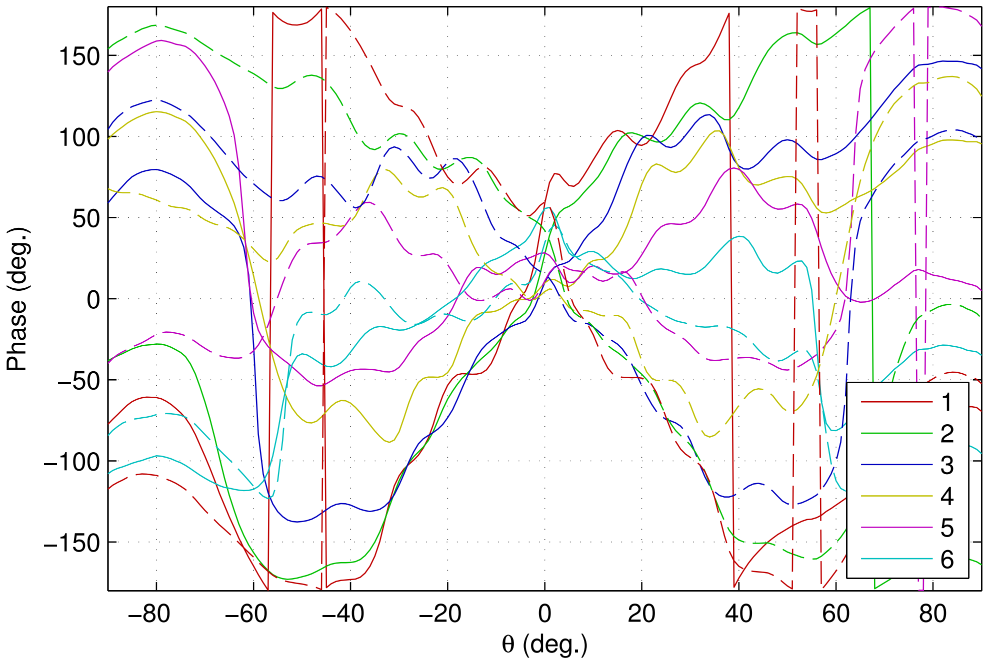

(b)

Figure 5-4: Measured element (a) gain and (b) phase patterns at 4 GHz.

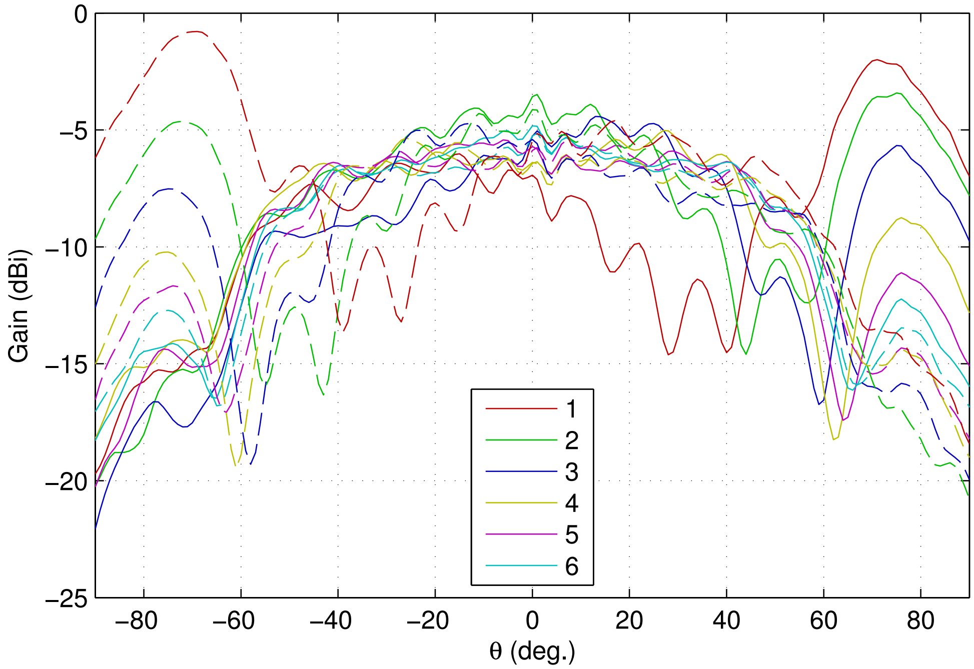

(a)

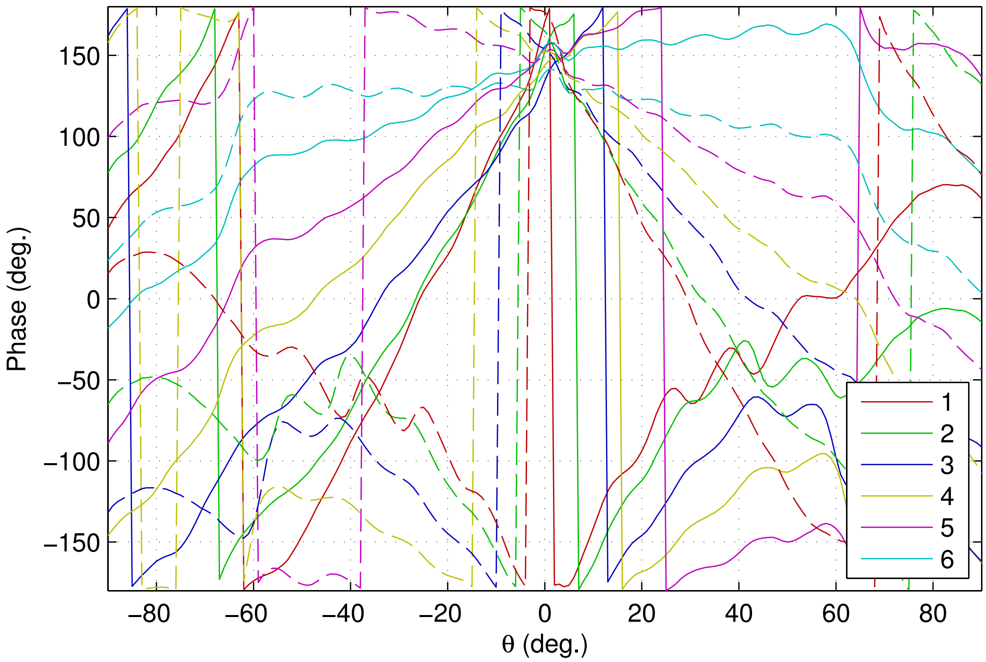

(b)

Figure 5-5: Measured element (a) gain and (b) phase patterns at 5 GHz.

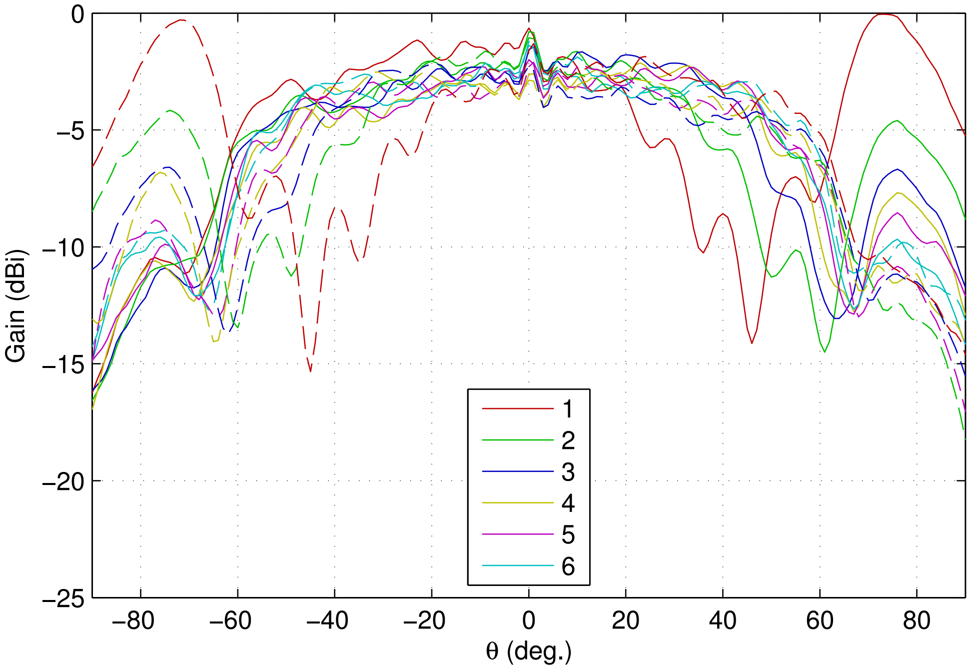

(a)

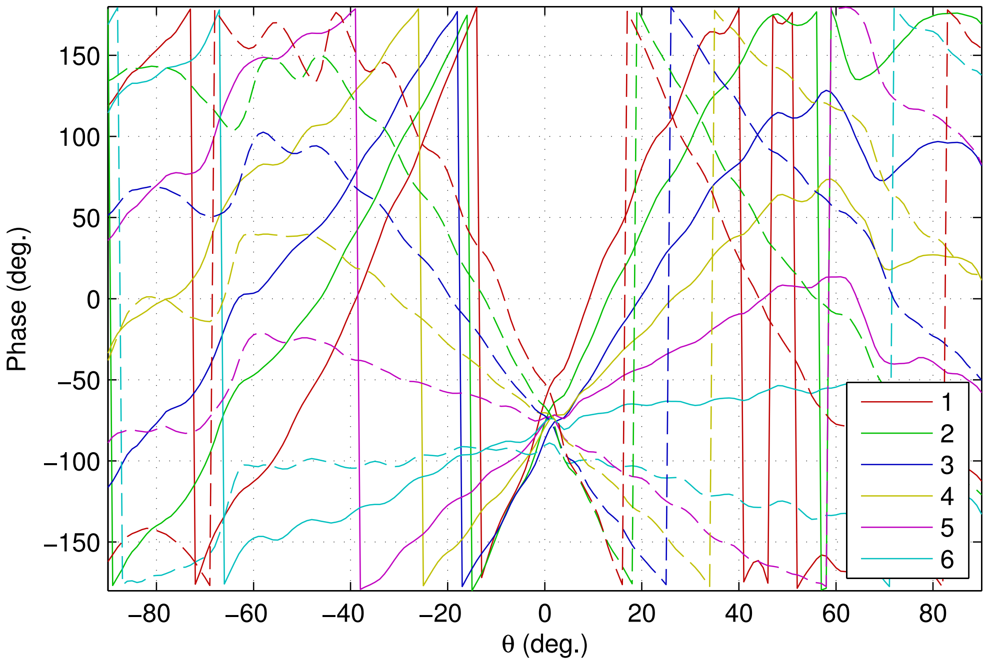

(b)

Figure 5-6: Measured element (a) gain and (b) phase patterns at 6 GHz.

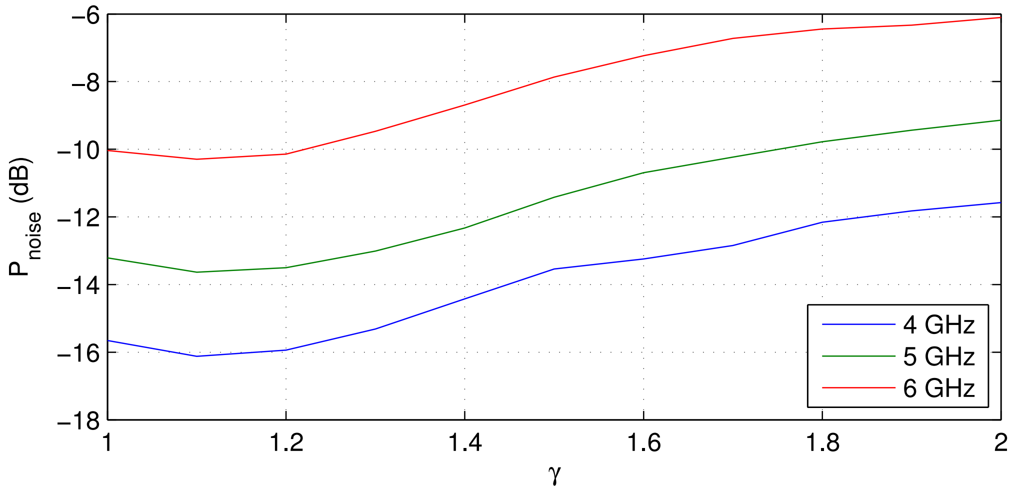

Figure 5-7: Average quantization noise power dependence on the ΔΣ amplitude ratio γ for the measured array.

Using the measured element gain patterns for 4, 5, and 6 GHz, the mean quantization noise power P_{noise} was determined from the mean square error between the patterns of the ideal (unquantized) and ΔΣ weights, averaged over 200 scan angles θ_0 selected at random. Repeating this calculation while varying the ΔΣ weight amplitude over the range $1 \leq \gamma \leq 2$, we obtain the results shown in Figure 5-7.

The results at each frequency indicate that a more modest value of approximately $\gamma = 1.1$ (with an expected efficiency loss of 0.83 dB) appears optimal, which is most probably due to the following reasons. First, the utility of larger values of γ is apparent only for high density ratios, as evidenced by Figure 4-8. At the frequency range of these measurements, the density ratio falls within the range $2.46 \leq R \leq 3.69$, at which the improvement in SQNR with γ sees diminishing returns well before the 2 dB efficiency loss point. Second, the reasoning behind the need for higher values of γ was that as the element spacing is decreased, the small, constant linear phase progression applied to the isotropic array elements led to non-trivial correlation between w and q. With the measured results, the nonlinear phase variations help to break up this structure, making these practical elements less susceptible to such correlation. Third, since these patterns are determined using the array *gain*, the effect of efficiency losses is reflected in the beamformed patterns. Consequently, as γ is increased, the loss in the ΔΣ efficiency is manifest as a scaling of the pattern (i.e. a vertical shift), thus pulling apart the ideal and ΔΣ patterns and increasing the overall error.

Fixing $\gamma = 1.1$ for the remainder of this section, we now wish to demonstrate that not only does the ΔΣ technique provide the ability to form desired patterns, but also that the dependence of quantization noise power on the density ratio is consistent with the overall development of the ΔΣ array. To begin, we compare the beamformed patterns for the ideal and quantized weights at 4, 5, and 6 GHz shown in Figures 5-8, 5-9, and 5-10, respectively. From a cursory glance at the main lobe regions, it appears that ΔΣ patterns fit most closely to the ideal patterns at 6 GHz. However, upon closer inspection, the results outside of the main lobe are more revealing. At 4 GHz, the sidelobe structure of the ΔΣ patterns tends to resemble that of the ideal patterns, with the exception of the $\theta_0 = 25°$ curve beyond about

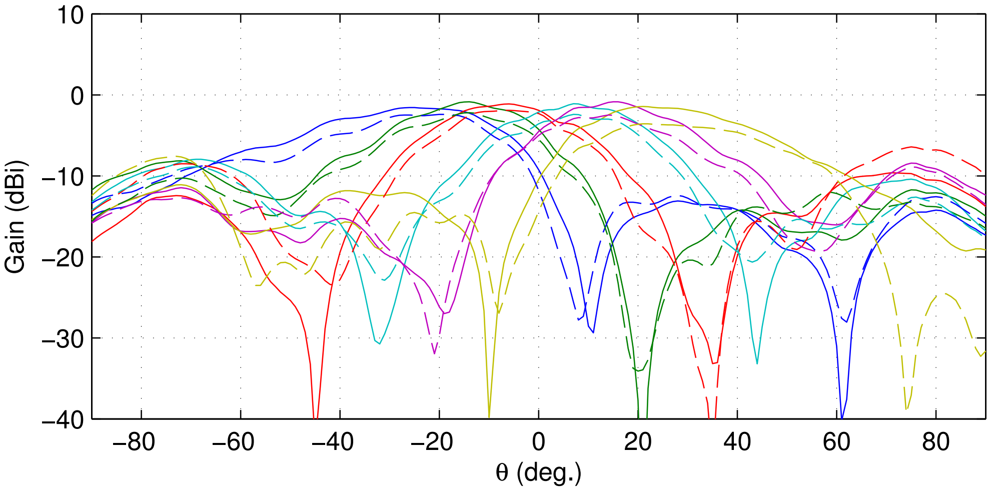

Figure 5-8: 12 x 1 array beamformed gain patterns for the ideal (solid) and $\Delta\Sigma$ (dashed) array weights at scan angles $\theta_0 = \{-25°, -15°, -5°, 5°, 15°, 25°\}$ at 4 GHz.

$\theta = 70°$. The results at 5 GHz begin to show more prominent distinctions, such as the green curve ($\theta_0 = -15°$), which shows a poor match near $\theta = 15°$ and then entirely misses the deep null near $\theta = 50°$. At 6 GHz, the errors begin to become destructive, creating "quantization lobes" at levels relative to the peak gain that are above the natural side lobes of the array pattern (e.g. the purple $\theta_0 = 15°$ curve at $\theta = -30°$ and the green $\theta_0 = -15°$ curve at $\theta = 20°$).

These observations are consistent with the intuition regarding the quantization noise as related to the electrical distance between elements. Still, it is worth revisiting the same type of analysis to explain the expected noise power as in Section 3.2.2. Recall that (3.27) was obtained from (3.26) by substituting $d_0 = Rd$ and $N_0 R = N$ at fixed frequency, making k a constant in that expression. In this case, the array geometry remains fixed such that $d = d_0 = \lambda_0/2$ and $N = N_0$, while the density variation is exhibited by $k = 2\pi/\lambda = 2\pi/\lambda_0 R$. Hence the expected noise power may be written as

$$P_{\text{noise}} = \left(\frac{\pi^2}{3N} \frac{N-1}{N} R^{-2} + \frac{1}{N^2} \right) \sigma_q^2. \tag{5.3}$$

From this form, we expect to see the average quantization noise power decrease with R^2 (plus the fixed edge element term), though two additional practical considerations will affect the behavior of these measured results. First, the finite array length results in significant element pattern variations, as we saw in Figures 5-4, 5-5 and 5-6, thus reducing the ability of the $\Delta\Sigma$ excitations to cancel the quantization errors effectively. In fact, while the element patterns at 4 GHz are somewhat less than desirable due to their high gain levels at directions well away from the array broadside, they remain relatively consistent for each element. In contrast, at 5 and 6 GHz, the variations between neighboring elements are more severe. This indicates the likely presence of additional contribution to the noise power that will also increase with frequency. Second, our results are determined from the array gain, not the normalized array patterns implicitly used in our analysis. Consequently, the inclusion

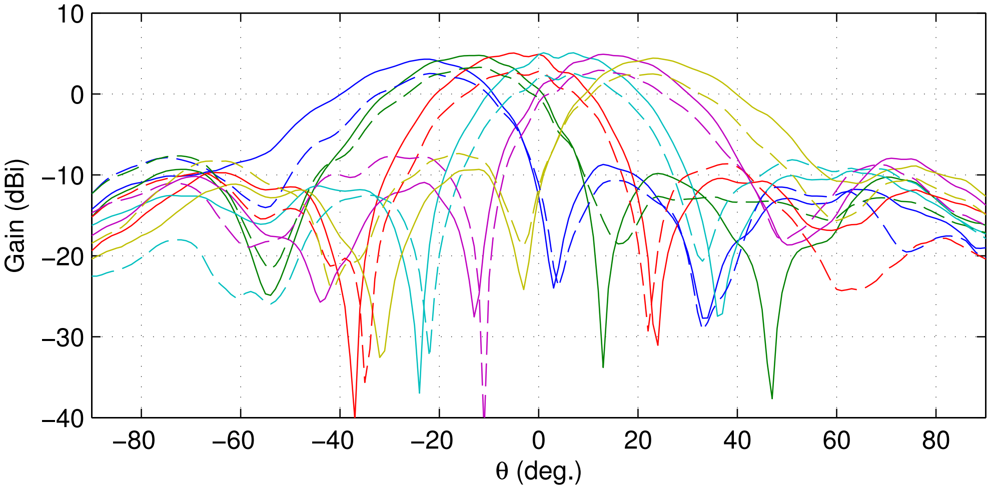

Figure 5-9: 12 x 1 array beamformed gain patterns for the ideal (solid) and ΔΣ (dashed) array weights at scan angles $\theta_0 = \{-25°, -15°, -5°, 5°, 15°, 25°\}$ at 5 GHz.

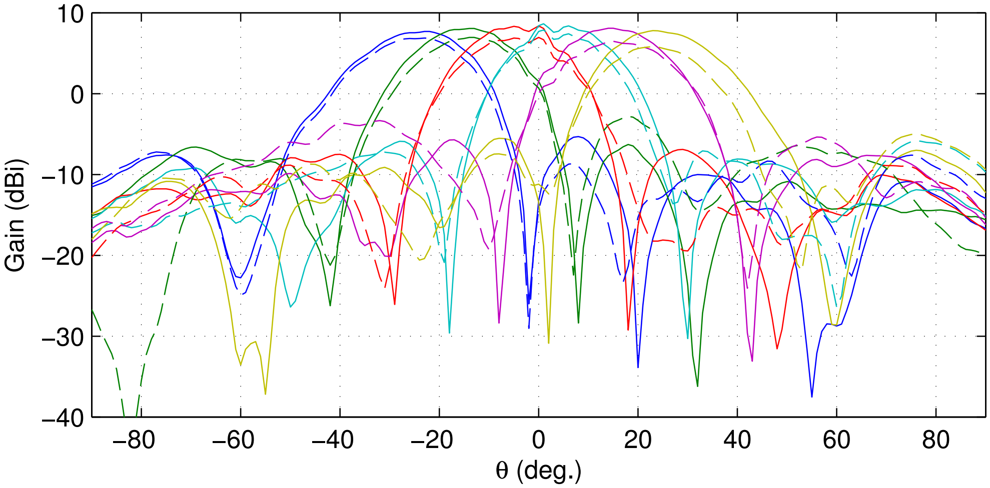

Figure 5-10: 12 x 1 array beamformed gain patterns for the ideal (solid) and ΔΣ (dashed) array weights at scan angles $\theta_0 = \{-25°, -15°, -5°, 5°, 15°, 25°\}$ at 6 GHz.

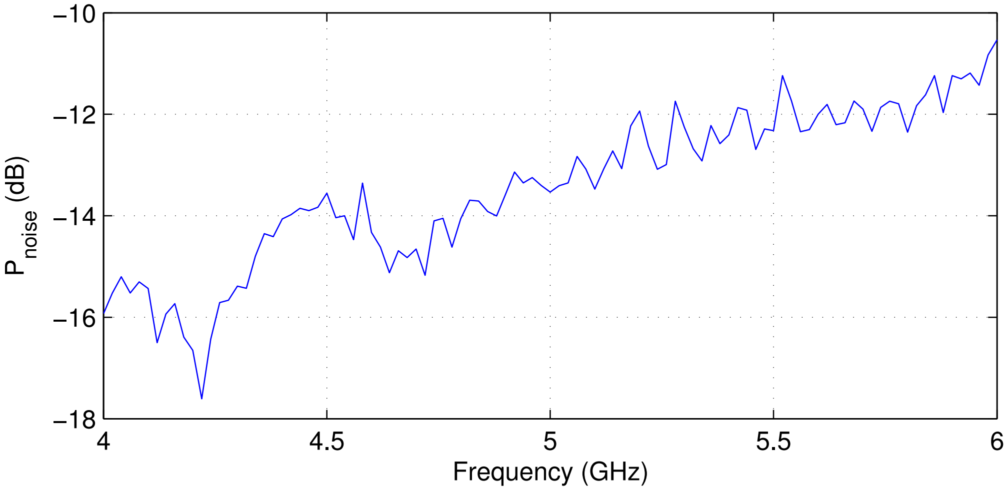

Figure 5-11: Frequency dependence of $\Delta\Sigma$ quantization noise power from measured results.

of the array efficiency will affect the results due to variations in the ideal and $\Delta\Sigma$ efficiencies relative to each other, as discussed earlier, as well as variations in the absolute efficiencies in both cases at different frequencies.

Calculating the noise power from the measured gain patterns over the 4 to 6 GHz frequency range, we obtain the results shown in 5-11. Noting that $f = f_0/R$, the expression in (5.3) indicates the result should increase with f^2. This would imply that an increase in frequency from 4 to 5 GHz should result in an increase in P_{noise} of $20\log_{10} 5/4 = 1.94$ dB and similarly an additional 1.58 dB from 5 to 6 GHz. The difference seen in the actual results are consistent with the practical considerations described above. Although the somewhat larger overall variation in the P_{noise} results could be interpreted as a more rapid reduction in the quantization noise with respect to the density ratio than the R^2 dependence suggested by (5.3), this is more likely due to the frequency dependent behavior of the element pattern variations as mentioned earlier. The role played by the array efficiencies is elucidated by Figure 5-12, which shows the average power efficiency associated with the ideal and $\Delta\Sigma$ array weights used in the calculations of P_{noise}, found by using the S-parameter measurements to form the scattering matrix in (2.8). These efficiency results explain the more anomalous behavior seen in Figure 5-11 which fall outside of the typical ripples one would expect in this practical setting. For example, at frequencies just below 6 GHz, the noise power appears to have an inflection point above which shows a more rapid increase. Observing the efficiencies at these frequencies, we see a divergence between the two curves which accounts for the additional discrepancy between the gain patterns. At the lower end of the band in the neighborhood of 4.25 GHz, the “dip” in the noise power occurs at the same point where both efficiency curves drop off, meaning the gain magnitudes and thus the associated mean square error should drop off as well. Accordingly, the behavior of the array efficiencies is clearly reflected in the noise power results.

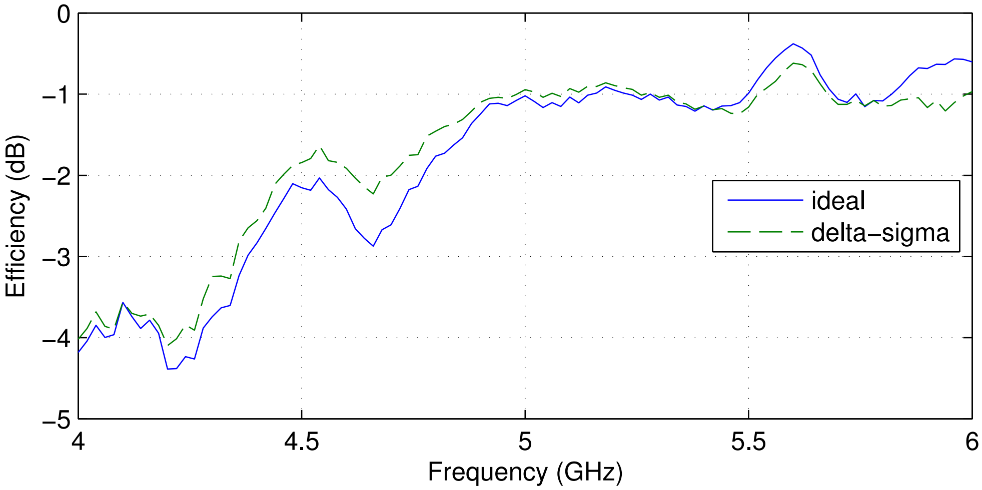

Figure 5-12: Frequency dependence of ideal and $\Delta\Sigma$ power efficiencies from measured results.

5.3 Remarks

When the practical characteristics of these measurements are accounted for, the results appear consistent with the analysis model developed for the $\Delta\Sigma$ array of isotropic elements. In fact, these additional considerations can be seen as moderate extensions of the system features that appeared in our model after the inclusion of mutual coupling. The effects of element pattern variations was seen in Section 4.1 in the form of the embedded element patterns; while from Section 4.2 it was evident that the differences in the beamformed gain patterns due to power efficiency issues – as opposed to quantization errors – was to be expected.

The available test hardware was not well suited to examine the wideband analysis in Section 4.3. In that analysis, the $\Delta\Sigma$ array was proposed as a means of obtaining wideband performance from an array of inherently narrowband elements (thin-wire dipoles), whereas in our measurements we had the very different situation of operating an ultra-wideband design outside of the intended frequency range. Not only did our results remain relatively well matched even within the measured frequency band, as was shown in Figure 5-12, but also, when simulations were run to implement the scan impedance matching network at a particular frequency, the resultant match worked well only at that frequency, thus narrowing the band of an already wideband array.

In the future, it would be of great interest to perform additional experimental measurements with array hardware specifically dedicated to the $\Delta\Sigma$ effort. This would allow for the examination of the wideband performance and would illustrate whether any assumptions, either implicit or explicit, regarding the behavior of our model and the nature of these experiments ignored any further practical considerations. Yet as they are, the present measurements provide several complementary insights to our analytical developments.

Perhaps most encouraging is the implication regarding the quantization amplitude γ. Even with the relatively modest efficiency losses predicted by the isotropic model and the compensatory wideband nature of the dense arrays, any such inherent losses remain undesirable. Based on the observation that the decrease in γ stems from the distinction between the nonlinear phase progression required to scan the main beam in this case to the linear progression used in the isotropic case, some caution should be taken in relating these experimental results to the behavior of larger designs, in which there will be a greater uniformity among the elements. Though it can be expected that practical arrays will exhibit some level of variations due to small fabrication errors, particularly in the case of high frequency millimeter wave systems, the system design should take care to consider the potential for the tone-like nature of the phase excitations. Similar issues arise in $\Delta\Sigma$ analog-to-digital converters to which he technique of adding small amounts of noise to the signal input, or *dithering*, is commonly practiced [11]. With the digital selection of the phases in the $\Delta\Sigma$ array, the implementation of some type of dithering technique could be easily implemented, allowing for the mitigation of the efficiency loss concerns.

Finally, the potential effects of element pattern variations and power efficiency seen in the measured results should be considered by the system designer when determining the density ratio appropriate for meeting a particular SQNR specification. However, the results of these experiments are not indicative of the expected performance of larger arrays, as these effects are exaggerated by the small number of elements and the operation of the array outside of its intended frequency band.

5.A Gain Measurements and Superposition

From the electromagnetic superposition principle, electric fields can be added. Our element pattern data is measured in *gain* and *phase*. We now briefly discuss how these are correctly used in beamforming.

The power pattern we have used thus far is, physically, a measure of the relative power intensity of the electromagnetic wave with electric field $E(\theta, \phi)$, where (θ, ϕ) specifies the location on a sphere of radius r in the far-field of an antenna. By restricting our attention to this sphere, attenuation due to propagation distance is constant in all directions and may be ignored. In terms of the electric field, the power intensity pattern is given by

$$P(\theta, \phi) = \frac{|E(\theta, \phi)|^2}{\xi}, \tag{5.4}$$

where ξ is the intrinsic impedance of the medium through which the wave is traveling, approximately 120π ohms in dry air.

The *directivity pattern* of an antenna is a more absolute measure of the radiating or receiving characteristics in that it is normalized by the average power intensity over the sphere (i.e. the power intensity relative to an isotropic element with the same total radiated power P_{rad})

$$D(\theta, \phi) = \frac{P(\theta, \phi)}{\frac{1}{4\pi}\int_0^{2\pi} d\phi \int_0^{\pi} d\theta \sin\theta P(\theta, \phi)} = \frac{4\pi P(\theta, \phi)}{P_{\text{rad}}}. \tag{5.5}$$

Proportional to directivity pattern is the *gain pattern*, which accounts for any power losses in the antenna

$$G(\theta, \phi) = \eta D(\theta, \phi) = \frac{P_{\text{rad}}}{P_{\text{inc}}} D(\theta, \phi), \tag{5.6}$$

where η is the antenna efficiency and P_{inc} is the total available incident power.

Combining the above expressions gives

$$G(\theta, \phi) = \frac{4\pi}{\xi} \frac{|E(\theta, \phi)|^2}{P_{\text{inc}}} \tag{5.7}$$

As such, the unit-power element pattern

$$E_n(\theta, \phi) = \sqrt{\frac{\xi}{4\pi} G_n(\theta, \phi)} e^{j\varphi_n(\theta, \phi)} \tag{5.8}$$

gives the electric field under the condition

$$w_n = 2\sqrt{Z_0}\delta_{nm}, \quad m = 0, 1, \ldots, 11 \tag{5.9}$$

such that by (2.7), $P_{\text{inc}} = 1$. Thus for any excitation,

$$E(\theta, \phi) = \frac{1}{2\sqrt{Z_0}} \sum_n w_n E_n(\theta, \phi), \tag{5.10}$$

and

$$P_{\text{inc}} = \frac{1}{4Z_0} \sum_n |w_n|^2. \tag{5.11}$$

Combining the above we arrive at the final expression for the beamformed gain

$$G(\theta, \phi) = \frac{|\sum_n w_n \sqrt{G(\theta, \phi)} e^{j\varphi_n(\theta, \phi)}|^2}{\sum_n |w_n|^2}. \tag{5.12}$$

Chapter 6

Sparse Multi-Coset Arrays

In the last few chapters, we developed the use of one type of digital-enhancement in which cooperative design of the array hardware and the associated digital control algorithms allowed for a relaxation of the requirement for high precision analog circuitry. We now turn our attention to another type of digitally-enhanced design in the form of the sparse multi-coset array.

We develop the multi-coset array from the perspective of linear imaging arrays. The concept of array imaging is quite similar to the standard notion of beamforming introduced in Chapter 2. Consider a single signal arriving at a linear array of elements at an angle θ from the axis perpendicular to the array as illustrated in Figure 6-1. For a signal with complex magnitude $X(\theta)$ at the origin, the response at position p away from the origin along the array axis is $x(p) = X(\theta)e^{-jkp\sin\theta}$. For an array of N elements at locations p_n, the "delay and sum" beamformer collimates the signal from θ by adjusting the response of each element by $e^{jkp_n\sin\theta}$ and then combining the phase-delayed responses, resulting in a beamformer output of

$$\frac{1}{N}\sum_{n=0}^{N-1} x(p_n)e^{jkp_n\sin\theta} = \frac{1}{N}\sum_{n=0}^{N-1} X(\theta)e^{-jkp_n\sin\theta}e^{jkp_n\sin\theta} = X(\theta). \tag{6.1}$$

In general, signals can arrive from any number of directions, and accordingly the beamformer phases can be varied to focus over a range of directions, building up information regarding the surrounding environment. This of course is simply the beam scanning process from Chapter 2. In the case of *digital* beamforming, each element connects directly to a receiver, which captures the response $x(p_n)$ at each element prior to beamforming, at which point scanning can be performed in the digital domain, allowing nearly instantaneous coverage over a wide range of angles.

An active radar imaging system is based on the above principles along with the addition of a transmitting source that radiates away from the array to illuminate the coverage area. When these fields interact with a *target object* at a direction θ, a certain portion of the field is scattered back to the receive array with a complex magnitude $X(\theta)$, which in this case depends on the total travel distance as well as the object size, shape, and orientation relative to the array. Hence, in radar imaging, rather than scanning the surrounding environment for incoming signals, the beamforming process captures information regarding the distribution of target objects throughout the region to form an representation, or *image*, of the particular scene.

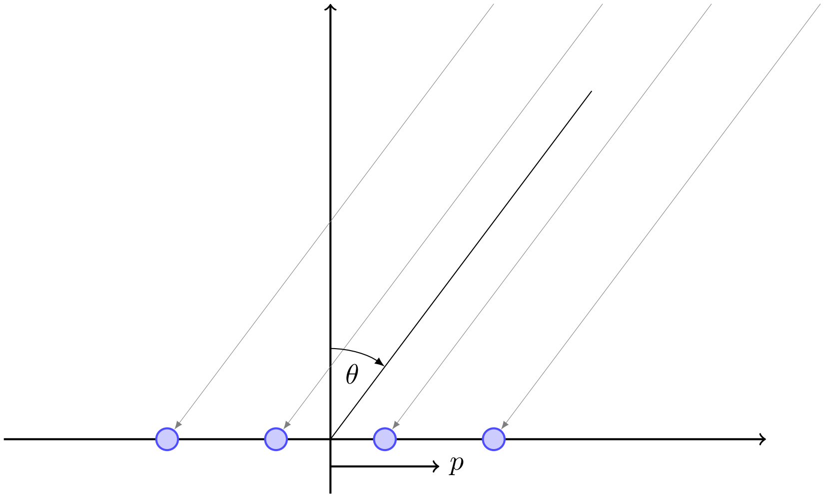

Figure 6-1: Imaging array geometry.

6.1 Array Structure and Scene Model

Throughout the development of the multi-coset array, we focus on linear arrays of elements located on some subset of collinear lattice points with uniform spacing $d = \lambda/2$, where λ is the operating wavelength of the array. We assume ideal isotropic elements and limit our attention to the half-plane such that the directional characteristics of the array are completely specified by the angle θ, measured from the broadside direction of the array.

A standard linear array refers to any array having uniform element spacing of $\lambda/2$. Substituting $\psi = \sin\theta/2$, we see the array response and far-field pattern for a standard array with $N \to \infty$ elements forming the usual Fourier transform pair

$$x[n] = \int_0^1 X(\psi) e^{j2\pi\psi n}\, \mathrm{d}\psi, \qquad n \in \mathbb{Z} \tag{6.2}$$

$$X(\psi) = \sum_{n=0}^{N-1} x[n] e^{-j2\pi\psi n}, \qquad \psi \in [0, 1). \tag{6.3}$$

From the view of array imaging, (6.2) describes $x[n]$ as the response at element n to a scene consisting of complex valued objects $X(\psi)$. Standard reconstruction (delay-and-sum beamforming) of the scene in a given direction ψ is carried out using (6.3).

The multi-coset arrays of interest in this work are subsets of a standard linear array. Specifically, for an integer parameter L, we can partition the N elements of any standard array into L cosets. Each coset is a uniform linear subarray with inter-element spacing L times greater than the nominal spacing. We index the cosets by the position of their first element relative to the first element of the full array. A *multi-coset* array comprises a subset of these cosets. In particular, for $P \leq L$, a (P, L) multi-coset array is an array formed by including P of these cosets. The selected cosets are denoted via

$$\mathcal{P} = \{p_0, p_1, \ldots, p_{P-1}\}, \tag{6.4}$$

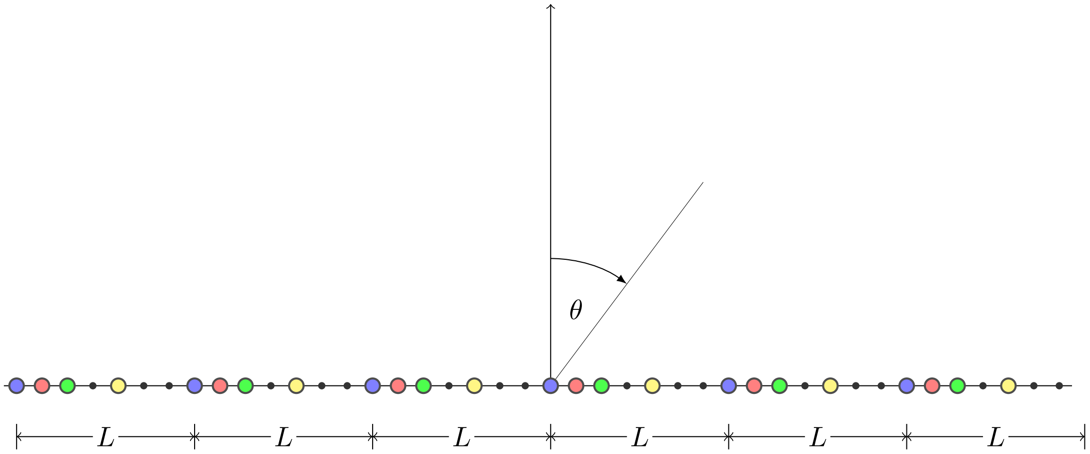

Figure 6-2: $(P, L) = (4, 7)$ multi-coset array with coset pattern $\mathcal{P} = \{0, 1, 2, 4\}$ and $M = 6$ coset periods.

with $0 \leq p_0 < p_1 < \cdots < p_{P-1} \leq L-1$, and is referred to as the *coset pattern* of the array. Note that the resulting array has a recurrent uniform pattern with period L, and thus we refer to L as the *coset period*. As further notation, there are $M = N/L$ such periods in the array. As an example, Figure 6-2 depicts the layout of a $(4, 7)$ multi-coset array with coset pattern $\mathcal{P} = \{0, 1, 2, 4\}$ superimposed on the lattice of the associated standard linear array from which it was derived. The colors of the elements indicate the different cosets that comprise the recurrent structure of the array. For example, the green elements make up the coset indexed by $p_2 = 2$ and the yellow elements represent the coset indexed by $p_3 = 4$.

The response for coset p is defined via

$$x^{(p)}[n] \triangleq x[n] \sum_{m=0}^{M-1} \delta[n - (mL + p)], \quad p \in \{0, 1, \ldots, L-1\}, \tag{6.5}$$

for $n = 0, 1, \ldots,$ where

$$\delta[k] \triangleq \begin{cases} 1 & k = 0 \\ 0 & \text{otherwise.} \end{cases} \tag{6.6}$$

The corresponding coset image in the angular domain is given by the Fourier transform of the coset response, i.e.,

$$X^{(p)}(\psi) = \sum_{n} x^{(p)}[n]\, e^{-j2\pi\psi n}, \qquad \psi \in [0, 1). \tag{6.7}$$

The individual coset images in (6.7) contain L uniformly shifted copies of the original scene due to the aliasing effect caused by the increased element spacing Ld. As a result, the coset image appears as L sectors, each containing grating lobes from the other $L-1$ sectors in addition to the correct response. Combining (6.2), (6.5), and (6.7), the coset image in the first sector can be written as a linear combination of the grating lobes of the original

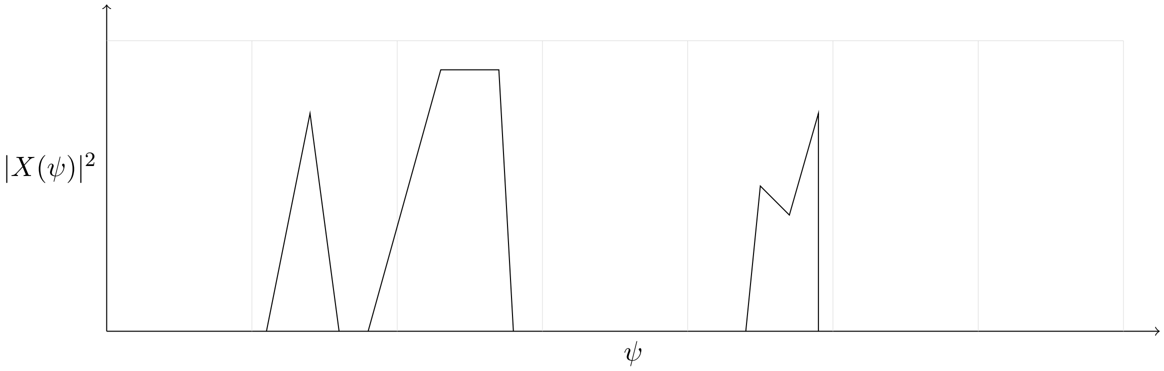

Figure 6-3: $(Q, L) = (3, 7)$-sparse scene with support $\mathcal{Q} = \{1, 2, 4\}$

scene

$$X^{(p)}(\psi) = \frac{1}{L} \sum_{q=0}^{L-1} X(\psi + q/L)\, e^{j2\pi pq/L}, \quad \psi \in [0, 1/L). \tag{6.8}$$

The goal in multi-coset image reconstruction is to extract the entire correct image from the images of multiple cosets in a single sector. While this is in general not possible, it is in scenarios where there are imaging targets in only a subset of the L sectors in the original scene, which we refer to as *sector sparsity.* More specifically, for any pair of integers $Q \leq L$, we say that a scene is (Q, L)-sparse if $X(\psi) = 0$ for all $\psi \notin \mathcal{S}$, where

$$\mathcal{S} = \bigcup_{k=0}^{Q-1} \left[\frac{q_k}{L}, \frac{q_k + 1}{L} \right), \tag{6.9}$$

where the q_k are integer-valued elements satisfying $0 \leq q_0 < q_1 < \cdots < q_{Q-1} \leq L - 1$. The set

$$\mathcal{Q} = \{q_0, q_1, \ldots, q_{Q-1}\}, \tag{6.10}$$

is referred to as the *(sector) support* of the scene. An example illustration of a $(3, 7)$-sparse scene is shown in Figure 6-3.

The array structure and scene model above is the spatial counterpart of temporal framework originally introduced [35], which developed the use of multi-coset sampling for signals with sparse spectral support.

In the following section, we summarize when and how image reconstruction is possible with multi-coset arrays for sector sparse scenes.

6.2 Multi-Coset Imaging Principles

In this section, we summarize the basic principles underlying multi-coset imaging of sector sparse scenes, and introduce our notation for the remainder of our analysis. Subsequent sections will then build on this foundation, incorporating the effects of noise and developing robust system design.

In our architecture, imaging proceeds in two phases: the first phase recovers the sector support of the scene, while the second phase reconstructs the signal values (target amplitudes and directions) in the active sectors identified in the first phase.

6.2.1 Reconstruction with known support

We begin by developing the properties of scene reconstruction when the sector support is known, corresponding to the second phase of the imaging process. This reconstruction can be expressed as the solution to a set of (possibly) redundant linear equations.

To see this, we first define

$$Y_p(\psi) \triangleq X^{(p)}(\psi)\, H(\psi), \tag{6.11}$$

$$X_q(\psi) \triangleq X(\psi + q/L)\, H(\psi), \tag{6.12}$$

with

$$H(\psi) \triangleq \begin{cases} 1 & \psi \in [0, 1/L) \\ 0 & \text{otherwise,} \end{cases} \tag{6.13}$$

from which we can express (6.8) in the form

$$Y_p(\psi) = \sum_{q=0}^{L-1} F_{pq} X_q(\psi) \quad \text{with} \quad F_{pq} \triangleq \frac{1}{L} e^{j2\pi pq/L}, \tag{6.14}$$

or, equivalently, $\mathbf{Y}(\psi) = \mathbf{F}\mathbf{X}(\psi)$, where $[\mathbf{Y}(\psi)]_p = Y_p(\psi)$, $[\mathbf{X}(\psi)]_q = X_q(\psi)$, and $[\mathbf{F}]_{pq} = F_{pq}$.

From (6.14) we see that the $\{X_q(\psi)\}$ may be directly recovered from the complete set of coset responses $\{Y_p(\psi)\}$. And once these quantities are recovered, image reconstruction is completed via

$$X(\psi) = \sum_{q=0}^{L-1} X_q(\psi - q/L). \tag{6.15}$$

In the case of a (P, L) sparse multi-coset array, we must consider instead the length-P vector $\mathbf{Y}_{\mathcal{P}}(\psi)$, composed of the entries of $\mathbf{Y}(\psi)$ indexed by the coset pattern $\mathcal{P}$. Similarly, we define the $P \times L$ matrix $\mathbf{F}_{\mathcal{P}}$ containing the P rows of $\mathbf{F}$ indexed by $\mathcal{P}$. This results in the relation

$$\mathbf{Y}_{\mathcal{P}}(\psi) = \mathbf{F}_{\mathcal{P}}\mathbf{X}(\psi). \tag{6.16}$$

In this form, we now have an undetermined system, having an infinite number of possible solutions.

For a (Q, L)-sparse scene with support $\mathcal{Q}$, the elements of $\mathbf{X}(\psi)$ not indexed by this support are zero-valued, and thus do not contribute to the coset responses. Hence, we may define the $P \times Q$ *measurement matrix* $\mathbf{F}_{\mathcal{P}\mathcal{Q}}$, composed of the columns of $\mathbf{F}_{\mathcal{P}}$ indexed by $\mathcal{Q}$, and the length-Q vector $\mathbf{X}_{\mathcal{Q}}(\psi)$ containing the nonzero entries of $\mathbf{X}(\psi)$. The updated relation becomes

$$\mathbf{Y}_{\mathcal{P}}(\psi) = \mathbf{F}_{\mathcal{P}\mathcal{Q}}\mathbf{X}_{\mathcal{Q}}(\psi). \tag{6.17}$$

If $\mathbf{F}_{\mathcal{P}\mathcal{Q}}$ is full rank, the correct image may be reconstructed as

$$\hat{\mathbf{X}}_{\mathcal{Q}}(\psi) = \mathbf{F}^{+}_{\mathcal{P}\mathcal{Q}}\mathbf{Y}_{\mathcal{P}}(\psi), \tag{6.18}$$

where $\mathbf{F}^{+}_{\mathcal{P}\mathcal{Q}} = (\mathbf{F}^{\dagger}_{\mathcal{P}\mathcal{Q}}\mathbf{F}_{\mathcal{P}\mathcal{Q}})^{-1}\mathbf{F}^{\dagger}_{\mathcal{P}\mathcal{Q}}$ is the Moore-Penrose pseudo-inverse of the matrix $\mathbf{F}_{\mathcal{P}\mathcal{Q}}$,

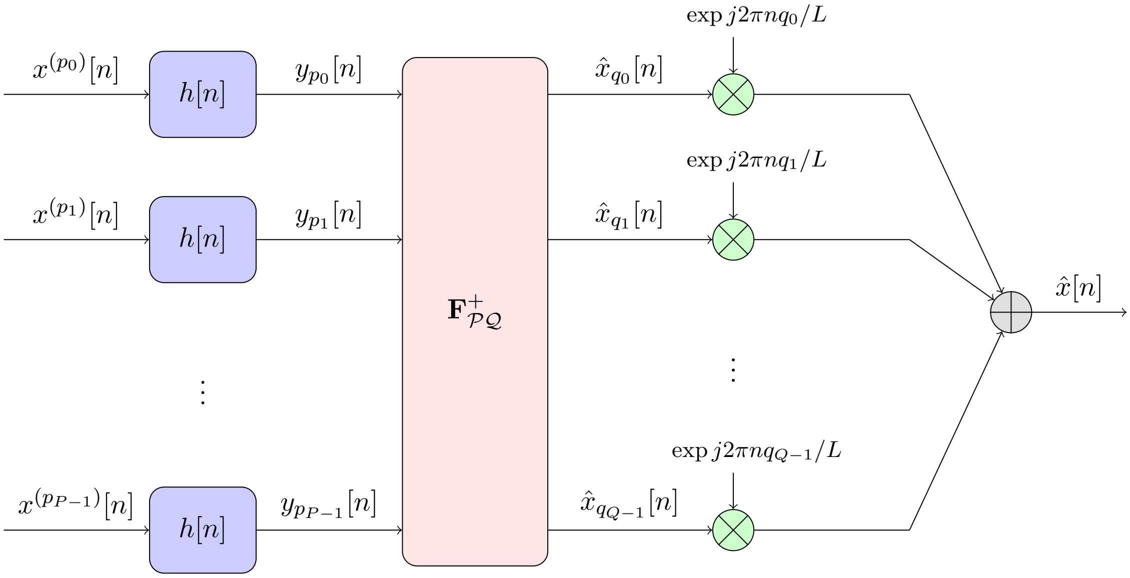

Figure 6-4: Multi-coset reconstruction processing chain.

with † denoting the conjugate transpose operator [44].

In practice, it is straightforward to ensure that the reconstruction (6.18) exists. In particular, the rank of $\mathbf{F}_{\mathcal{PQ}}$ depends on both $\mathcal{P}$ and $\mathcal{Q}$. A pattern $\mathcal{P}$ that ensures $\mathbf{F}_{\mathcal{PQ}}$ is full rank for any support of length Q is called a universal pattern. As shown in [35], such patterns exist whenever $P \geq Q$. For example, the so-called "bunched" pattern, in which the first P cosets are selected, i.e., $p_i = i, \quad i = 0, 1, \ldots, P-1$, is generally universal, though we will ultimately be interested in still better patterns.

System Implementation

The basic architecture described in this section admits a convenient implementation. In particular, the required processing is straightforward to carry out on the coset responses $x^{(p)}[n]$ directly in the array domain, and takes the form depicted in Figure 6-4.

As the first step, corresponding to (6.11), the coset responses are first passed through a linear time-invariant filter with unit-sample response $h[n]$ (whose Fourier transform is $H(\psi)$), to form the entries of the output vector sequence $\mathbf{y}_{\mathcal{P}}[n]$. From this array domain perspective, we see that the entries of $\mathbf{y}_{\mathcal{P}}[n]$ are the interpolated coset responses, generating $L-1$ values between each coset element via the interpolating filter $h[n]$.

As the second step, corresponding to expressing (6.17) in the following array domain form

$$\mathbf{y}_{\mathcal{P}}[n] = \mathbf{F}_{\mathcal{PQ}}\,\mathbf{x}_{\mathcal{Q}}[n], \tag{6.19}$$

we generate the reconstruction $\hat{\mathbf{x}}_{\mathcal{Q}}[n] = \mathbf{F}^+_{\mathcal{PQ}}\mathbf{y}_{\mathcal{P}}[n]$. by applying the $Q \times P$ matrix $\mathbf{F}^+_{\mathcal{PQ}}$ to obtain the $\hat{\mathbf{x}}_{\mathcal{Q}}[n]$.

As the final step, corresponding to the following array domain version of (6.15)

$$x[n] = \sum_{q=0}^{L-1} x_q[n]\, e^{j2\pi nq/L}, \tag{6.20}$$

we have that the complete array response $\hat{x}[n]$ may be formed in the array domain by modulating and summing the Q contributions from $\hat{\mathbf{x}}_{\mathcal{Q}}[n]$.

6.2.2 Support recovery

We next consider the first phase of imaging, corresponding to determining the active sectors in the scene, i.e., the sectors containing nonzero signal content. In this phase, Q is treated as known, and we seek to recover $\mathcal{Q}$.

Since if $q \notin \mathcal{Q}$, then $X_q(\psi) = 0$ for all $\psi \in [0, 1/L)$, the recovery of $\mathcal{Q}$ via (6.16) can be viewed as an infinite-dimensional version of what is known in the compressive sensing literature as a *multiple measurement vector* (MMV) problem. However, it is straightforward to reduce the problem to a finite-dimensional one through a representation in terms of correlation matrices. In particular, with

$$\mathbf{R}_{\mathbf{X}} = \int_0^{1/L} \mathbf{X}(\psi)\mathbf{X}^\dagger(\psi)\,\mathrm{d}\psi \in \mathbb{C}^{L\times L}, \tag{6.21}$$

$$\mathbf{R}_{\mathbf{Y}_{\mathcal{P}}} = \int_0^{1/L} \mathbf{Y}_{\mathcal{P}}(\psi)\mathbf{Y}_{\mathcal{P}}^\dagger(\psi)\,\mathrm{d}\psi \in \mathbb{C}^{P\times P} \tag{6.22}$$

denoting the coset correlation matrices, respectively, we have the relation

$$\mathbf{R}_{\mathbf{Y}_{\mathcal{P}}} = \mathbf{F}_{\mathcal{P}}\mathbf{R}_{\mathbf{X}}\mathbf{F}_{\mathcal{P}}^\dagger. \tag{6.23}$$

We may decompose the coset correlation matrix according to $\mathbf{R}_{\mathbf{Y}_{\mathcal{P}}} = \mathbf{V}\mathbf{V}^\dagger$ with $\mathbf{V} = \mathbf{U}\boldsymbol{\Lambda}^{1/2}$, where $\mathbf{U}$ and $\boldsymbol{\Lambda}$ are obtained from the eigenvalue decomposition $\mathbf{R}_{\mathbf{Y}_{\mathcal{P}}} = \mathbf{U}\boldsymbol{\Lambda}\mathbf{U}^\dagger$. In turn, we can write

$$\mathbf{V} = \mathbf{F}_{\mathcal{P}}\mathbf{W}, \tag{6.24}$$

where, via (6.23), $\mathbf{R}_{\mathbf{X}} = \mathbf{W}\mathbf{W}^\dagger$. Thus, we seek to determine a suitable $\mathbf{W}$ from $\mathbf{V}$.

Since $\mathbf{F}_{\mathcal{P}}$ is a $P \times L$ matrix with $P \leq L$, the matrix $\mathbf{W}$ is not uniquely determined by (6.24). The compressive sensing problem seeks the solution $\mathbf{W}_0$ that minimizes the number of rows having nonzero entries. This particular ℓ_0-minimization problem may be replaced by a computationally preferable (specifically, convex) ℓ_1-minimization problem. To this end, we define the length-L vector $\mathbf{w}$ with entries equal to the ℓ_2-norm of the corresponding rows of $\mathbf{W}$. With this, the optimization becomes

$$\text{minimize } \|\mathbf{w}\|_1 \quad \text{subject to } \mathbf{V} - \mathbf{F}_{\mathcal{P}}\mathbf{W} = \mathbf{0}. \tag{6.25}$$

For a more detailed discussion of this formulation, and additional perspectives, see, e.g., [45]. More generally, there is a broader literature on algorithms for the solution of MMV problems; see, e.g., [46, 47].

Of particular interest to the design of the multi-coset array is an understanding of the number of cosets P required to guarantee the recovery of Q support sectors. From [46], a sufficient condition for unique recovery is given by

$$P \geq 2Q - \operatorname{rank}(\mathbf{R}_{\mathbf{X}}) + 1. \tag{6.26}$$

This result tells us that the required number of cosets depends not only on the number of occupied sectors, but also upon the cross-correlation of the scene content among the different sectors (for example, due to multi-path).

Eq. (6.26) implies that in the worst-case ($\text{rank}(\mathbf{R_X}) = 1$) we may require $P \geq 2Q$ cosets, as compared with $P \geq Q$ when the sector support is known, as discussed in Section 6.2.1. Hence, blindness can incur a factor of two increase in the minimum number of array elements required for successful image reconstruction. However, when the rows of $\mathbf{X}(\psi)$ form a linearly independent set, $\mathbf{R_X}$ has rank Q and it follows from (6.26) that $P \geq Q + 1$ cosets are sufficient for recovery. In this case, the price of blindness is the requirement of a single additional coset.

Solutions to the ℓ_1-minimization problem may still require more computation than may be practical in a dynamic imaging application. For such scenarios, a computationally less expensive solution is the alternative originally proposed in [35] and based on the MUSIC direction finding algorithm [25]. The basic algorithm is as follows. In the absence of noise, the correlation matrix $\mathbf{R}_{\mathbf{Y}_\mathcal{P}}$ has Q of its P eigenvalues nonzero. Accordingly, the eigenvector matrix is partitioned as $\mathbf{U} = [\mathbf{U}_\text{S}\, \mathbf{U}_\text{N}]$, where the $P \times Q$ matrix $\mathbf{U}_\text{S}$ contains the eigenvectors corresponding to the nonzero eigenvalues. These eigenvectors form an orthonormal basis for the range of the measurement matrix $\mathbf{F}_{\mathcal{P}\mathcal{Q}}$, traditioanlly referred to as the *signal subspace*. The orthogonal subspace spanned by the columns of the $P \times (P - Q)$ matrix $\mathbf{U}_\text{N}$ is known as the *noise subspace*. In this scenario, the zero-valued eigenvalues associated with this subspace reflect the noise-free idealization. To determine the support, each of the L columns of $\mathbf{F}_\mathcal{P}$ is projected onto the noise subspace. The columns corresponding to the active sectors contained within the support $\mathcal{Q}$ lie in the orthogonal subspace spanned by $\mathbf{U}_\text{S}$ and hence will have zero projection onto $\mathbf{U}_\text{N}$. The recovered support $\hat{\mathcal{Q}}$ contains the indices of these columns. Thus, defining the columns of $\mathbf{F}_\mathcal{P}$ and $\mathbf{U}$ as $\mathbf{f}_q$ and $\mathbf{u}_m$ such that $\mathbf{F}_\mathcal{P} = [\mathbf{f}_0\, \mathbf{f}_1\, \cdots\, \mathbf{f}_{L-1}]$ and $\mathbf{U} = [\mathbf{u}_0\, \mathbf{u}_1\, \cdots\, \mathbf{u}_{P-1}]$ (where the $\mathbf{u}_m$ are ordered by eigenvalue size), the algorithm evaluates the *null spectrum*

$$D_\text{MUSIC}(q) = \sum_{m=Q}^{P-1} |\mathbf{f}_q^\dagger \mathbf{u}_m|^2 \tag{6.27}$$

and selects as $\mathcal{Q}$ the values of q such that $D_\text{MUSIC}(q) = 0$.

For the case in which $\text{rank}(\mathbf{R_X}) = Q$, the MUSIC approach is particularly attractive, being a polynomial-time algorithm satisfying the lower bound of (6.26) [35]. However, it is well-known that the MUSIC algorithm is unreliable in scenarios corresponding to the case in which $\mathbf{R_X}$ is rank-deficient [25]. For such cases, a hybrid MMV algorithm referred to as subspace-augmented MUSIC, which combines MUSIC with orthogonal matching pursuit techniques, may be be used to more efficiently handle rank-deficiencies [48].

More generally, additional results on the relationship between traditional CS MMV algorithms, MUSIC, and the issue of rank may be found in, e.g., [49, 50].

System Implementation

While not shown in Figure 6-4, the sector support $\hat{\mathcal{Q}}$ is recovered from $\mathbf{y}_\mathcal{P}[n]$ prior to the remaining steps of the reconstruction. For this recovery procedure, the required correlation matrix $\mathbf{R}_{\mathbf{y}_\mathcal{P}}$ can also be computed from the coset responses directly in the array domain according to [cf. (6.22)]

$$[\mathbf{R}_{\mathbf{y}_\mathcal{P}}]_{lk} = \sum_n y_{p_l}[n]\, y_{p_k}^*[n]. \tag{6.28}$$

The estimated support is then utilized in the remaining reconstruction steps.

6.2.3 Coset period selection considerations

For a fixed aperture length corresponding to a standard array of N elements, the choice of the coset period L in the associated multi-coset array involves a tradeoff between conflicting objectives.

On one hand, the sector-wise density $\rho_{s,L} = Q/L$ of the scene decreases monotonically with increasing L, converging to the limiting scene density ρ_s. Hence, this favors choosing a large value for L, so that the sparsest possible array can be used.

On the other hand, as L increases, the number of coset periods $M = N/L$ decreases, causing imaging performance to suffer. This is due mainly to two reasons. First, the number of coset periods can be viewed as corresponding to the number of "snapshots" involved in estimating the scene support, and fewer snapshots means less noise averaging. Second, with a finite array aperture, targets in active sectors $\mathcal{Q}$ effectively "spill over" into neighboring inactive sectors, so that underlying sparsity corresponding to (6.9) is obscured. Moreover, this leakage is exacerbated as the sectors become narrower.

As will be discussed shortly, the support recovery and scene reconstruction algorithms can be made robust to the situation in which (6.9) is violated by the presence of noise in the inactive sectors. Moreover, from the perspective of the associated processing, the signal energy leaked into inactive sectors behaves like other sources of noise in the system. Hence, its dominant effect is to increase the noise floor in the measurements, and its impact can be neglected provided its level is significantly lower than that due to the combination of other sources of noise in the system. In practice, we can usually choose L small enough to ensure this.

More generally, the use of standard low-sidelobe tapers from the array processing literature will mitigate the spillover effect and help to make possible the use of larger values of L and thus sparser array designs at high SNRs. And for scenarios where leakage simply cannot be ignored, a refined version of the array-domain image reconstruction process is described in [26]. Using this aperture-aware reconstruction, it is shown that the finite-aperture effects may be reduced to any desired level by dedicating a suitable portion of the array to the task, which in turn incurs a corresponding reduction in resolution.

6.3 Multi-Coset Array Processing

Having summarized the basic principles and techniques governing multi-coset imaging we now turn to the detailed design of robust multi-coset array processing. Central to our development is quantifying the impact of noise on the performance of the imaging system, and identify how to best mitigate the impact of such noise. Since noise affects both support recovery and scene reconstruction phases of the imaging process, we consider each separately, starting with the latter.

6.3.1 Reconstruction noise amplification

With respect to scene reconstruction, the second phase of the imaging process, noise causes a direct degradation in the reconstruction SNR (RSNR). We will characterize the relationship between the SNR at the sensor and the resulting RSNR. Since the SNR at the sensor is the reconstruction SNR for a standard array, this relationship allows us to assess the impact of the multi-coset architecture. We focus on the high SNR regime, where we can assume the support is reliably recovered.

We begin by showing how the RSNR is related to the condition number of the relevant measurement matrix $\kappa(\mathbf{F}_{\mathcal{PQ}})$. First, let $x[n]$ denote the array response from the scene as before, but now we let $z[n]$ denote the spatially-white array response due to the noise. Defining $\mathbf{Z}(\psi) \in \mathbb{C}^L$ such that $[\mathbf{Z}(\psi)]_q = Z(\psi + q/L)$ is the coset response in the image domain is, we then have

$$\begin{aligned} \mathbf{Y}_{\mathcal{P}}(\psi) &= \mathbf{F}_{\mathcal{P}}(\mathbf{X}(\psi) + \mathbf{Z}(\psi)) \\ &= \mathbf{F}_{\mathcal{PQ}}\mathbf{X}_{\mathcal{Q}}(\psi) + \mathbf{F}_{\mathcal{P}}\mathbf{Z}(\psi). \end{aligned} \tag{6.29}$$

Applying our scene reconstruction procedure (which ignores the noise), we obtain that the resulting noisy reconstruction is

$$\begin{aligned} \hat{\mathbf{X}}_{\mathcal{Q}}(\psi) &= \mathbf{F}^{+}_{\mathcal{PQ}}\mathbf{Y}_{\mathcal{P}}(\psi) \\ &= \mathbf{X}_{\mathcal{Q}}(\psi) + \mathbf{F}^{+}_{\mathcal{PQ}}\mathbf{F}_{\mathcal{P}}\mathbf{Z}(\psi), \end{aligned} \tag{6.30}$$

which corresponds to the desired image plus an amplified noise component.

The reference noise level is

$$N_0 \triangleq \mathbb{E}\left[\int_0^1 |Z(\psi)|^2 \, \mathrm{d}\psi\right], \tag{6.31}$$

which corresponds to the reconstruction noise level in a standard array. For the multi-coset array, the reconstruction noise level is, via (6.30),

$$\begin{aligned} N_r &= \mathbb{E}\left[\int_0^1 \|\mathbf{F}^{+}_{\mathcal{PQ}}\mathbf{F}_{\mathcal{P}}\mathbf{Z}(\psi)\|^2 \, \mathrm{d}\psi\right] && (6.32) \\ &= \mathrm{Tr}\left((\mathbf{F}^{+}_{\mathcal{PQ}}\mathbf{F}_{\mathcal{P}})\, \mathbb{E}\left[\mathbf{R}_Z\right] (\mathbf{F}^{+}_{\mathcal{PQ}}\mathbf{F}_{\mathcal{P}})^{\dagger}\right) && (6.33) \\ &= \mathrm{Tr}\left(\mathbf{F}^{+}_{\mathcal{PQ}}\mathbf{F}_{\mathcal{P}}\mathbf{F}^{\dagger}_{\mathcal{P}}\mathbf{F}^{+,\dagger}_{\mathcal{PQ}}\right) \frac{N_0}{L}, && (6.34) \\ &= \mathrm{Tr}\left(\mathbf{F}^{+}_{\mathcal{PQ}}\mathbf{F}^{+,\dagger}_{\mathcal{PQ}}\right) \frac{N_0}{L^2} && (6.35) \end{aligned}$$

where to obtain (6.34) we have use the spatial whiteness of $z[n]$, and to obtain (6.35) we have used that the rows of $\mathbf{F}_{\mathcal{P}}$ are taken from the $L \times L$ (inverse) DFT matrix, whence $\mathbf{F}_{\mathcal{P}}\mathbf{F}^{\dagger}_{\mathcal{P}} = \mathbf{I}/L$ with $\mathbf{I}$ denoting the identity matrix.

Comparing (6.31) with (6.35), and recognizing that

$$\|\mathbf{A}\|^2_{\mathrm{F}} \triangleq \mathrm{Tr}(\mathbf{A}\mathbf{A}^{\dagger}) \tag{6.36}$$

is the squared Frobenius norm of an arbitrary matrix $\mathbf{A}$, we see that RSNR in the multi-coset imaging system is reduced by a factor

$$\begin{aligned}\frac{N_r}{N_0} &= \frac{\|\mathbf{F}^{+}_{\mathcal{PQ}}\|^2_{\mathrm{F}}}{L^2} \\ &= \frac{1}{L^2}\sum_{j=0}^{P-1}\sum_{i=0}^{Q-1}\left|\left[\mathbf{F}^{+}_{\mathcal{PQ}}\right]_{ij}\right|^2 \\ &= \frac{1}{L^2}\sum_{i=0}^{Q-1}\left|\sigma_i(\mathbf{F}^{+}_{\mathcal{PQ}})\right|^2 \\ &= \frac{1}{L^2}\sum_{i=0}^{Q-1}\frac{1}{|\sigma_i(\mathbf{F}_{\mathcal{PQ}})|^2} \qquad (6.37)\end{aligned}$$

where the $\{\sigma_i(\mathbf{F}^{+}_{\mathcal{PQ}})\}$ are the Q nonzero singular values of $\mathbf{F}^{+}_{\mathcal{PQ}}$, and where to obtain (6.37) we have used that the singular values of a matrix are the reciprocals of the singular values of its pseudo-inverse.

In the high SNR regime, the condition number of the measurement matrix, $\kappa(\mathbf{F}_{\mathcal{PQ}})$, which is the ratio its maximum to minimum singular values, accurately reflects the degree of noise amplification in the reconstruction. To see this, note that since $\mathbf{F}_{\mathcal{PQ}}$ is a $P \times Q$ matrix with each entry having magnitude $1/L$, it follows that

$$\|\mathbf{F}_{\mathcal{PQ}}\|^2_{\mathrm{F}} = \sum_{i=0}^{Q-1}|\sigma_i(\mathbf{F}_{\mathcal{PQ}})|^2 = \frac{PQ}{L^2}. \qquad (6.38)$$

Thus, while the sum in (6.38) is fixed for a given L, P, and Q, the sum in (6.37) may vary greatly, depending on the distribution of the singular values of the measurement matrix. Specifically, the smaller the minimum $\sigma_i(\mathbf{F}_{\mathcal{PQ}})$, the larger the noise amplification. Hence, in the selection of the coset pattern, it is desirable to select $\mathcal{P}$ such that $\kappa(\mathbf{F}_{\mathcal{PQ}})$ takes relatively small values for *all* support sets $\mathcal{Q}$.

6.3.2 Support recovery reliability

With respect to support recovery, the first phase of the imaging process, the presence of noise means that (6.9) does not strictly holds for any $Q < L$, and thus there is no exact sparse solution to (6.16). As a result, modifications to the support recovery algorithm are required. Ultimately, we will characterize the performance of the support recovery phase in terms of the threshold SNR (TSNR) above which the correct support $\mathcal{Q}$ can be reliably recovered, and note that this threshold will in general depend on the scene density and choice of coset pattern $\mathcal{P}$.

Before characterizing the support recovery performance, we first develop how to accommodate noise in the both the ℓ_1-minimization and MUSIC-based approaches to the problem.

With respect to the ℓ_1-minimization approach, we note that the optimization (6.25) must modified. In particular, following standard practice, since the noise precludes the possibility of an exact sparse solution, we relax the equality constraint in (6.25), yielding

$$\text{minimize } \|\mathbf{w}\|_1 \quad \text{subject to } \|\mathbf{V} - \mathbf{F}_{\mathcal{P}}\mathbf{W}\|^2_{\mathrm{F}} < \epsilon, \qquad (6.39)$$

where ϵ is chosen as a function of the SNR. A variety of algorithms suited to this noisy MMV problem can be found in [51, 52].

For the MUSIC algorithm approach, the extension to the noisy case is straightforward when the number of measurements is large enough such that the eigenvector matrix $\mathbf{U}$ has converged to roughly the noise free case, and the noise power is uniformly distributed throughout both the signal and noise subspaces [25]. However, difficulties arise when the number of coset periods is more limited. In particular, $\mathbf{U}_\mathrm{S}$ and $\mathbf{U}_\mathrm{N}$ will not accurately partition the signal and noise subspaces, and the contribution due to noise is no longer evenly distributed over the P eigenvalues.

A "soft" version of the MUSIC algorithm known as the eigenvalue method [53] accounts for finite sample sets by weighing the projections onto each subspace direction $\mathbf{u}_m$ more heavily for smaller eigenvalues. Specifically, the null-spectrum under this method is given by

$$D_\mathrm{EV}(q) = \sum_{m=Q}^{P-1} \frac{1}{\lambda_m} |\mathbf{f}_q^\dagger \mathbf{u}_m|^2, \tag{6.40}$$

where the eigenvalues λ_m are the (ordered) diagonal elements of $\mathbf{\Lambda}$. In essence, this approach aims to suppress the signal contribution within the estimate of $\mathbf{U}_\mathrm{N}$ in order to obtain a more accurate representation of the true noise subspace.

At low SNR, as the threshold between signal and noise eigenvalues becomes less distinct, the estimated signal eigenvectors can potentially be aligned more closely to the true noise subspace than the true signal subspace. This point is unaccounted for in (6.40). Based on this observation, we have found that a still "softer" version of MUSIC, corresponding to the null-spectrum

$$D_\mathrm{MEV}(q) = \sum_{m=0}^{P-1} \left(\frac{1}{\lambda_m^{1/2}} - \frac{1}{\lambda_0^{1/2}} \right)^2 |\mathbf{f}_q^\dagger \mathbf{u}_m|^2, \tag{6.41}$$

to be effective at low SNR—a regime in which MUSIC has traditionally been considered unsuitable. We stress that this version of MUSIC includes contributions from the *entire* column space of $\mathbf{U}$, save for the eigenvector associated with the largest eigenvalue λ_0.

Numerical simulations were performed to compare the different recovery algorithms. A representative example of the results is shown in Figure 6-5. In these simulations, a coset period of $L = 19$ with $P = 9$ active cosets was selected. The coset pattern is fixed at $\mathcal{P} = \{0, 1, 2, 3, 5, 7, 12, 13, 16\}$, selected by the design algorithm described in the following section. To gauge the recovery performance of the basic MUSIC, eigenvalue-MUSIC (soft MUSIC), modified-eigenvalue-MUSIC (softer MUSIC), and ℓ_1-minimization algorithms, each was applied to 1000 randomly generated scenes in which $Q = 7$ active sectors supported by $\mathcal{Q}$ were selected at random. Gaussian noise was added to each scene, evenly distributed over the entire range of ψ. This was repeated over a range of SNRs. A successful recovery was declared when the Q most likely active sectors as estimated by the respective algorithm matched exactly to the Q sectors contained in $\mathcal{Q}$. While the ℓ_1 algorithm gave the best result, our modified MUSIC algorithm performed nearly as well, reaching a recovery probability of nearly 100% at a similar TSNR, while requiring considerably less computation time. The most striking result is the notable improvement beyond the established MUSIC algorithms.

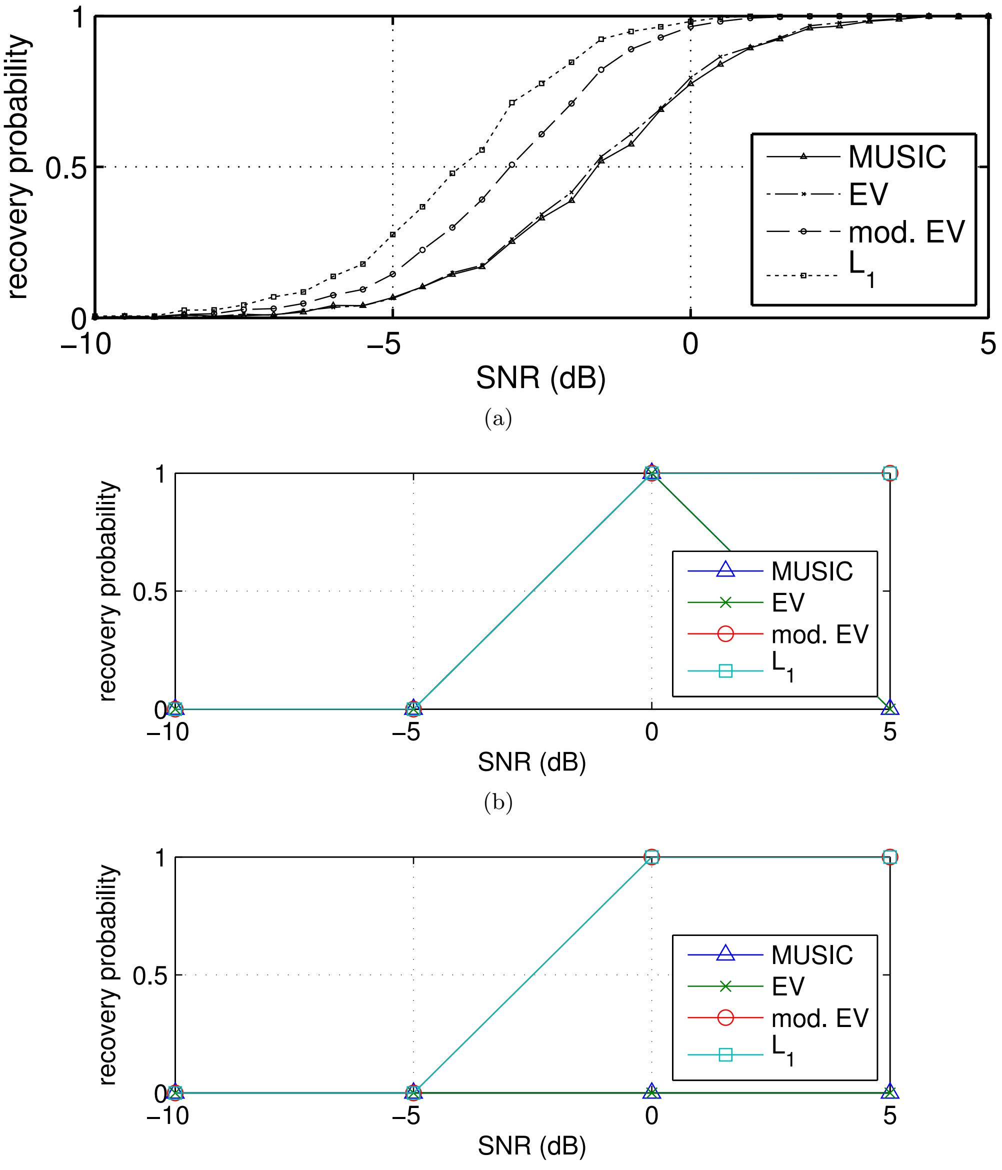

(a)

(b)

(c)

Figure 6-5: Empirical recovery probability versus SNR for $L = 19$, $P = 9$, and (a) $Q = 6$ (b) $Q = 7$ (c) $Q = 8$.

6.4 Support Recovery Failure Detection

In practice, the scene density and SNR may not be known in advance, or may evolve dynamically. As we have shown, both these quantities affect the support recovery reliability in a multi-coset array imaging system. While we could choose the number of cosets in our array to cover a worst-case scenario, in the typical case this would be rather wasteful of resources. An alternative to such an approach would be to use considerably less overprovisioning, and instead develop a method for detecting when the scene density exceeds the level at which a reliable image can be formed.

In this section, we develop such an approach. And while methods can be developed for detection such false images at high levels of abstraction using machine vision techniques, in our development we focus on the use of low-level techniques that can be easily integrated into our array processing pipeline.

The technique we develop is based on the concept of back-projection error (BPE). Consider the (P, L) multi-coset array with coset pattern $\mathcal{P}$ and a (Q, L)-sparse scene with support $\mathcal{Q}$, where both Q and $\mathcal{Q}$ are unknown. In the support recovery stage, the received information contained in $\mathbf{Y}_{\mathcal{P}}(\psi)$ is used to obtain an estimate of the support $\hat{\mathcal{Q}}$. Using the estimated support, the image is reconstructed as $\hat{\mathbf{X}}_{\hat{\mathcal{Q}}}(\psi) = \mathbf{F}^{+}_{\mathcal{P}\hat{\mathcal{Q}}}\mathbf{Y}_{\mathcal{P}}(\psi)$. Since the true $\mathbf{X}_{\mathcal{Q}}(\psi)$ is unknown, we use a *back-projection* onto the space spanned by $\hat{\mathcal{Q}}$ for comparison to the original coset response

$$\begin{aligned}\hat{\mathbf{Y}}_{\mathcal{P}\hat{\mathcal{Q}}}(\psi) &= \mathbf{F}_{\mathcal{P}\hat{\mathcal{Q}}}\hat{\mathbf{X}}_{\hat{\mathcal{Q}}}(\psi) \\ &= \mathbf{F}_{\mathcal{P}\hat{\mathcal{Q}}}\mathbf{F}^{+}_{\mathcal{P}\hat{\mathcal{Q}}}\mathbf{Y}_{\mathcal{P}}(\psi).\end{aligned} \tag{6.42}$$

Where the product $\mathbf{F}_{\mathcal{P}\hat{\mathcal{Q}}}\mathbf{F}^{+}_{\mathcal{P}\hat{\mathcal{Q}}}$ is the projection matrix onto the range of $\mathbf{F}_{\mathcal{P}\hat{\mathcal{Q}}}$.

If $\hat{\mathcal{Q}}$ is correct, the back-projection $\hat{\mathbf{Y}}_{\mathcal{P}\hat{\mathcal{Q}}}(\psi)$ should be approximately equal to $\mathbf{Y}_{\mathcal{P}}(\psi)$, provided the noise level is relatively low. We quantify this through the *back-projection error*,

$$\mathrm{BPE} = \int_0^{1/L} \|\mathbf{Y}_{\mathcal{P}}(\psi) - \hat{\mathbf{Y}}_{\mathcal{P}\hat{\mathcal{Q}}}(\psi)\|_2^2 \,\mathrm{d}\psi. \tag{6.43}$$

6.4.1 Failure detection in the absence of noise

Consider first the case where the noise level is negligible relative to the received signal power. As discussed in Section 6.2, a multi-coset array with a (P, L)-universal pattern should be able to recover the support $\mathcal{Q}$ of a (Q, L)-sparse scene in most cases given $P \geq Q + 1$. When the support estimate is recovered from the response $\mathbf{Y}_{\mathcal{P}}(\psi) = \mathbf{F}_{\mathcal{P}\mathcal{Q}}\mathbf{X}_{\mathcal{Q}}(\psi)$ is (or contains) the correct support such that $\mathcal{Q} \subseteq \hat{\mathcal{Q}}$, the back-projection is

$$\hat{\mathbf{Y}}_{\mathcal{P}\hat{\mathcal{Q}}}(\psi) = \mathbf{F}_{\mathcal{P}\hat{\mathcal{Q}}}\hat{\mathbf{X}}_{\hat{\mathcal{Q}}}(\psi) = \mathbf{F}_{\mathcal{P}\mathcal{Q}}\mathbf{X}_{\mathcal{Q}}(\psi) = \mathbf{Y}_{\mathcal{P}}(\psi), \tag{6.44}$$

and the BPE is zero. When the scene is insufficiently sparse for the array, the recovery stage fails to determine the entirety of the support and $\hat{\mathcal{Q}} \subset \mathcal{Q}$. In this case, much of the energy contained in the unidentified support sectors $\mathcal{Q}/\hat{\mathcal{Q}}$ vanishes during the back-projection operation. This behavior can be seen in Figure 6-6. Each curve represents a fixed number of cosets P for which the average BPE is plotted as a function of the number of supported sectors Q. The average BPE was calculated over 1000 trials, each trial having a random Gaussian scene evenly distributed over a randomly selected support $\mathcal{Q}$. As expected,

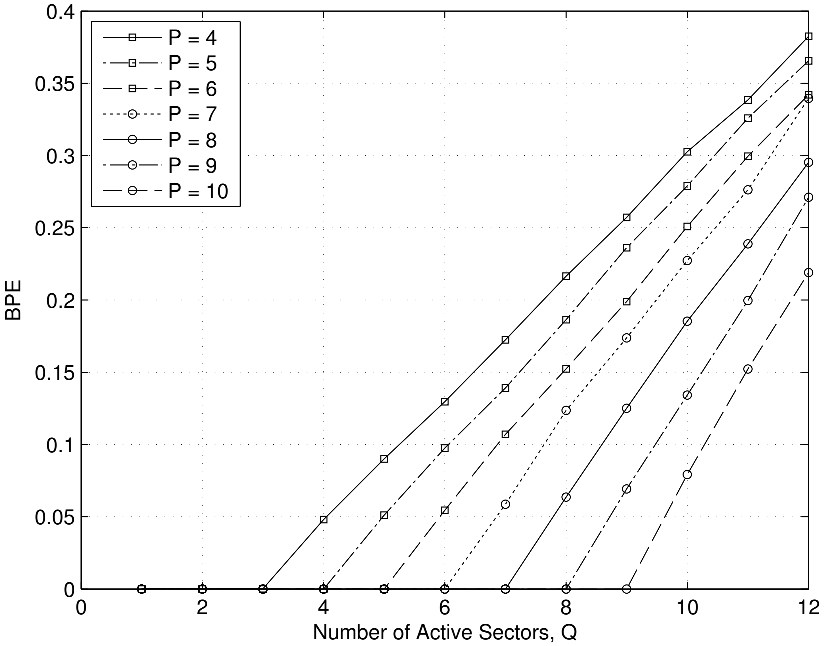

Figure 6-6: BPE versus Q, $L = 19$. Results averaged over 1000 trials.

each curve remains at zero for $Q < P$ and rises in nearly linear fashion with Q beyond this point.

6.4.2 Failure detection in the presence of noise

To understand how the presence of noise impacts the BPE, consider a scene with fixed signal power distributed over any $Q \leq P - 1$ sectors. For noise powers below some threshold level (specific to the particular values of L, Q, and $\mathcal{P}$), the support recovery will not be adversely affected. In this region, the support $\mathcal{Q}$ will be recovered successfully and the BPE will be due solely to the noise within the subspace orthogonal to the range of $\mathbf{F}_{\mathcal{PQ}}$, which will increase in proportion to the total noise power. As a consequence, failures occur with increasing likelihood for $P > Q$ at lower SNRs. Hence, a useful failure detection mechanism is to indicate when the BPE exceeds some prescribed threshold.

The choice of this threshold depends on SNR, a Figure 6-7 reflects. This figure shows the normalized BPE versus Q for different SNR values for a $(9, 19)$ multi-coset array. Rather than averaging the BPE results over every trial as in Figure 6-6, the averages are instead taken separately for the cases of successful and failed support recovery estimates. We observe that independent of Q, the failed cases consistently lie above some threshold, which varies with SNR. Defining the threshold BPE as the midpoint between the maximum success and minimum failure BPEs allows a nominal level indicating a probable failure to be determined at each SNR. Figure 6-8 illustrates the resulting BPE thresholds from this analysis for the $(9, 19)$ array. Similar analysis can be undertaken for another other particular array pattern.

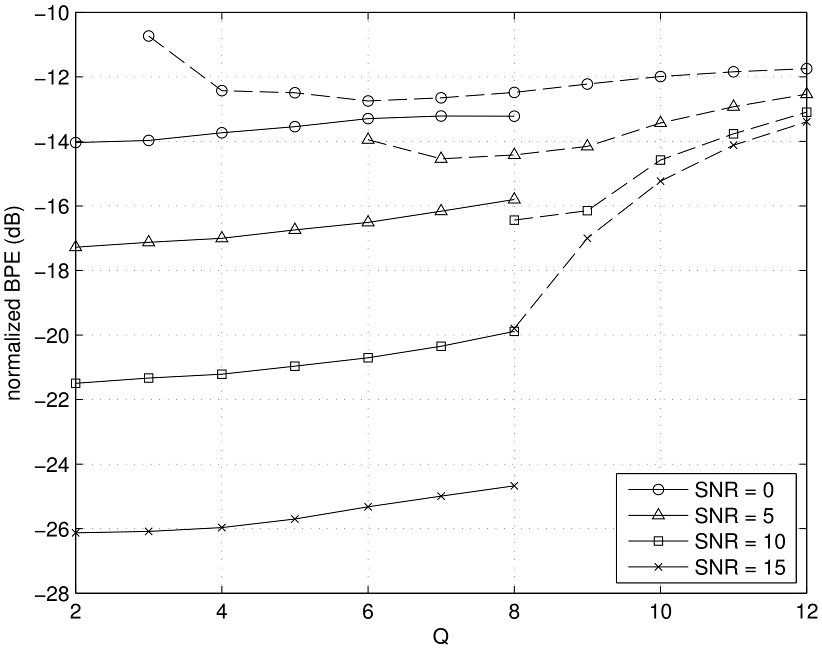

Figure 6-7: Normalized BPE versus Q, at different SNR, $L = 19$, $P = 9$. The solid and dashed portion of each curve represent the successful and failed cases, respectively.

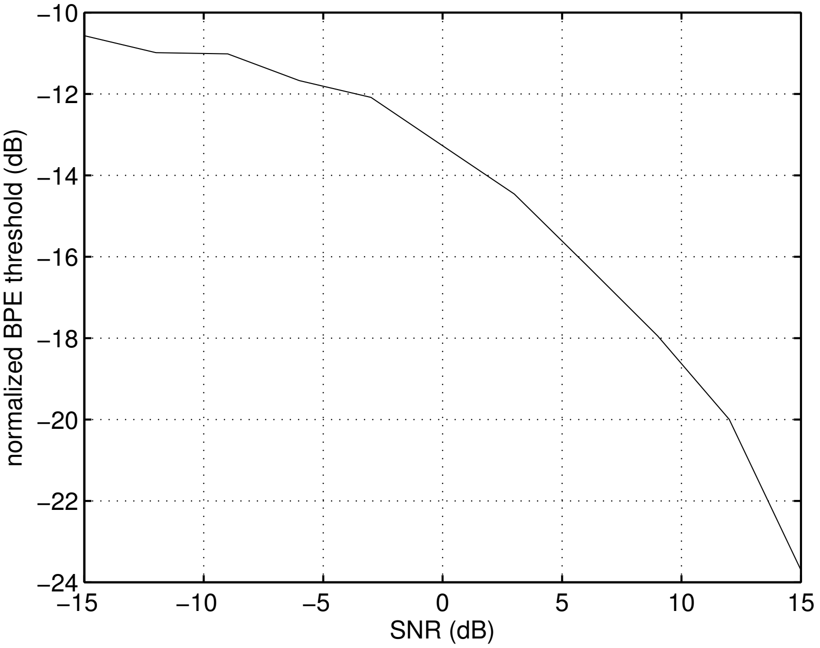

Figure 6-8: Normalized BPE threshold versus SNR, $L = 19$, $P = 9$.

Chapter 7

Multi-Coset Array Design and Application

In the previous chapter, we detailed the general principles related to the underlying concepts and performance metrics of the multi-coset array. In this chapter, we tie these principles to the practical design and operational aspects of the overall multi-coset system. To begin, we develop our approach for the design of good multi-coset array patterns over a linear aperture of length N measured in half-wavelengths. In our development, we assume the coset period L has been chosen based on the considerations in Section 6.2.3. This means that scenes of a given density are characterized by a particular value of Q, which we treat as known. For this scenario, we consider array designs with density corresponding to a number of active cosets P such that $P \geq Q+1$, consistent with our earlier development, but note that in practice the addition of at least one additional coset $P \geq Q+2$ provides large performance gains in support recovery.

We now consider the design of (P, L) multi-coset array patterns that are uniformly good for all (Q, L)-sparse scenes. Our development separately considers the high- and low-SNR regimes.

7.1 High SNR Designs

At high SNR, the correct support is recovered with high probability, so system performance is largely determined by the RSNR achieved during the scene reconstruction phase of imaging. Based on the analysis in Section 6.3.1, which reveals the peformance is dominated by the smallest eigenvalue of the measurement matrix $\mathbf{F}_{\mathcal{P}\mathcal{Q}}$. Accordingly, we seek the coset pattern $\mathcal{P}$ such that $|\mathcal{P}| = P$ for which the measurement matrix $\mathbf{F}_{\mathcal{P}\mathcal{Q}}$ remains well conditioned for all possible supports $\mathcal{Q}$ satisfying $|\mathcal{Q}| \leq Q$, i.e.,

$$\mathcal{P}^*_\kappa = \underset{\mathcal{P}\in\mathcal{C}_P}{\operatorname{argmin}} \max_{\mathcal{Q}\in\mathcal{C}_Q} \kappa\left(\mathbf{F}_{\mathcal{P}\mathcal{Q}}\right). \tag{7.1}$$

Note, however, that the sets $\mathcal{C}_P$ and $\mathcal{C}_Q$ containing the possible choices of $\mathcal{P}$ and $\mathcal{Q}$ grow rapidly with increasing L. An exhaustive search based on (7.1) requires $|\mathcal{C}_P| \times |\mathcal{C}_Q|$ calculations of $\kappa(\mathbf{F}_{\mathcal{P}\mathcal{Q}})$, which makes this design approach, while conceptually natural, unappealing from the perspective of computational complexity.

7.2 Low SNR Designs

At lower SNR, errors in the support recovery become significant, and thus system performance is more determined by the TSNR achieved during the support recovery phase of imaging. In this regime, the condition number of the induced measurement matrix $\mathbf{F}_{\mathcal{P}\mathcal{Q}}$ is less important, and the design procedure in Section 7.1 is less meaningful.

Instead, in this low SNR regime, we develop an alternate design framework inspired by the Minimum Redundancy Linear Arrays (MRLA) introduced in [54]. MRLA designs have the defining property that there are no sensor pairs having identical spacings, in an effort to yield the best representation of the full correlation matrix with the fewest number of elements.

Our approach can be viewed as a generalization of the MRLA framework that takes into account the periodicity constraint inherent in multi-coset array. In particular, we start by defining the following modulo-distance between pairs of elements l, k within a single coset period:

$$t_{lk} \triangleq \min\{|l-k|, L-|l-k|\}. \tag{7.2}$$

In turn, we count the number of times each pairwise spacing is found in a particular pattern $\mathcal{P}$. For this purpose, the *co-array* for $\mathcal{P}$ is a vector of the number of times each modulo-distance occurs in the pattern. In particular, the tth entry of $\mathcal{P}$ is the number of times the distance t occurs, i.e.,

$$[\mathbf{c}_{\mathcal{P}}]_t \triangleq \sum_{\{(l,k)\,:\,t_{lk}=t\}} s_l s_k, \quad 1 \le t \le \frac{L-1}{2}. \tag{7.3}$$

where $\mathbf{s}_{\mathcal{P}}$ is the binary selection vector with entries

$$[\mathbf{s}_{\mathcal{P}}]_l = \begin{cases} 1, & l \in \mathcal{P} \\ 0, & \text{otherwise,} \end{cases} \qquad l = 0, 1, \ldots, L-1. \tag{7.4}$$

From this perspective, $\mathbf{c}_{\mathcal{P}}$ can be viewed as a modulo version of the co-array originally defined in [54].

Finally, our desired pattern is that in which all the different spacings occur as infrequently as possible. Since the total number of spacings is the same for all patterns of length P, this corresponds to a co-array vector that is as close to constant as possible, which can be computed by selecting the coset pattern having the co-array $\mathbf{c}_{\mathcal{P}}$ with the smallest ℓ_2-norm, i.e.,

$$\mathcal{P}_c^* = \operatorname*{argmin}_{\mathcal{P} \in \mathcal{C}_P} \|\mathbf{c}_{\mathcal{P}}\|_2. \tag{7.5}$$

The rationale for this design approach comes from considering the correlation matrix associated with all L cosets

$$\mathbf{R}_{\mathbf{Y}} = \mathbf{F}\mathbf{R}_{\mathbf{X}}\mathbf{F}^{\dagger}. \tag{7.6}$$

For the moment, consider the model with uncorrelated scene sectors, i.e.,

$$[\mathbf{R}_{\mathbf{X}}]_{mn} = \int_0^{1/L} X_m(\psi)\, X_n^*(\psi)\, \mathrm{d}\psi = \begin{cases} \sigma_m^2 & m = n \\ 0 & m \neq n, \end{cases} \tag{7.7}$$

where $\sigma_m^2 = \int_0^{1/L} |X_m(\psi)|^2\, \mathrm{d}\psi$ is the signal energy from sector m. In this case, the full

Table 7.1: Examples of coset patterns $\mathcal{P}_c^*$ selected according to the co-array approach.

L	P	ρ_A	$\mathcal{P}_c^*$	c^*
7	3	0.43	$\{0,1,3\}$	1
7	4	0.57	$\{0,1,2,4\}$	2
11	5	0.45	$\{0,1,2,4,7\}$	2
11	6	0.55	$\{0,1,2,4,5,7\}$	3
13	4	0.31	$\{0,1,3,9\}$	1
13	9	0.69	$\{0,1,2,3,4,5,7,9,10\}$	6
19	9	0.47	$\{0,1,2,3,5,7,12,13,16\}$	4
19	10	0.53	$\{0,1,2,3,5,7,12,13,15,16\}$	5

correlation matrix has a Hermitian-circulant structure

$$[\mathbf{R_Y}]_{lk} = \frac{1}{L^2}\sum_{q=0}^{L-1}\sigma_q^2 e^{j2\pi(l-k)q/L}. \tag{7.8}$$

From (7.8), the dependence of the matrix entries on the relative spacing between elements indicates the importance of the pairwise spacings as represented by the $2(L-1)$ off-diagonals. Specifically, the information contained in $\mathbf{R_Y}$ can be obtained by representing each of the possible spacings a single time. The symmetries in the Hermitian-circulant structure reduce the number of unknowns by another factor of four, suggesting the entire matrix could be represented by only $\lceil (L-1)/2 \rceil$ unknowns. In practice, there will be measurement noise and some correlation between the different sectors, and as such $\mathbf{R_Y}$ will vary to some extent along each diagonal. As such, multiple occurrences of a particular pairwise spacing can be interpreted as multiple samples of noisy data. Hence, this suggests a design with evenly distributed spacings.

7.3 Pattern Computation, Evaluation, and Comparison

A quick comparison of (7.1) and (7.5) shows that the co-array based design approach entails significantly fewer computations due to the independence of this design on $\mathcal{Q}$. In this section, we further show the co-array designs are also optimal—or very close to optimal—in performance in both low- and high-SNR regimes.

To begin, we examine a set of (L,P) pairs for which the number of unique element pairs $P(P-1)/2$ is an integer multiple of the number of possible spacings $(L-1)/2$. This condition makes it possible, in principle, for a pattern to have a perfectly flat co-array distribution: each entry of $\mathbf{c}_{\mathcal{P}}$ takes the identical value $c^* = P(P-1)/(L-1)$. Examples of coset patterns fitting this description are shown in Table 7.1, along with the array density ρ_A, and the associated value of c^*.

Focusing on the $(4,7)$-sparse array in this table for purposes of illustration, note first that this array layout is depicted in Figure 6-2. We emphasize, too, that this coset pattern can be used with any number of coset periods M depending on the array length, and that the effective array density is approximately 57% of the number of elements contained in a standard array of the same length. The corresponding co-array is $\mathbf{c}_{\mathcal{P}} = [2\,2\,2]$, which reflects that there are two element pairs having each of the (modulo) spacings 1 (element

Table 7.2: Maximum condition numbers, $Q = P - 1$.

L	P	$\kappa_{\mathcal{P}_\kappa^*}^{\max}$	$\kappa_{\mathcal{P}_c^*}^{\max}$	$\kappa_{\mathcal{P}_{\mathrm{b}}}^{\max}$
7	3	1.31	1.66	2.64
7	4	2.18	2.18	3.60
11	5	4.24	4.24	17.54
11	6	5.17	5.17	20.22
13	4	2.75	3.26	15.85
13	9	6.49	6.49	33.25
19	9	13.54	13.54	1063.63
19	10	13.93	13.93	1154.08

pairs $(0,1)$ and $(1,2)$), 2 (element pairs $(0,2)$ and $(2,4)$), and 3 (element pairs $(1,4)$ and $(0,5)$).

For the values of L and P shown in Table 7.1, it is computationally feasible to determine the condition number of the measurement matrix $\kappa(\mathbf{F}_{\mathcal{P}\mathcal{Q}})$ over the sets $\mathcal{C}_P$ and $\mathcal{C}_Q$, corresponding to the high-SNR regime design framework. From these results, the maximum condition number $\kappa_{\mathcal{P}}^{\max}$ over all $\mathcal{Q}$ of length $Q = P-1$ is determined for each $\mathcal{P}$. The results for $\kappa_{\mathcal{P}_\kappa^*}^{\max}$, $\kappa_{\mathcal{P}_c^*}^{\max}$, and $\kappa_{\mathcal{P}_{\mathrm{b}}}^{\max}$ are shown in Table 7.2 for each of the (L, P) pairs in Table 7.1. Also included in this table are results for the refers to the bunched universal pattern mentioned in Section 6.2.1. This pattern, $\mathcal{P}_{\mathrm{b}} = \{0, 1, \ldots, P-1\}$, is included for the reference, and is an example of a pattern that only guarantees that the measurement matrix will have a finite condition number for all $\mathcal{Q}$.

As an initial observation, note that the bunched patterns lead to poor RSNR performance, as we would expect.

Next, note that there are many entries in Table 7.2 for which $\kappa_{\mathcal{P}_\kappa^*}^{\max}$ and $\kappa_{\mathcal{P}_c^*}^{\max}$ match, revealing that our high-SNR and low-SNR designs often yield identical patterns. Moreover, even when they differ, our low-SNR designs do not sacrifice significant RSNR peformance when used in the high SNR regime. Hence, we conclude that even at high SNR, the co-array based pattern designs are “near” optimal.

Conversely, we can also evaluate the performance of our high-SNR designs in the low-SNR regime in the two instances in Table 7.2 where the designs differ from their low-SNR counterparts. In particular, in Figure 7-1 we plot the recovery probability as a function of SNR for the $(3, 7)$ and $(4, 13)$ sparse arrays. In this case, we see that these high-SNR designs offer conspicuously poorer TSNR performance in the low-SNR regime.

Equally noteworthy, in these and all other choices of (P, L) for which simulations were conducted, the co-array pattern designs consistently yielded the lowest TSNR for reliable support recovery among all possible patterns, providing additional evidence that co-array based pattern design framework is well matched to the low-SNR regime.

While co-array based designs offer attractive performance characteristics, for coset periods beyond $L = 20$, the exhaustive search for such patterns via (7.5) over $\mathcal{C}_P$ consumes significant computation. In this regime, it is natural to replace the brute force search with a iterative optimization based on the Markov Chain Monte Carlo (MCMC) method [55]. In our experiments, we found this approach effective for quickly determining well designed coset patterns. Several examples with uniform co-arrays obtained from this procedure are shown in Table 7.3.

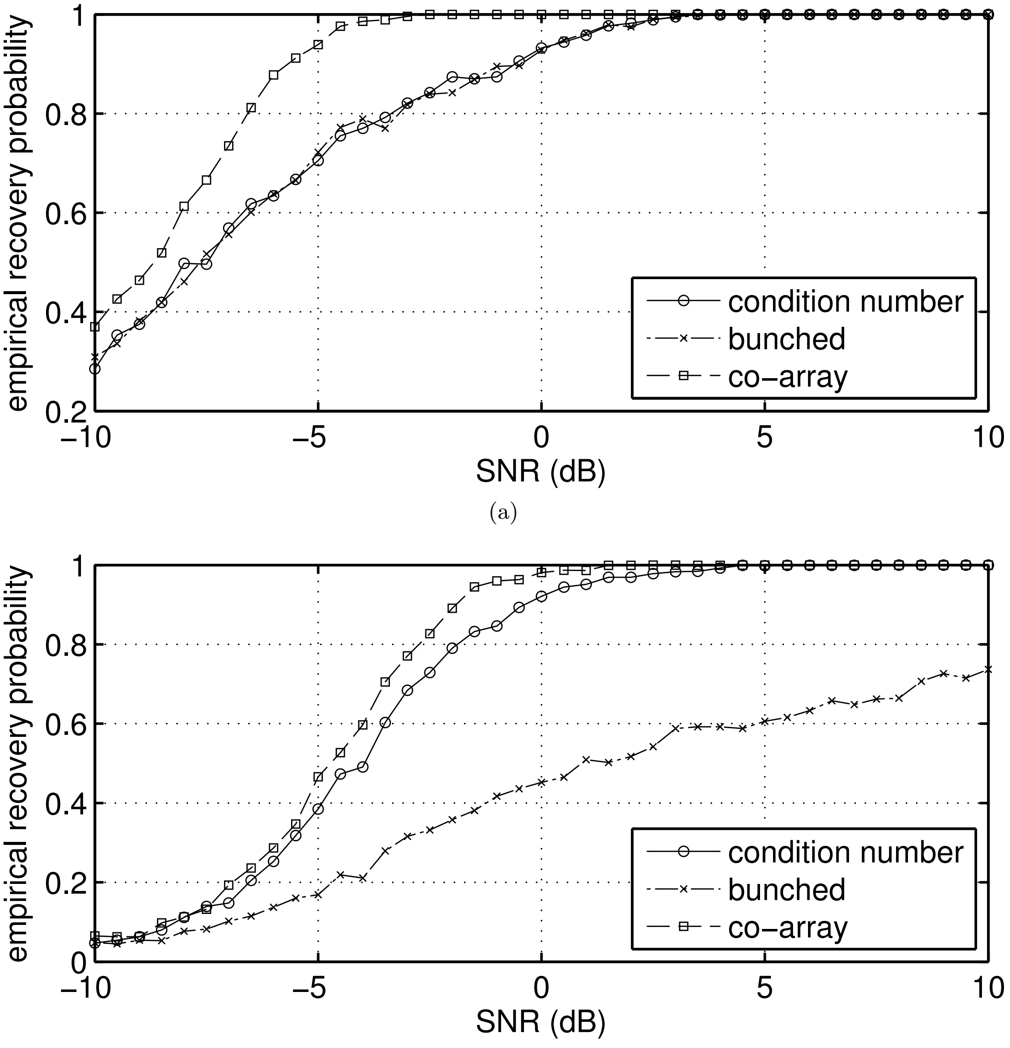

(a)

(b)

Figure 7-1: Recovery probability vs SNR for (a) $(L, P, Q) = (7, 3, 2)$ and (b) $(L, P, Q) = (13, 4, 3)$

Table 7.3: Examples of coset patterns $\mathcal{P}_c^*$ found using MCMC.

L	P	ρ_A	$\mathcal{P}_c^*$	c^*
21	5	0.24	$\{0, 1, 6, 8, 18\}$	1
21	16	0.76	$\{0, 1, 2, 3, 4, 5, 6, 7, 8, 10, 12, 13, 14, 15, 18, 19\}$	12
23	11	0.48	$\{0, 1, 2, 3, 5, 7, 8, 11, 12, 15, 17\}$	5
23	12	0.52	$\{0, 1, 2, 3, 4, 6, 8, 9, 12, 13, 16, 18\}$	6
31	6	0.19	$\{0, 1, 14, 20, 24, 29\}$	1
31	15	0.48	$\{0, 1, 2, 3, 5, 7, 11, 14, 15, 16, 22, 23, 26, 28, 29\}$	7
31	16	0.52	$\{0, 1, 2, 3, 4, 6, 7, 8, 12, 14, 16, 17, 19, 24, 25, 28\}$	8
35	17	0.49	$\{0, 1, 2, 3, 5, 6, 10, 16, 17, 18, 22, 24, 25, 27, 28, 31, 33\}$	8
37	9	0.24	$\{0, 1, 3, 9, 13, 14, 21, 31, 35\}$	2
57	8	0.14	$\{0, 1, 13, 15, 21, 24, 31, 53\}$	1

It is important to emphasize that while the coset pattern examples shown in Tables 7.1 and 7.3 can be considered "perfect" in the sense of our co-array metric, the set of patterns that are good in a practical sense is considerably larger. Indeed, small deviations from a uniform co-array generally do not significantly impact performance. Consequently, within the process of selecting $\mathcal{P}$, emphasis should be placed on arriving at a pattern for which the elements of $\mathbf{c}_{\mathcal{P}}$ are distributed reasonably evenly. In the simulations of Section 7.4, we use such a near-perfect pattern for a scenario with parameters $L = 47$ and $P = 28$.

7.4 Range-Azimuth 2-D Imaging Simulations

In this section, the multi-coset imaging techniques are applied to create two-dimensional range-azimuth images. We first develop our framework to exploit the tendency of scenes to exhibit *range-dependent sparsity.* Then, we use a simple electromagnetic simulation to generate data for an active imaging radar system composed of a single transmit element and an array of receive elements.

7.4.1 Range-dependent scene sparsity

While many scenes are not strictly sparse when viewed in solely in terms of azimuthal sectors of arbitrary range, they are often sparse in azimuth when further partitioned into range cells. In active systems, such range partitioning can be achieved through the use of standard pulse compression techniques. This suggests a natural architecture where pulse compression is used to sort content into range cells, after which our multi-coset imaging techniques are applied separately at each range.

Pulse compression techniques are well understood, and many good treatments are available in the literature. For our purposes, it suffices to keep in mind the following characteristics. For a transmitted waveform containing a range of frequencies Δf about the center frequency f_0, the inverse Fourier transform of the received frequency domain data sorts the response according to the two-way travel times of the various signals reflected from the environment. In a typical medium, each of these signals travel at the same speed, hence sorting by time effectively sorts by distance.

From this perspective, the pulse-compressed range resolution improves linearly with the bandwidth Δf. As the scene is divided in finer range cells, the resultant range-dependent sparsity profile improves, since the density at any range is monotonically non-increasing as the range cell length Δr decreases. The available *fractional* bandwidth $\Delta f / f_0$ of a particular array design is relatively fixed for any f_0. Hence, exploitation of range-dependent sparsity is inherently well suited for high frequency systems.

In the following simulations, we utilize this approach with a simulated scene that has nearly full azimuthal occupancy before range partitioning. It should be pointed out that the image reconstruction at each range is performed based on the narrowband model developed in Chapter 6 at the center frequency f_0. As the fractional bandwidth Δf increases, it may be necessary to consider a more careful general treatment, though no apparent diffusion effects are noticeable in these results.

7.4.2 2-D imaging illustration

As a demonstration of multi-coset range-azimuth imaging, consider the representative application of a millimeter-wave vehicular-mounted imaging system. Assume a center frequency

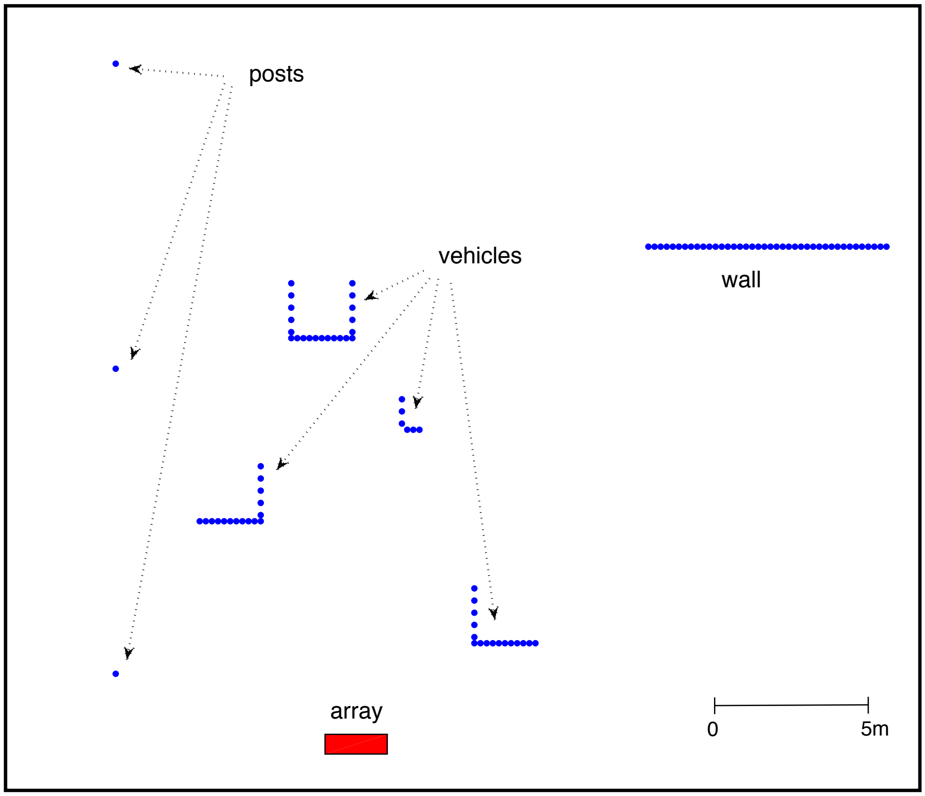

Figure 7-2: Point source model.

of $f_0 = 75$ GHz and an available aperture length of 2 m. At this frequency, an element spacing of $d_0 = \lambda_0/2 = 2$ mm implies the need for 1000 array elements in order to fully populate the linear aperture. The simple line-of-sight point target model shown in Figure 7-2 was used to simulate the array response over a frequency bandwidth of 1 GHz, which provides a 15 cm range resolution following pulse compression.

Modeling the transmitting source as a single isotropic antenna located at the center of the aperture, the frequency response was initially determined at the $N = 1000$ equally spaced receive element locations. The full standard array image is generated by first sorting the received data by range using the pulse-compression technique, and then applying (6.3) at each of the range bins. In the following images, a Hamming window [42] was applied across the array elements to aid in the suppression of sidelobe leakage, as discussed in Section 6.2.3.

The image was partitioned into sectors of equal widths $\Delta\psi_L = 1/L$ for increasing values of L in order to observe maximum sector density $\rho_{s,L} = Q_{\max}/L$ over all ranges. Following a rapid decrease, $\rho_{s,L}$ begins to level off at about $L = 50$. Based on observations that prime values of L typically yield better conditioned measurement matrices, a coset period of $L = 47$ was selected. Adhering to the aperture constraint, this allows $M = 21$ coset periods for a total number of array elements $N = ML = 987$. Using all 987 elements to generate the standard array image with SNR = 30 dB yields the result shown in Figure 7-3.

At $L = 47$ the maximum number of occupied sectors is $Q = 14$. A conservative pick for the number of cosets is $P = 2Q = 28$, resulting in an array with a density factor

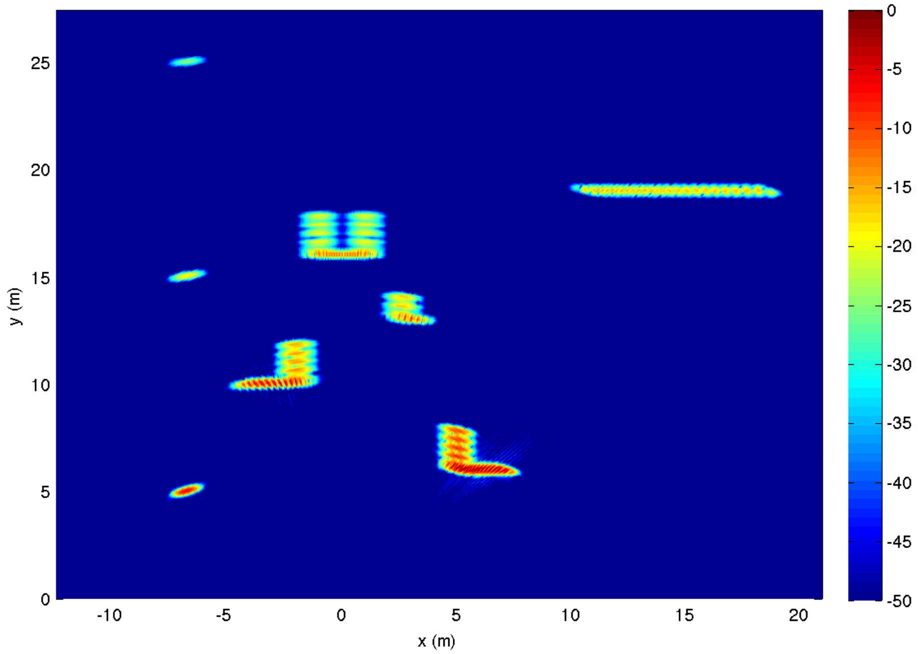

Figure 7-3: Standard array image reconstruction, $N = 987$ elements with spacing $d_0 = \lambda_0/2$. SNR = 30 dB.

$\rho_A = 0.596$. Using the MCMC technique to design the coset pattern for the $(28, 47)$ multi-coset array with $N = 588$ elements, the resultant image is shown in Figure 7-4. With this conservative choice of P, we see that the multi-coset array image reconstruction is nearly indistinguishable from the full array reconstruction.

For comparison, a uniformly spaced array with this same number of elements (corresponding to $d = d_0/0.596 = 0.839\lambda$) performs poorly, due to grating lobe effects, as shown in Figure 7-5. Indeed, this array is unable to distinguish the direction of arrival for targets outside of $|\psi| < 0.30$ and copies of image targets appear in multiple locations.

The corresponding "bunched" coset pattern also performs poorly as shown in Figure 7-6, as we would expect from our analysis. While the bunched pattern is able to determine the correct support at each range due to the conservative choice of P, it is evident that the poor conditioning of the associated measurement matrix results in a significant magnification of the noise within this support.

The noise amplification characteristics associated with the bunched pattern are even more pronounced at low SNR. To illustrate this, Figures 7-7, 7-8, and 7-9 show the image reconstructions at SNR = 10 dB for the full 987 element array, the co-array designed multi-coset array, and the bunched multi-coset array, respectively.

Figure 7-8 also emphasizes a significant feature of the multi-coset reconstruction. In contrast to the reconstruction from the full array in Figure 7-7, in which the noise appears relatively uniformly throughout the image, the image in Figure 7-8 has the noise eliminated in the sectors identified as inactive by support recovery processing.

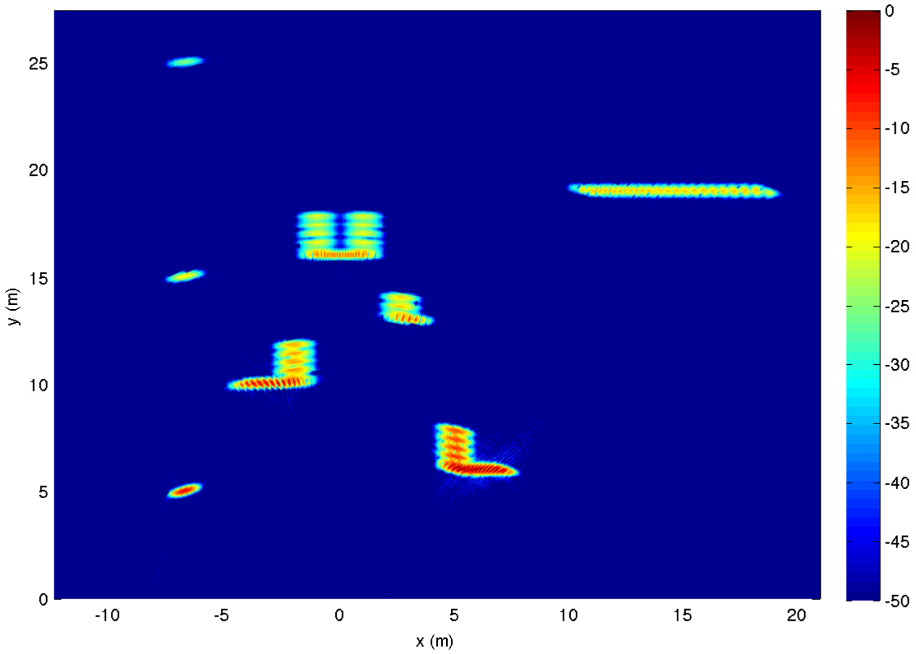

Figure 7-4: Reconstructed image for the $(28, 47)$ multi-coset array with coset pattern $\mathcal{P} = \{0, 1, 2, 3, 4, 5, 10, 11, 12, 13, 15, 16, 19, 21, 22, 25, 26, 27, 30, 32, 34, 38, 39, 41, 42, 44, 45, 46\}$. SNR = 30 dB.

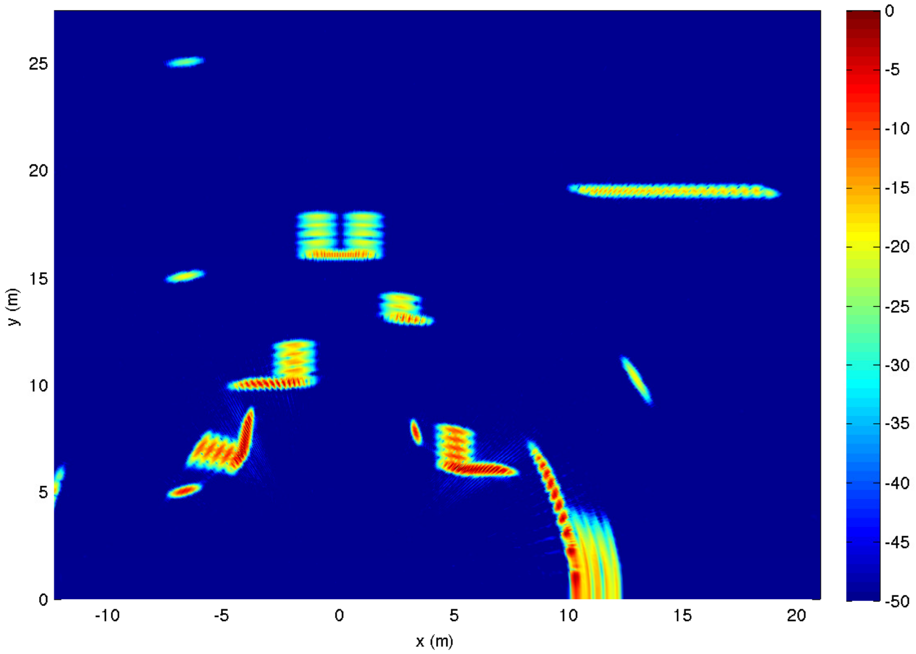

Figure 7-5: Reconstructed image from the sparse uniform array of $N = 588$ elements with spacing $d = d_0/0.596 = 0.839\lambda$. SNR = 30 dB.

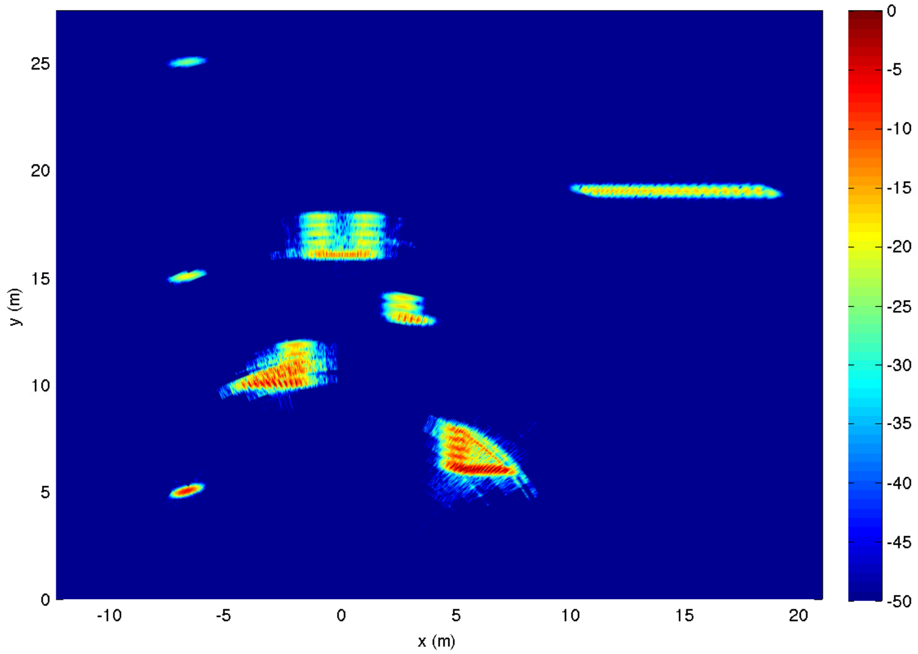

Figure 7-6: Reconstructed image for the $(28, 47)$ multi-coset array with "bunched" coset pattern $\mathcal{P}_\mathrm{b} = \{0, 1, \dots, 27\}$. SNR $=$ 30 dB.

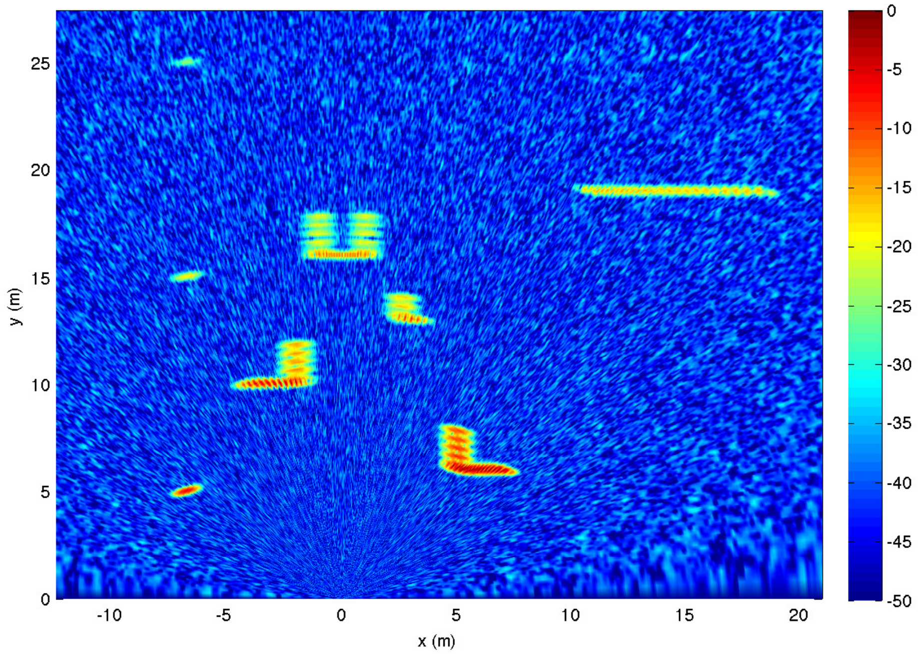

Figure 7-7: Standard array image reconstruction, $N = 987$ elements with spacing $d_0 = \lambda_0/2$. SNR $=$ 10 dB.

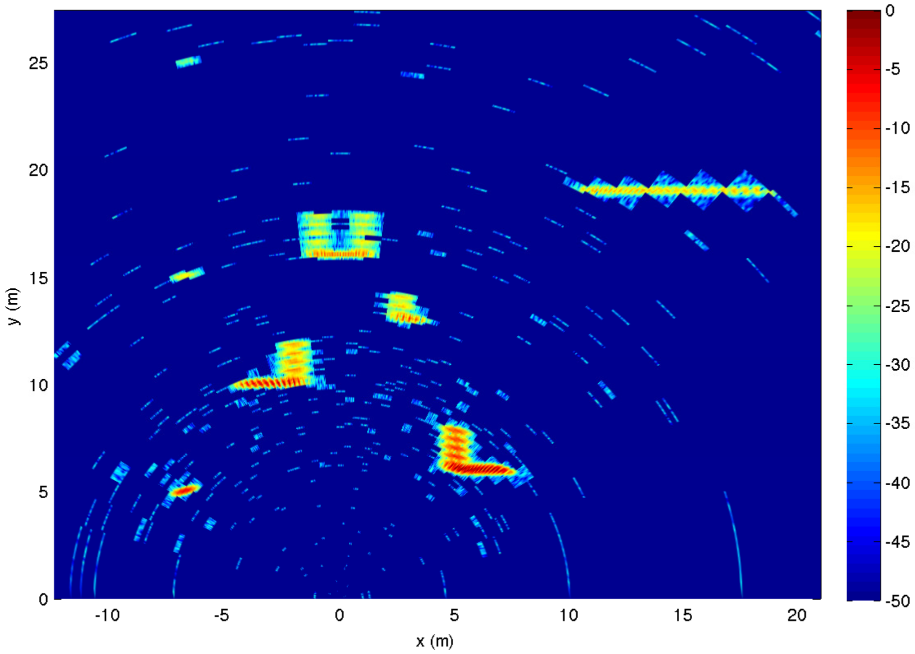

Figure 7-8: Reconstructed image for the $(28, 47)$ multi-coset array with coset pattern $\mathcal{P}$ as in Figure 7-4. SNR = 10 dB.

7.4.3 Undersparse arrays

Useful reconstructions can be obtained from multi-coset imaging even when the number of elements is strictly insufficient for the realized scene density, as we will now illustrate. In such cases, the associated reconstructions are most useful in conjunction with failure detection methods as developed in Section 6.4. In this 2-D imaging scenario, our BPE failure measure is applied at each range. Figure 7-10 shows the reconstructed images for $P \leq Q = 14$. The bar immediately to the right of each reconstruction indicates the BPE at each range.

Due to the moderately aggressive choice of $P = 14$ for this scene, the image shown in Figure 7-10a exhibits a mild degree of error at the ranges with the highest densities. This is to be expected as the number of cosets begins to be insufficient to accurately determine the supported sectors. In Figure 7-10b, the array has $P = 9$ cosets, and more severe errors begin to occur. A primary utility of having this range-dependent error indication is that when failures occur, the location can be identified and ignored, or judged with caution, without discarding results at other ranges that still have sufficiently low densities. In Figure 7-10c, the array retains $P = 5$ cosets, having reduced the total number of elements to 105 of the original $N = 987$. While the objects are showing noticeable levels of distortion, each target is still being located by the support recovery algorithm, with the most egregious corruptions being identified by the error indicator.

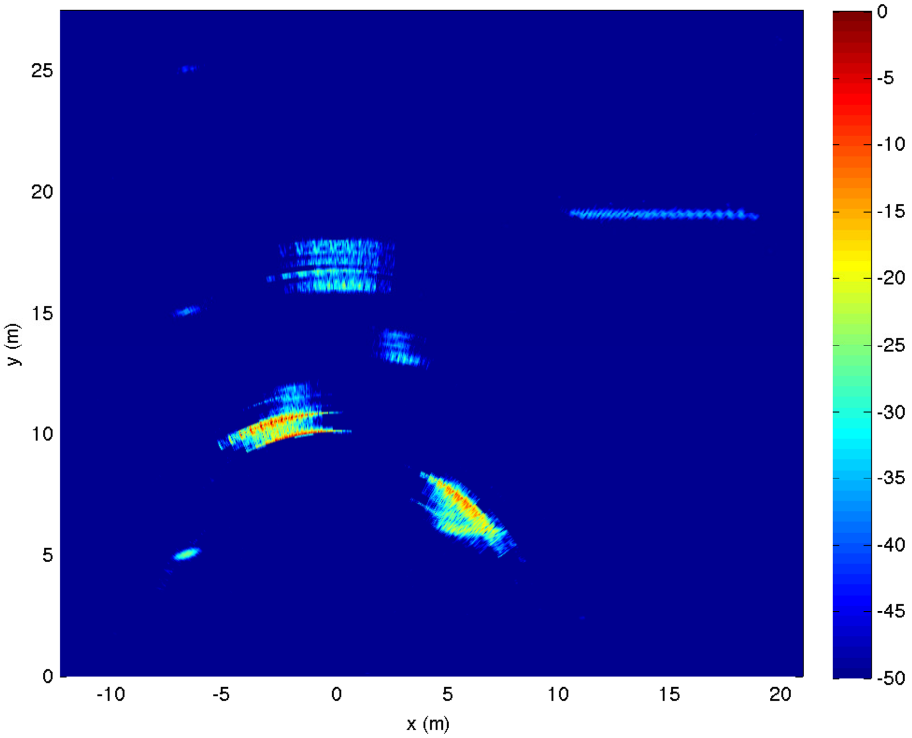

Figure 7-9: Reconstructed image for the $(28, 47)$ multi-coset array with "bunched" coset pattern $\mathcal{P}_{\mathrm{b}} = \{0, 1, \ldots, 27\}$. SNR = 10 dB.

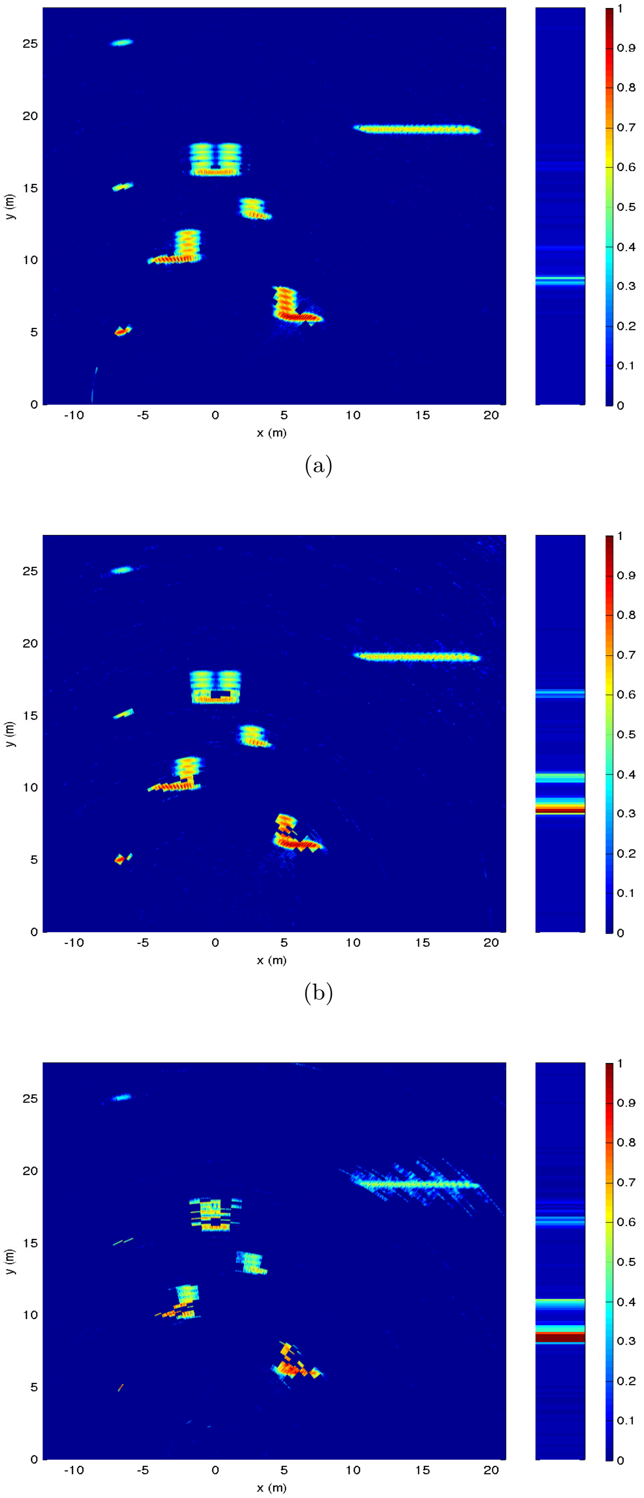

(a)

(b)

(c)

Figure 7-10: Multi-coset images with failure detection, $L = 47$ and (a) $P = 14$, (b) $P = 9$, (c) $P = 5$. SNR = 30 dB.

Chapter 8

Multi-Coset Array Experimental Validation

To show the robustness of the multi-coset array in a practical setting, measurements were performed with the use of equipment and facilities provided by MIT Lincoln Laboratory, Lexington, MA.

8.1 Hardware description

Our measurements were taken with the use of the small, portable radar platform shown in Figure 8-1. This platform is made up of four primary components:

1. The radar module, contained within the light gray box near the center of the forward face of the platform
2. A cylindrical "quadridge" transmit horn antenna
3. An identical receive antenna
4. The physical platform mount

This radar module can be controlled by attaching a laptop through the USB interface port and sending configuration and measurement commands. When a request for a radar data measurement is made, a transmit signal is sent through one of the two RF antenna ports, after which a received signal measured at the other RF port is processed and the data is delivered to the laptop.

The horn antennas are 11.5" in length and open to a circular aperture 5.25" in diameter. They support both vertical and horizontal polarization, accessed through feed ports located on the top and side of the antenna, respectively, located 5/8" from the small end of the horn. In the configuration used in these measurements, the radar module attaches to the antennas via a 90° hybrid coupler, which in turn attaches in-phase and quadrature ports to the vertical and horizontal polarization feeds, resulting in circularly polarized waves. The radar operates at a center frequency $f_c = 3.1$ GHz ($\lambda_c = c_0/f_c = 2.81$", where c_0 is the propagation speed of the electromagnetic waves), and employs a waveform with bandwidth $B = 2.2$ GHz, providing a range resolution of $\Delta r = c_0/2B = 2.68$".

The platform mount attaches to a straight rail on which it can positioned manually. By making repeated measurements at uniformly spaced positions along the rail, the measured

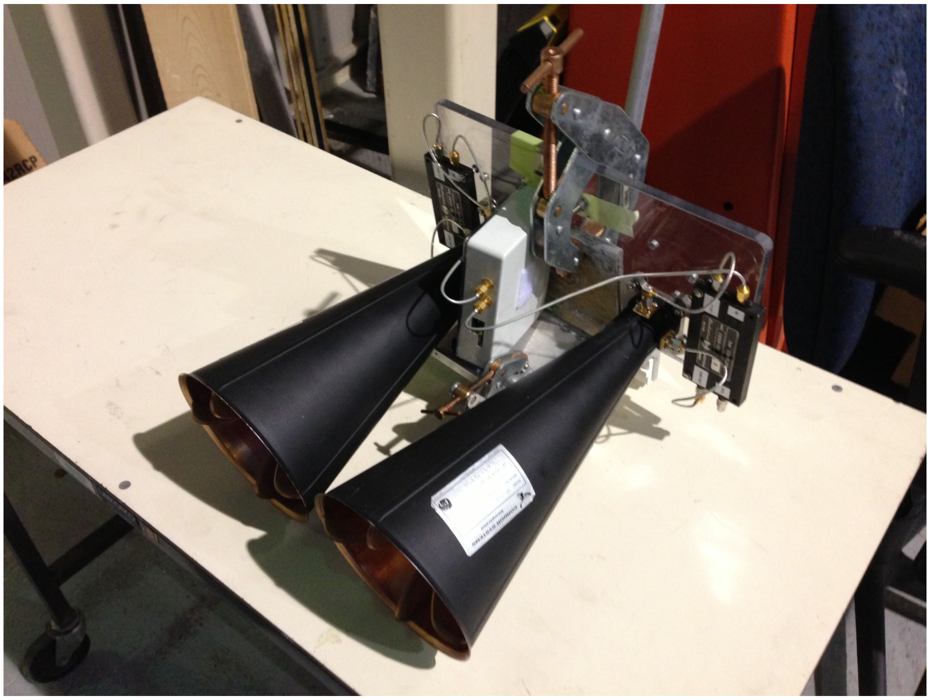

Figure 8-1: Radar antennas used in multi-coset measurements.

data can be used to synthesize the multi-channel response of a uniform linear array with elements located at the measurement positions.

The rail itself, shown in Figure 8-2, is $L = 98$" long, with uniformly spaced markings at 1" intervals. When the full length of the rail is utilized to synthesize the array aperture, the image resolution is $\Delta\psi = \lambda_c/2L = 0.0146$. The choice of the 1" spacing, rather than a spacing of $d = \lambda_c/2 = 1.4$", is necessary due to the type of measurements being made. As opposed to the *bistatic* type measurements described in the previous chapters, where the transmitting source antenna is located in a fixed position, these measurements are of the *monostatic* type, since the transmit antenna moves with the receive antenna. As a result, the relative path differences (i.e. phase variations) the for each "element" is increased by a factor of two, necessitating closer spacings. While this suggests a spacing of 0.7", the directive properties of the horn antennas act to suppress the presence of any grating lobes due to the 1" spacing.

8.2 Test Configuration and Layout

The rail-mounted radar platform was set up as shown in Figure 8-3. For target objects, four aluminum trihedral corner reflectors were mounted on non-conducting tripods approximately 25' from the rail. Three of these corner reflectors were of the type shown in Figure 8-4a, with each of the three faces being right isosceles triangles with an edge length of 8.5". The remaining corner reflector, shown in Figure 8-4b, had square shaped faces with an edge length of 9".

After placing the four targets in the configuration shown in Figure 8-5, a tape measure was used to record the positions of the reflectors relative to the array and their mounted

Figure 8-2: Mounting rail with markings indicating measurement locations.

Figure 8-3: Rail-mounted radar in experimental setting.

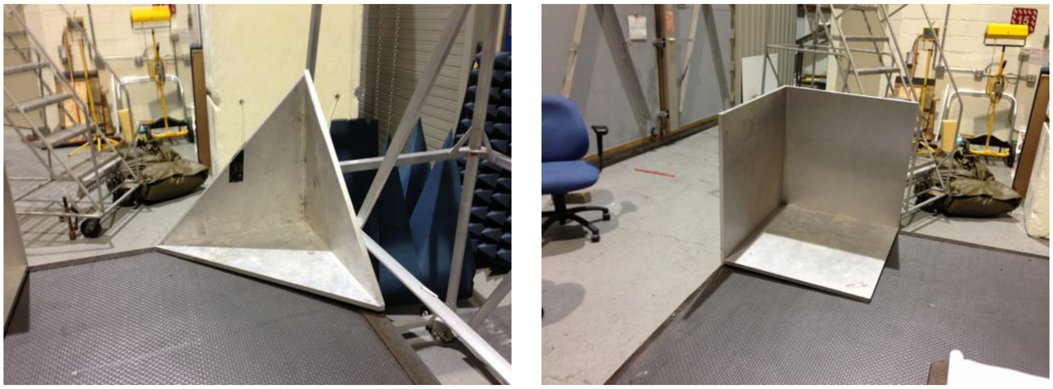

(a)

(b)

Figure 8-4: Corner reflectors used as target objects for measurements.

Figure 8-5: Target setup.

heights. The experimental layout is illustrated in Figure 8-6

8.3 Measurement Description

Once the radar platform and targets were arranged as described above, the attached laptop was used to interface with the radar hardware. To configure the system, this interface was used to specify a transmit gain of 0 dB (setting the transmitted power to the minimum level of -32 dBm), the start and stop times during which the received data is recorded and a delay time used to calibrate the system to account for the travel time of the signal through the transmit and receive feed paths. To set the delay time, several calibration measurements were taken with a single reflector placed at known distances from the radar antennas. The recording start time was used to suppress the signals which, rather than radiating away from the antennas, couple directly from the transmit to the receive horn. For these measurements this was set to correspond to a two-way travel time for a range of 5 meters. The stop time was set in a similar manner for a range of 14 meters, allowing enough extra time to account for multi-path reflections while stopping well before any reflections from the surrounding external objects (such as the vehicles seen in Figure 8-5, located approximately 20 m from the radar platform) could interfere with the desired measurements.

To remain consistent with the bistatic radar imaging model developed in the previous chapters, a preliminary conversion was used to synthesize the equivalent response to a single isotropic transmitter located at the center of the linear aperture. This response was obtained using conventional array processing techniques by first generating the image using an appropriate backprojection approach [56], and then projecting the response onto the array elements directly using (6.2).

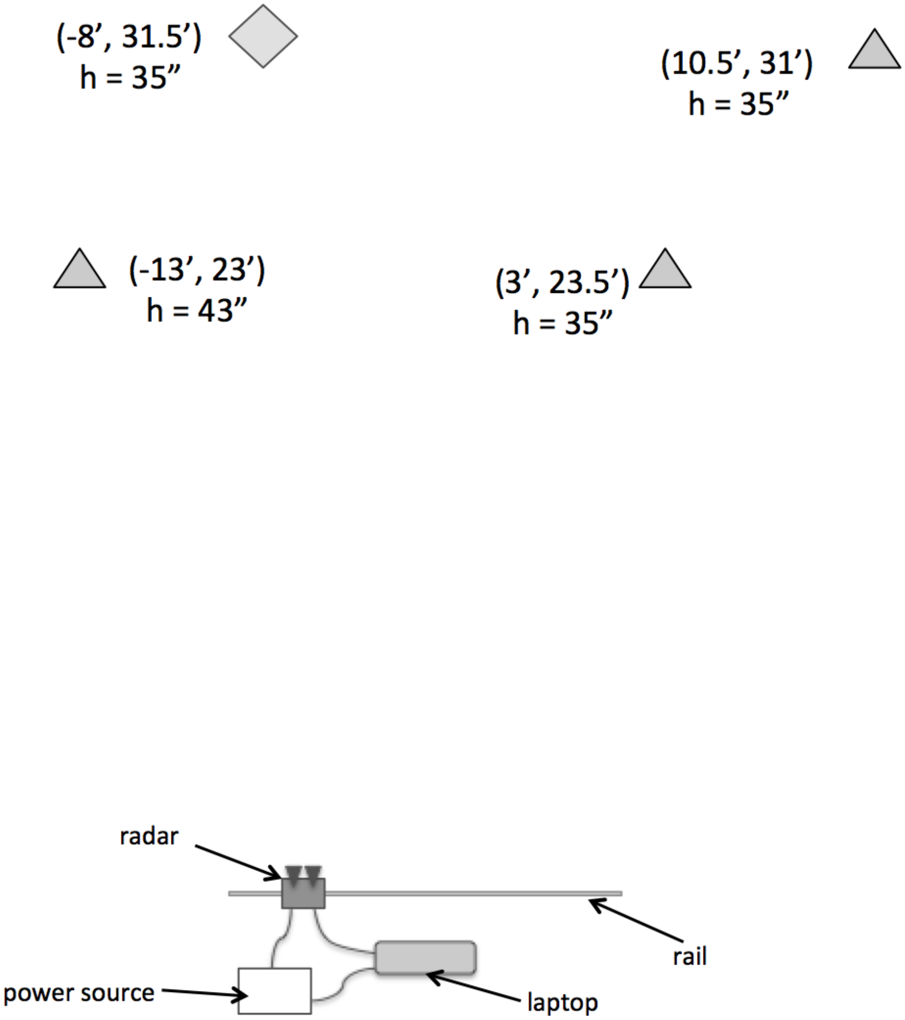

Figure 8-6: Experimental layout and geometry.

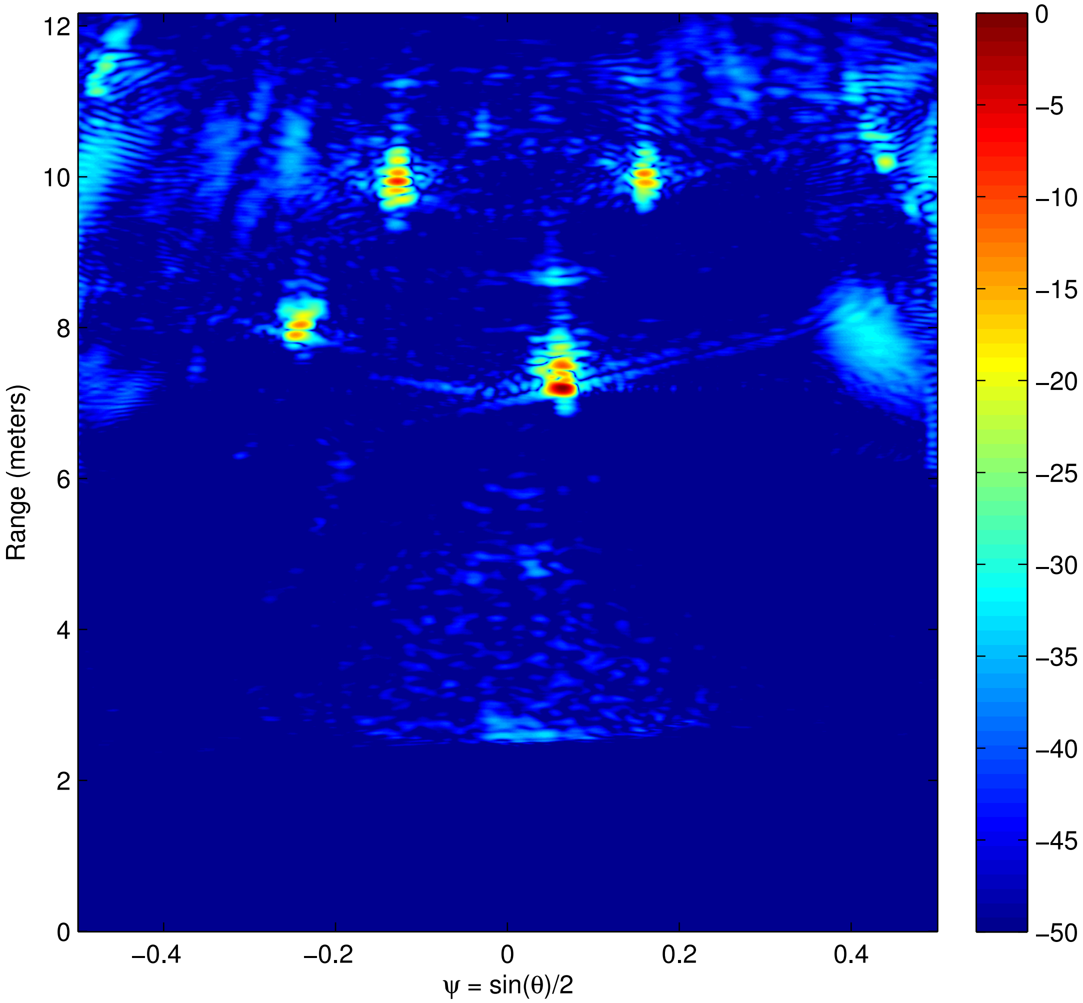

Figure 8-7: Full array image in ψ-range space.

After sorting the response data by range, the image obtained using the full 98 array elements was found from (6.3) at each range cell. The result in $\psi -$ range space is shown in Figure 8-7 over a range of 50 dB relative to the peak response level. In this format, we can see most clearly the range-dependent scene density. The four reflector targets appear as the primary responses at their expected locations, as can be seen in the image shown in cartesian coordinates in Figure 8-8. When taking these measurements, the radar takes a large enough number of repeated samples such that the ambient and receiver noise is significantly suppressed through averaging. The remaining responses throughout the image result from residual effects of the monostatic to bistatic conversion as well as the naturally occurring side lobes. For our purposes, this additional "noise" is useful for demonstrating the degree of robustness the multi-coset array exhibits with such practical effects. We can see that the most densely populated ranges are located in the neighborhood around 10 meters from the array, where we can expect to observe reconstruction errors due to support recovery failures to appear as the multi-coset array utilizes fewer cosets.

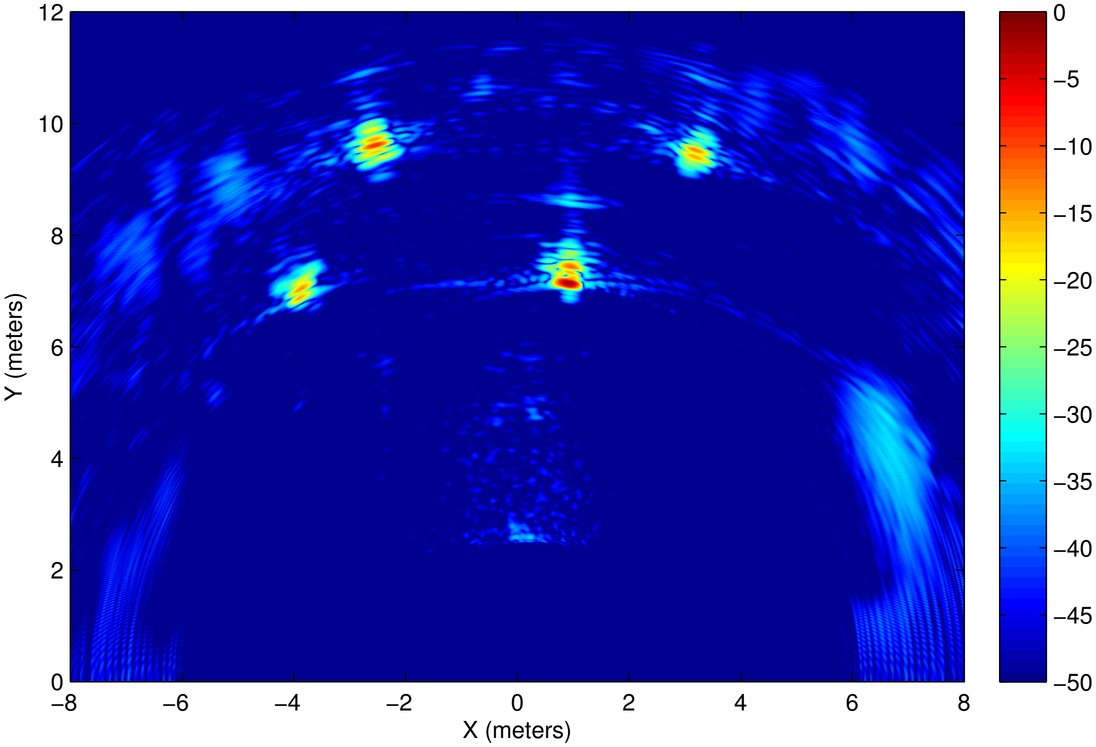

Figure 8-8: Full array image in cartesian coordinates.

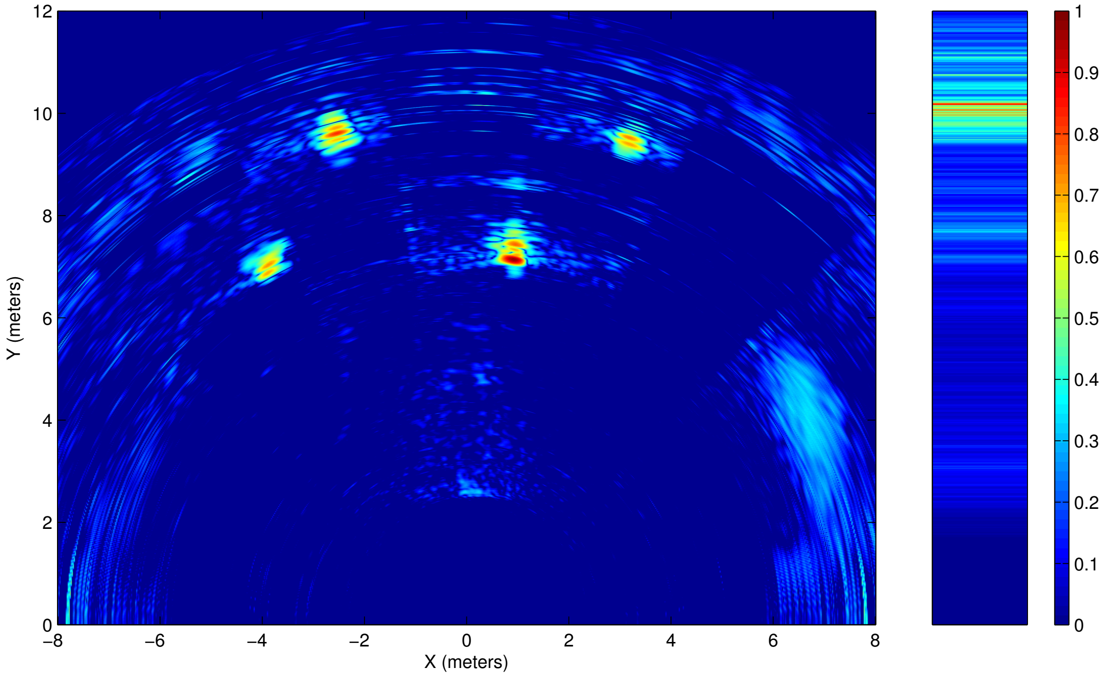

Figure 8-9: Reconstructed image result and range dependent back projection error from measured data for an array sparsity of 71.4%. $L = 7$, $P = 5$, $\mathcal{P} = \{0, 1, 2, 3, 5\}$.

8.4 Multi-Coset Image Results

In determining an appropriate multi-coset array layout, a coset period of $L = 7$ was chosen so that the corresponding $L = 7$ scene sectors were small enough to allow for the targets to lie within several different sectors while still having $M = 14$ coset periods — a large enough number such that troublesome finite array effects, in particular, any rank deficiencies in the support recovery stage, would be unlikely. Additionally, the "good" coset patterns $\mathcal{P}$ for any number of active cosets $P \leq L$ are easily established, with so-called "perfect" patterns for both $P = 3$ and $P = 4$.

Starting with $P = 5$ cosets, Figure 8-9 shows the multi-coset image using $MP = 70$ out of the possible $ML = 98$ array elements. In this result, we see the clear reconstruction of the four target objects as well as much of the background responses. The BPE is displayed to the right of the image and shows a moderate level of error at the ranges containing the target objects. This is to be expected as the BPE accounts for differences between the response before and after the sector support is utilized. In the event that a non-trivial level of response is located outside the support, this adds to the BPE even though the support may be correct. Hence, in this result, the additional responses due to the target side lobes outside of the support will in general yield a non-zero BPE.

With $P = 4$ cosets, we obtain the multi-coset image using $MP = 56$ of the possible $ML = 98$ array elements seen in Figure 8-10. In this case, the BPE at range of 10 meters indicates a more cautionary likelihood of errors. However, this appears to be due to missing range-sidelobes, seen most clearly for the target near $(X, Y) = (2.5, 9.5)$ meters. The image still provides a good reconstruction of the main response for each target, and there are no noticeable false targets throughout the image.

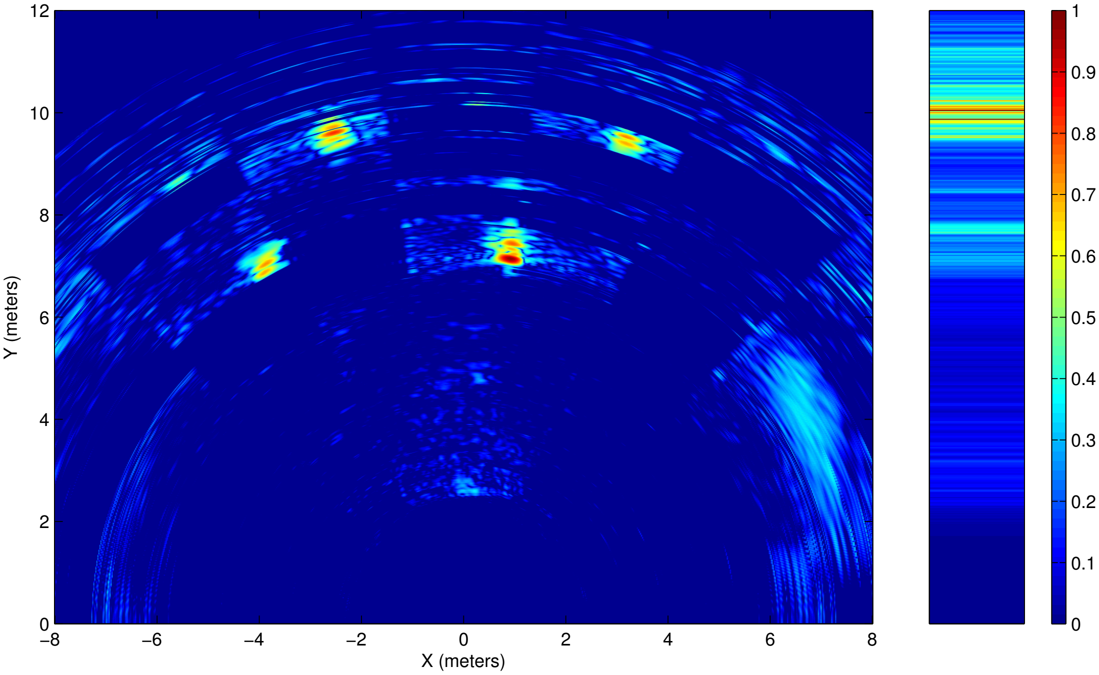

Figure 8-10: Reconstructed image result and range dependent back projection error from measured data for an array sparsity of 57.1%. $L = 7$, $P = 4$, $\mathcal{P} = \{0, 1, 2, 4\}$.

Using $P = 3$ cosets results in the image shown in 8-11. At this array sparsity, we begin to see more troublesome errors. Recall from our development that the multi-coset array with P cosets can detect a maximum of $Q = P - 1$ support sectors, meaning in this case, the array can select only two sectors at each range. Hence, at the ranges containing the two target objects, there is limited tolerance for the non-trivial response levels outside of the appropriate sectors. Note that these errors are different in nature than those seen at higher array densities in that when the reconstruction algorithm misses the correct support sectors, it can result in an attempt to place the target within an incorrect sector in a manner that best reflects the data. Here this is occurring as false targets appearing in the sectors to the left and right of the correct sector.

For the sake of illustrating a “catastrophic” failure, the response for $P = 2$ is shown in Figure 8-12. In this result, the algorithm is forced to select a single sector in which it must determine the response that most closely matches the measured data. This shows up as both complete support recovery failures, as seen by the entire misplacement of one target, and an additional target-like response that the reconstruction places alongside the closest target in the center sector.

8.5 Remarks

The experimental results appear consistent with the expectations given by the analysis developed for the multi-coset array. As predicted, the image fidelity was maintained as long as the number of active cosets remained greater than the number of occupied sectors. While the use of the same reconstruction algorithm as in the case of the synthesized radar data

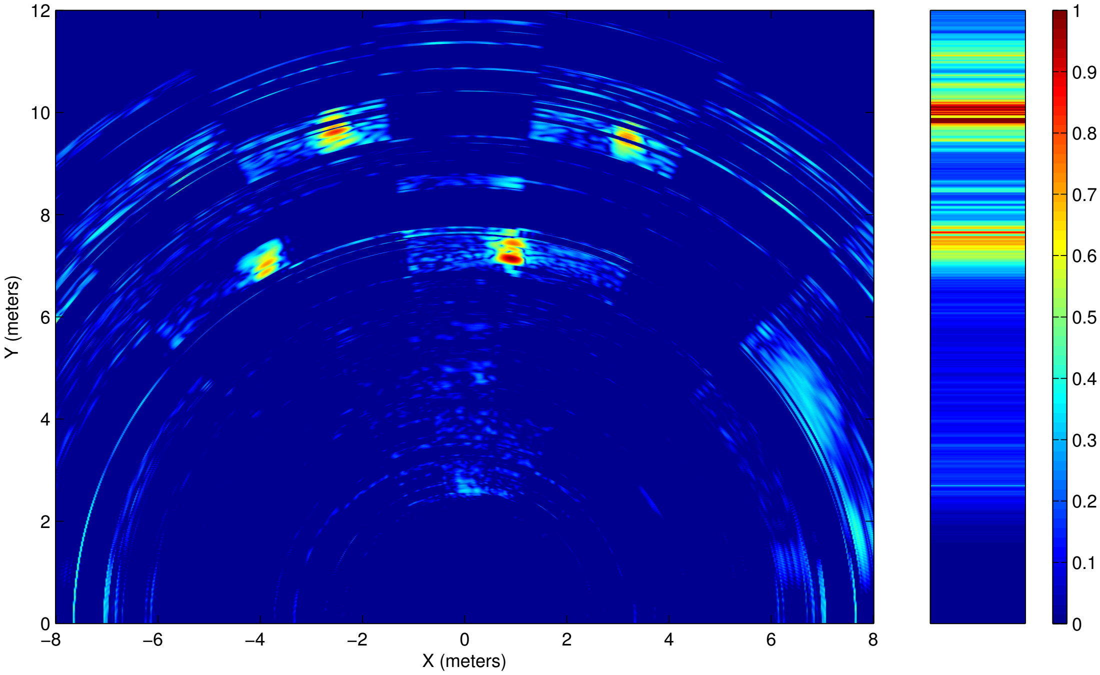

Figure 8-11: Reconstructed image result and range dependent back projection error from measured data for an array sparsity of 42.9%. $L = 7$, $P = 3$, $\mathcal{P} = \{0, 1, 3\}$.

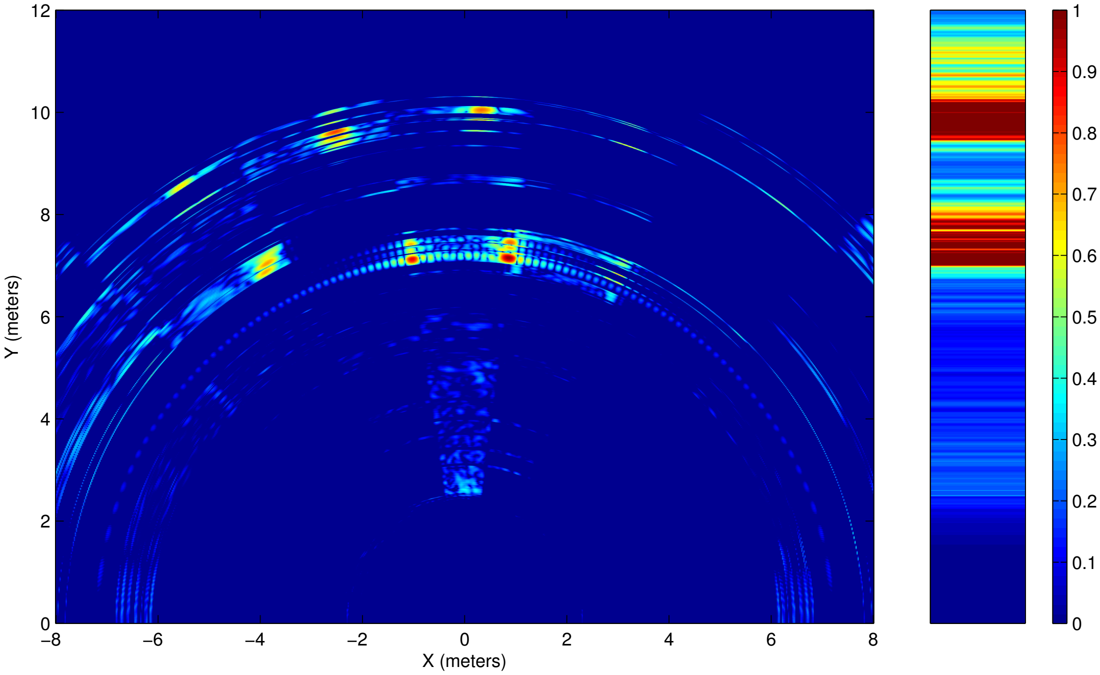

Figure 8-12: Reconstructed image result and range dependent back projection error from measured data for an array sparsity of 28.6%. $L = 7$, $P = 2$, $\mathcal{P} = \{0, 1\}$.

in Section 7.4 demonstrates a level of agreement with our development model, additional experimentation efforts to determine whether other environments may have characteristics in which disagreements with the model could become evident.

Of particular interest would be the inclusion of larger distributed, less “point-like” targets than the corner reflectors used in these measurements. While the likelihood of the physical contents of separate sectors having enough similarities such that the coherence issues described in Section 6.2.2 would arise, it may be the case that certain multi-path responses could lead to the appearance of sector coherence from the perspective of the algorithm. Were such events to result in a breakdown in the use of the MUSIC based support recovery algorithm this would become evident in the back-projection, suggesting the use of a secondary algorithm suited to the coherent case in these situations. As such, further work to understand the need for and the implementation details of this type of system modification is warranted.

The use of the repeated monostatic radar measurements in place of a full multi-coset array seems valid. However, as is the case in all engineering endeavors, each layer of assumption distinguishing the model from the final system allows for the possibility of unexpected consequences. Thus a complete validation of the multi-coset array will necessitate the fabrication of a dedicated array in order to determine whether any such consequences affect the array performance in a meaningful way. One clear distinction is the omission of any mutual coupling effects in these measurements. While coupling played an important role in the analysis of the dense $\Delta\Sigma$ array, it is less likely to affect the performance of the sparse array, in which the electromagnetic interactions between elements will be less severe. In consideration of the nonuniform array design, it should be noted that if the *inactive* cosets are manifest as “missing” elements, this may affect the element patterns in a manner not considered in our analysis model. Further, with the recurrent nature of the array, this would mean each coset would be associated with a unique pattern shared by all of its constituent elements. While it may be possible to compensate for this effect in the reconstruction algorithm, this would then be contingent on the calibration of these patterns, adding complexity in both the overall design process as well as the additional processing. A more pragmatic approach can be achieved by including the inactive coset elements as so-called “dummy” elements. Recall that it is not the physical antennas that lead to the high cost of phased arrays, but the complicated circuitry behind the front end. The inclusion of the additional inactive cosets, match-terminated with simple resistive loads at their terminals, would remove the issue of nonuniform element patterns without incurring an appreciable increase in overall costs. In fact, as we visualize large-scale millimeter wave implementations on apertures that would conventionally require many thousands of elements, it may be the case that it is more convenient to fabricate the array in this fashion, rather than needing to specify the particular nonuniform structure.

Due to the moderate number of measurements, the relatively small coset period length of $L = 7$ limited the variety of array sparsity levels and particular coset patterns the could be examined. Larger values of L would permit a greater ability to validate the performance of the co-array design technique, one of the primary contributions of this thesis. Further, a longer coset period would allow for a more gradual decrease in the array density as the number of active cosets is reduced, as well as a smaller fraction of occupied sectors for the scene. As a result, these experimental results give a somewhat modest indication of the capability to decrease the array sparsity made possible by the multi-coset array. In consideration of this and the above comments, we look forward to future experimental investigation of full-scale, dedicated multi-coset arrays.

Chapter 9

Conclusions and Future Work

This thesis has presented the architectures and associated algorithms for the design, operation, and processing of two digitally-enhanced antenna arrays. While the specifics of each array differ greatly, this research has the common thread of identifying and understanding the practical aspects related to the application of both designs. To conclude this work, we now provide an summary of the research and resulting insights, as well as the implications for future research directions.

The Dense $\Delta\Sigma$ Phased Array

The $\Delta\Sigma$ array was introduced via the notion of phase quantization, a concept which is related to signal discretization in analog-to-digital converters. From this, we extended the concept of oversampled $\Delta\Sigma$ ADCs to form the foundation of dense $\Delta\Sigma$ phased arrays. Under the model of independent and identically distributed quantization errors, the equivalence between the ADC and the phased array was demonstrated in terms of the expected quantization noise power and its dependence on the level of temporal or spatial oversampling, described by the density ratio R. Namely, for a fixed aperture, we saw that the SQNR improved by 9 dB/octave, where each octave refers to a doubling of the array density ratio. The initial 3 dB/octave is due to the natural averaging associated with the increased number of array elements, with the remaining 6 dB/octave resulting from the error canceling mechanism of the $\Delta\Sigma$ excitations. We then saw from numerical simulations for an array of isotropic elements that the SQNR increased at a slightly lower rate as the white noise model became less applicable with the increasing array density—a consequence of the smaller phase progression applied to the more closely spaced elements. Further, it was observed that by increasing the amplitude of the quantized excitations relative to the ideal excitations, the errors held more closely to the white noise model, thereby recovering the 9 dB/octave dependence. However, this came at the cost of reduced power efficiency, a property unique to the application of $\Delta\Sigma$ to the context of phased arrays.

We then compared the quantization distortion of the 2-bit $\Delta\Sigma$ array to conventional arrays of up to 5-bits of phase resolution and saw the improved robustness of the $\Delta\Sigma$ array with respect to phase errors, a particularly significant feature for millimeter wave applications. This observation is important in establishing the potential utility of the design as technology pushes into increasingly higher frequency regimes.

We demonstrated the ability to apply the dense $\Delta\Sigma$ technique to planar arrays and provided two types of $\Delta\Sigma$ excitation schemes for the rectangular lattice geometry. The first of these allowed the quantization errors to be decomposed along both array dimensions, resulting in a 3 dB improvement in the SQNR while maintaining the 6 dB/octave $\Delta\Sigma$ dependence of the linear array. This 3 dB advantage is particularly useful at small density ratios when the potential for increasing the number of elements is limited. For higher density ratios, the second $\Delta\Sigma$ scheme was even more beneficial: though lacking the initial 3 dB improvement, this approach resulted in an SQNR improvement in proportion to 12 dB/octave. In both cases, these SQNR improvements are in addition to the natural 6 dB/octave averaging improvement. The analysis of these planar array results made use of the idea of the $\Delta\Sigma$ kernel, which provides a foundation for the tractable extension of the analysis to arbitrary (uniform) array geometries.

By employing the more evolved free excitation array model, we concluded that rather than affecting the utility of the $\Delta\Sigma$ beamforming technique in a deleterious manner, the mutual coupling in the dense array environment in fact was seen to be helpful due to more directive embedded element patterns, which helped suppress the most troublesome pattern distortions near the extents of real space. A moderate increase in the quantization noise resulted from variations in the embedded patterns of the elements near the array edges, though this is of only moderate concern in the intended application space of array lengths greater than a few wavelengths, for which such effects are relatively benign.

For the isotropic array element model, we found the $\Delta\Sigma$ array to have a moderate loss in the narrowband power efficiency of 1-2 dB (compared to the equivalently dense array with ideal excitations) resulting from the increased excitation amplitudes required by the $\Delta\Sigma$ array to scan the quantization errors into imaginary space. However, it was demonstrated that with the use of the simple scan impedance matching network, the densely packed array yielded better efficiency performance than the conventional half-wavelength spaced array over both wider scan regions and frequency bandwidths.

Using element gain patterns and mutual coupling measurements for a twelve element linear array, we validated the $\Delta\Sigma$ development and analysis. While the existing array hardware prevented the ability to vary the physical element spacing, the effective density ratio was varied by adjusting the electrical distance between elements over a range of frequencies. We observed relatively close agreement with the expectations that the noise power would decrease with R^2, the discrepancy being reasonably explained by variations in the array efficiency and the nature of the element patterns over the frequency range.

These results are encouraging even before taking into account the issues of operating outside the intended frequency band of the array, the modest density ratios, and the small number of elements. We also observed that the issue of setting the amplitude ratio proved less problematic than previously indicated by the analysis of the isotropic array elements. In general, the phase patterns of practical array elements will differ from the linear responses associated with the hypothetical isotropic element, from which we can conclude that the "inherent" power efficiency reduction indicated by the initial analysis will be less concerning in practical settings.

The Sparse Multi-Coset Imaging Array

Our development of the multi-coset array expressed the notion of beamforming in the context of image formation. After presenting the core concepts of scene sector sparsity, the multi-coset array structure, and the two-stage image reconstruction algorithm, we showed that in high SNR settings, it is possible to produce the identical image attainable by a uniform half-wavelength spaced imaging array, provided the multi-coset array density is greater than the scene sector density.

The initial reconstruction stage, support recovery, in which the algorithm determines the sectors wherein lie the image targets, can be formulated in a compressive sensing setting as a multiple measurement vector problem. The solution of such problems requires that the measurement matrix be of rank greater than the number of occupied sectors. This implies the need for a minimal number of coset periods equal to this same value. Further, as the sector sparsity decreases with the length of each coset period—which determines the number of sectors—the benefit of long coset periods along with the minimal number of these periods can be used to dictate the appropriate setting of these parameters for a given overall aperture length.

In consideration of the effects of noise, the reconstruction SNR was shown to be related to the ambient SNR—equal to the SNR of the image formed by the standard uniform array—by the condition number of the multi-coset measurement matrix. Consequently, beyond the requirement for a universal coset pattern, which guarantees a finite condition number, the reconstruction SNR finding implies the further desire for a minimal condition number over all possible sector supports.

A more critical aspect of noise was seen through the threshold SNR, that is, the minimum SNR at which the support recovery stage of the reconstruction algorithm can reliably determine the correct sector support. We saw that this threshold SNR depended on the particular algorithm choice, and that this had important practical implications. The use of the MUSIC direction-finding algorithm resulted in a significant reduction in computation time compared to the convex ℓ_1 minimization approach, though this came at the cost of a several dB increase in the threshold SNR. To address this, a modified direction-finding type algorithm was discovered within this research which maintained the computational benefits of the conventional MUSIC algorithm at a much less severe cost with respect to the threshold SNR. Because the possibility of crossing the threshold SNR persists outside of the most conservative multi-coset sparse designs, a computationally simple failure indication stage was introduced, based on the concept of back projection error. This approach is easily implemented as a third stage in the reconstruction algorithm to provide a measure of confidence regarding the possibility of erroneous results in the support recovery stage due to either increases in the scene sparsity or decreases in the SNR below the threshold level.

An improved design technique for selecting the coset pattern, adapted from the co-array design approach associated with the sparse minimum redundancy linear array, was presented here. Previous research regarding multi-coset sampling suggested coset pattern designs based on the minimax optimization of the associated measurement matrix condition number. While this approach implied optimal reconstruction SNR performance, the problem of designs optimized for the minimization of the threshold SNR remained open. Through extensive numerical experimentation, our result was shown to provide optimal threshold SNR performance in all cases, while maintaining the same, or nearly the same, reconstruction SNR performance as designs based on the condition number criteria. In addition, the co-array design procedure represents a significant reduction in design complexity due to its independence from the sector support, resulting in a reduced optimization search space by an order of a square root. Further, we found that for large array geometries at which an exhaustive search over even this reduced space becomes untenable, the Markov Chain Monte Carlo technique was particularly well suited for determining coset pattern designs.

Using simple electromagnetic models to generate the radar response to a simulated scene of target objects, we demonstrated the reconstruction of two-dimensional (range-angle) images, employing the concepts of both range-dependent sparsity and back projection error to examine the behavior of the multi-coset array at a variety of array sparsity and SNR levels. For further validation of this sparse array design, experimental measurements were performed to demonstrate these same principles. As in the case of the $\Delta\Sigma$ array experiments, even with the less than perfect operational conditions resultant from the limitations imposed by the availability of dedicated hardware, the results for the multi-coset array tests were consistent with our development and analysis.

Future Research Areas

A number of topics for future areas of research follow directly from the material presented throughout this thesis. For example, it would be of interest to examine the application of the $\Delta\Sigma$ design technique to other common array geometries, such as cylindrical or ring arrays. Such research would include determining whether the $\Delta\Sigma$ error passing schemes presented here are appropriate, or if any particular aspects of this geometry suggest a more suitable, potentially advantageous approach to be exploited. Further, it would be useful to compare the behavior of any such array to the linear $\Delta\Sigma$ array regarding the relations between the element density and the resultant pattern distortion. Another interesting example is the hexagonal (sometimes referred to as triangular) planar array lattice. Beyond the well-understood characteristics of such planar designs, this geometry permits an extensive variety of error passing forms that may result in notable reductions in quantization noise even at very low density ratios.

Another consideration is the feasibility of *higher-order* $\Delta\Sigma$ structures. In this work, our $\Delta\Sigma$ technique is modeled on the first-order $\Delta\Sigma$ modulator[1], due to a concern for stability in light of the array-specific issue of power efficiency, as well an overall desire for simplicity throughout our architecture. However, it may be the case that alternative error passing techniques can improve the array performance under certain conditions, and hence further investigation could prove to be of value.

One of the major contributions in this research for the multi-coset array was the strong performance of our modified MUSIC algorithm, which itself leads to a number of questions. Perhaps most interesting is whether this modified form would be of benefit to other applications in which the MUSIC algorithm is commonly employed. It is our belief that the joint utilization of both the “signal” and “noise” subspaces have some potential performance drawbacks (e.g., in the asymptotic limit in which the estimated subspaces converge to the correct value with high probability). Any additional estimate variance resulting from this is likely to be a larger issue in so-called “super-resolution” direction finding applications than in the relatively low-resolution usage here of determining the target support sectors. Still, the promising results regarding the notable improvement over the standard MUSIC algorithm suggests further consideration.

On a related note, recall that although the modified MUSIC algorithm regained much of the performance lost in the effort of utilizing the simpler polynomial-time direction finding algorithm, as opposed to the more computationally intensive ℓ_1 convex optimization, the latter technique was still able to provide reliable results at a lower SNR. Depending on the

---

[1] The two planar $\Delta\Sigma$ approaches described in Section 3.6 may be interpreted as exhibiting traits of higher-order $\Delta\Sigma$ modulators, though it was deemed sufficient to develop these ideas directly from the first-order linear $\Delta\Sigma$ to avoid unnecessary confusion

specific application needs (i.e. reliability vs. data throughput rate), it would be easy to implement an additional algorithm feature that, in the event of a likely failure indication, revisits the support recovery stage using the more reliable optimization. While this would not be of benefit in the case of a sparsity based failure, such feature could prove useful in difficult dynamic SNR environments. We will look at a similar type of BPE responsive architecture later in this chapter.

In addition to these topics, the following sections describe promising directions for future research into expanding the depth of analysis and the potential benefits of the $\Delta\Sigma$ and multi-coset arrays.

9.1 Delta-Sigma Amplitude Tapering

Although our attention was focused on the suppression of phase quantization errors, the $\Delta\Sigma$ excitation technique has the additional advantage of being able to recreate the effect of nonuniform amplitude excitations without the need for any means of controlling the physical amplitude used to excite each element. The $\Delta\Sigma$ quantizer treats the discrepancy between the desired and the applied amplitudes in the same way it treats the phase errors. That is, rather than tracking the intended excitations themselves, it tracks the excitation errors and effectively works to cancel out these errors in the beam pattern.

A commonly used example of a nonuniform amplitude taper was developed by Taylor [41, 57, 58] to produce patterns with a specified sidelobe level. Applying this to the array of length $L = 20\lambda$, we can see the ability of the $\Delta\Sigma$ excitations to decrease the sidelobe level to -30 dB in Figure 9-1. While the pattern for $R = 4$ closely resembles the ideal pattern near the main lobe, the noise shaping effect is insufficient for the suppression of quantization distortion beyond $|k_z| > 0.75$.[2] At a density ratio of $R = 6$, the pattern is quite close to the 30 dB goal, and by $R = 8$, any remaining distortion falls below the intended sidelobe level.

In the selection of the appropriate $\Delta\Sigma$ array design, it is reasonable to expect that the density ratio should be large enough to ensure that the expected noise power falls below the target sidelobe level. This however does not guarantee the elimination of any spurious quantization lobes in all cases. On the other hand, overcompensating will lead to potentially unnecessary increases in overall costs and design complexity. As such, the questions of the appropriate system needs as addressed for the uniform amplitude setting in this thesis warrant revisiting for the nonuniform amplitude taper.

Regarding the efficiency of the $\Delta\Sigma$ array relative to the conventional array, the formulation for the uniform amplitude setting suggests that the lack of any physically realized tapering of the array weights in the $\Delta\Sigma$ case will exacerbate the effective loss in efficiency. A fair treatment of this topic requires further consideration as to how amplitude tapers are implemented conventionally. If the particular amplitudes must be allowed to vary, this will typically be implemented by way of controllable attenuation or amplification of signals at the individual element level. These approaches are inherently lossy, and hence, much of the efficiency lost by the $\Delta\Sigma$ array in order to steer the amplitude errors outside of real space is offset by the losses occurring in the conventional array.

When it is sufficient to keep a fixed amplitude taper, this can be implemented within the array feed network through the use of unequal power dividers [37] if this initial effort is deemed worthwhile to avoid the losses described above. This might suggest that the

---

[2] As previously stated, this effect will be lessened for the majority of practical array elements.

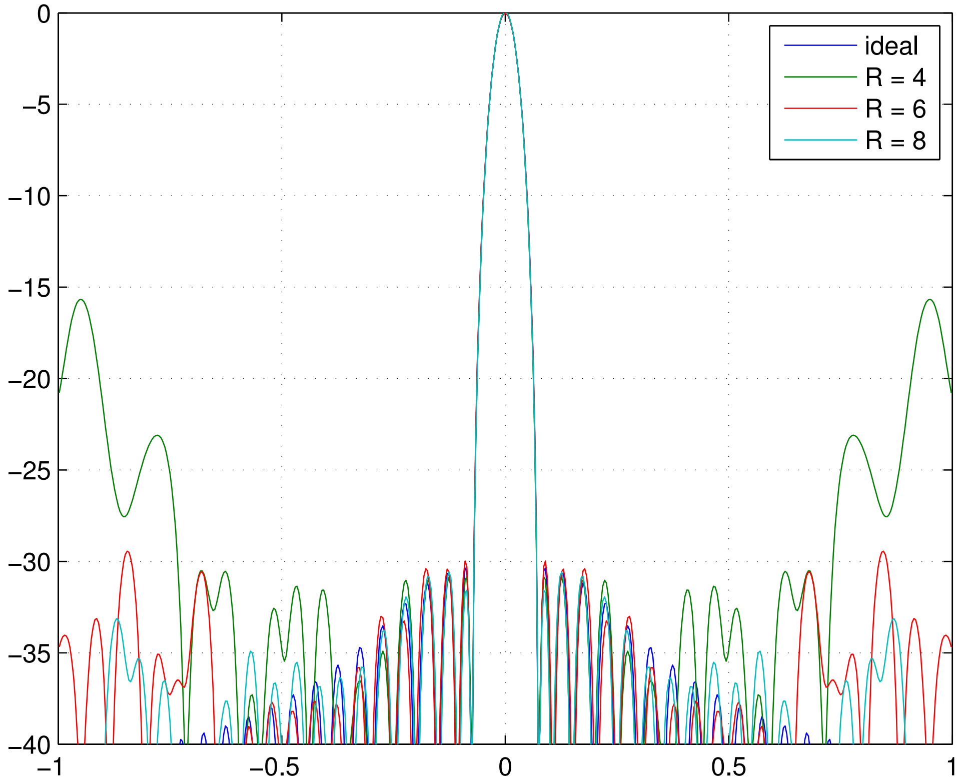

Figure 9-1: Power patterns for ideal and $\Delta\Sigma$ arrays of length $L = 20\lambda$ with 30 dB Taylor windows.

difference in efficiency performance for the $\Delta\Sigma$ array is unresolvable; yet this raises the question of whether a similar feed network can be utilized in the $\Delta\Sigma$ array in a beneficial way. This idea itself has a number of interesting possibilities.

- The "incident power gap" can be reduced such that the ratio of $|\hat{w}_n|/|w_n|$ can be made nearly constant with respect to n. This allows the efficiency considerations to be quite similar to the uniform amplitude setting (where this ratio was the fixed constant γ), which we observed from the measured results of Chapter 5 to be a relatively small concern in practical settings.

- As opposed to the relatively white behavior of $\{q_n\}$ for the uniform taper, the error would no longer be identically distributed in the sense that σ_q should scale roughly with the taper level at each element. Consequently, this would relieve the need to move to large density ratios to ensure desired pattern responses.

- The increased density of the $\Delta\Sigma$ array implies a commensurate increase in the complexity of the tapered feed network. However, due to the $\Delta\Sigma$ error suppression capability, the need for a precise representation of the desired amplitude taper is eliminated. For example, instead of applying the exact Taylor window, a much simpler linear taper could be used to achieve the majority of efficiency and noise reduction benefits, leaving the "finer grain" tuning of the excitations to the $\Delta\Sigma$ mechanism.

This last point has the additional implication that a class of amplitude tapers could be supported by a sort of "amplitude envelope" to allow for the improved pattern and efficiency performance, while maintaining a level of flexibility to apply a variety of amplitude tapers in the adaptive setting. From a broader perspective, this begins to show the extensive potential made possible with the $\Delta\Sigma$ concept. While our analysis chose to develop the $\Delta\Sigma$ array in the context of cost effective array design, this is really only one aspect of the more general contribution of a new perspective in the design and operational characteristics of the phased array.

9.2 Topics in Random Matrix Theory in Multi-Coset Analysis

Certain aspects of the multi-coset analysis in this thesis, namely, the topics of the modified MUSIC algorithm, the coset pattern design optimization, and the threshold SNR, lack a complete sense of rigor. In each of these cases, the research objective was to determine either a system design approach or the relevant behavior within the low SNR, limited sample size (here, the number of coset periods) setting. Unfortunately, the preponderance of existing analyses on related topics rely on asymptotic techniques [59], singularly unsuited for reaching meaningful conclusions in this endeavor. However, while outside the scope of this research, it appears that the field of random matrix theory [60] may provide the necessary tools to reach the following research objectives.

While the performance of the modified MUSIC algorithm is encouraging, it would be nice to provide a more rigorous justification than the intuitive reasoning that led to its conception. Further, there remains the possibility of alternative subspace weightings that may outperform our current implementation. It is expected that a random matrix theory approach to the entire problem has the potential to provide the formality required to

- Justify the improved results as compared to the standard MUSIC algorithm seen in the experimental simulations
- Determine the regime of conditions in which use of the modified algorithm is appropriate
- Prove or disprove the optimality of the modified algorithm and determine, if applicable, a more optimal form
- Utilize this understanding to recognize the potential application space for such modifications

In much the same manner as the above discussion, the closely related topics of the coset pattern design and the threshold SNR leave open several questions that, while not particularly concerning in a practical sense, remain unanswered: although the co-array coset pattern design technique is based on sound intuition and yielded optimal threshold SNR levels in each of many numerical experiments, is there a way to prove explicitly that this is the optimal design? Also, for a specified set of array and scene parameters, is there a method of calculating the expected threshold SNR analytically?

9.3 Nested Multi-Resolution Multi-Coset Arrays

Because the scene sparsity level will vary, the multi-coset array sparsity must be chosen with care. For a fixed number of elements, this choice represents a design tradeoff between the resolution level of the array and the maximum scene density for which the array can give accurate results. If the array design is too sparse, a nonzero failure rate is to be expected. However, too conservative of a design, while perhaps providing consistently accurate results, also will provide consistently low resolution results. In a sense, such a design dedicates a proportionally significant number of elements in preparation for a high scene density occurrence, regardless of how often this happens. In light of this, it may be preferable to have the ability for the array resolution to adapt to different scene densities.

A variation on the standard multi-coset array, the *multi-resolution multi-coset* (MRMC) array, has the potential to address the desire for adaptability by means of an architecture composed of the union of multiple *nested* multi-coset arrays. As an illustration, consider the example shown in Figure 9-2, in which the MRMC array $\mathcal{A}_{\mathrm{MR}}$ is formed by the union of the three basic multi-coset arrays $\mathcal{A}_0$, $\mathcal{A}_1$, and $\mathcal{A}_2$. These nested arrays share a common coset period of $L = 7$ with unique lengths and coset periods specified by

$$\begin{aligned}
\mathcal{A}_0 &: M_0 = 6, \mathcal{P}_0 = \{0, 1\} \\
\mathcal{A}_1 &: M_1 = 4, \mathcal{P}_1 = \{0, 1, 2, 4\} \\
\mathcal{A}_2 &: M_2 = 2, \mathcal{P}_2 = \{0, 1, 2, 3, 4, 5\} \\
\mathcal{A}_{\mathrm{MR}} &= \mathcal{A}_0 \cup \mathcal{A}_1 \cup \mathcal{A}_2. \qquad (9.1)
\end{aligned}$$

Using this nested structure, the element responses of the longest and sparsest constituent array $\mathcal{A}_0$ can be used to form high-resolution images if the scene is sufficiently sparse. If not, the BPE technique can be used to indicate a failure at this resolution, at which point the reconstruction algorithm is repeated with the element responses of the shorter yet denser $\mathcal{A}_1$, and so forth. With this approach, the MRMC array $\mathcal{A}_{\mathrm{MR}}$ is reliably able to provide

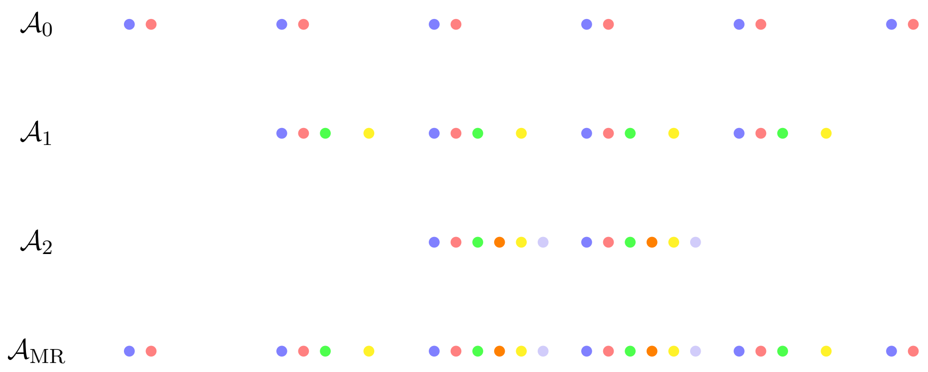

Figure 9-2: MRMC array $\mathcal{A}_{\mathrm{MR}}$ and constituent arrays $\mathcal{A}_0$, $\mathcal{A}_1$, $\mathcal{A}_2$ from (9.1).

low-resolution images for scene sector occupancies of up to $Q = 5$ out of the $L = 7$ total sectors, without sacrificing high-resolution capabilities in the case of less dense scenes.

The MRMC array can be interpreted by comparing the above example to a basic multi-coset array with the same total number of elements, having the same total length, $M = 6$, with a fixed number of cosets $P = 4$ in each period. If the scene density is expected to be low for the most part, yet potentially too great for the array to reconstruct at some times, this system must either tolerate failures at these events, or be redesigned to have, for example, $M = 4$ and $P = 6$. In this latter case, the higher resolution performance is lost entirely. In contrast, instead of rededicating all of the elements contained in the outermost coset period, $\mathcal{A}_{\mathrm{MR}}$ repositions only half of these elements within the inner nested array, thus dedicating fewer resources to these infrequent high scene density occurrences. This general behavior is summarized in Figure 9-3. The marked points along the dashed line represent fixed resolution multi-coset arrays with the same number of elements as the MRMC in (9.1), while the marked points along the solid line denote the three possible states simultaneously available to $\mathcal{A}_{\mathrm{MR}}$.

While the above is simply intended as an illustrative example, the benefits of the additional design flexibility are clear. There remains a number of ways in which this overall concept requires further development. Most significantly, a design strategy should be formulated which incorporates both a probabilistic model for the scene density and some value or cost function associated with the resultant image resolution. Additionally, the simplistic operational approach described above remains inefficient in that each stage of the nested reconstruction utilizes only a subset of the available information from the array. More sophisticated reconstruction algorithms that make use of the sparse outer arrays at high scene densities as well as the entirety of the dense inner arrays at low scene densities could be used to improve both the reliability and reconstruction quality made possible by this particular structure. The key goal here is to find such an approach that retains the ability to exploit the remaining structure of the MRMC, thus avoiding the need to use more computationally complex compressive sensing techniques.

9.4 “Ultra-Sparse” Multi-Coset Arrays

In Section 7.4, we saw how the use of the very standard radar technique of separating a scene into a number of range bins allows an otherwise cluttered scene to be viewed as a

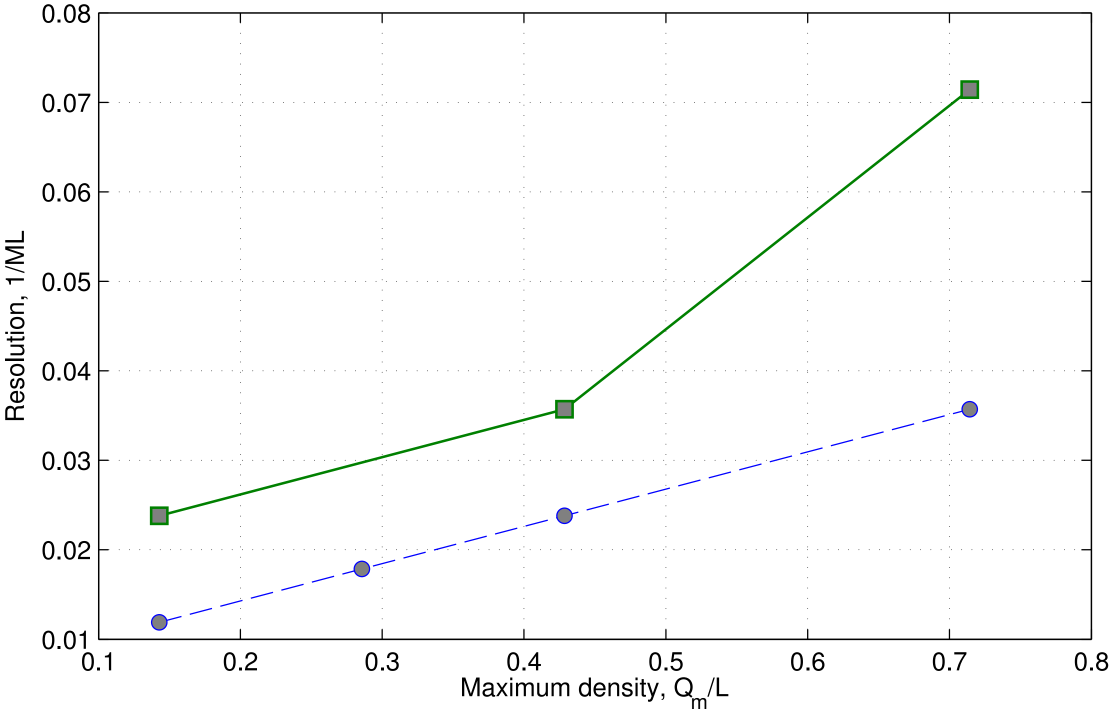

Figure 9-3: Characterization of array resolution versus maximum scene sector occupancy ($Q_{\max} = P - 1$) for the 24 element MRMC array shown in Figure 9-2 [cf. (9.1)]. Circular markers along the dashed line represent four distinct *fixed* multi-coset array geometries. Square markers along the solid line denote the three operational states simultaneously available to the MRMC array.

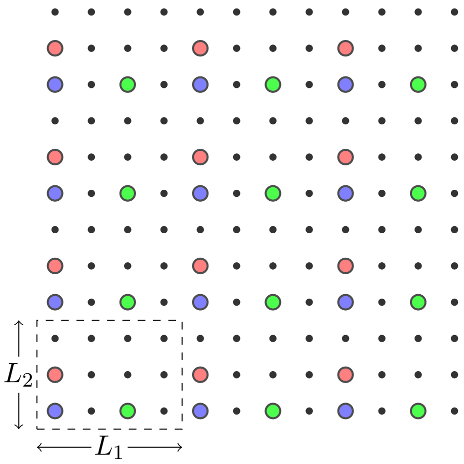

Figure 9-4: Planar multi-coset array on rectangular lattice.

series of individual sparse scenes. In doing this, the opportunity for the use of the sparse multi-coset array is extended. In this section, we describe additional means of leveraging existing radar techniques to extend even further the possibility of creating sparse array designs.

9.4.1 Planar multi-coset arrays

The extensions of multi-coset sampling to the case of two-dimensional signals was introduced by Feng and Bresler in [61] and received further attention in the subsequent paper by Venkataramani and Bresler [62]. The application of these techniques to two-dimensional imaging arrays was developed therein for the class of rectangular-lattice planar arrays by replacing the linear periodic coset pattern with rectangular tiles. An example of this is shown in Figure 9-4, in which each tile of twelve lattice points contains three active elements, shown in distinct colors for the purpose of illustration. With this two-dimensional recurrent structure, each coset becomes a sparse rectangular array with uniform element spacing of $L_1 = 4$ along the horizontal dimension and $L_2 = 3$ along the vertical. The associated grating lobe structure of the individual sparse coset subarrays results in the two-dimensional scene being represented as divided into twelve sectors.

Roughly speaking, the array sparsity along each dimension yields a multiplicative benefit in the planar array case. As a result, the overall reduction in the number of elements is notably more abundant than for the linear array. In addition, the planar multi-coset array retains the ability to exploit range-dependent sparsity to achieve even further sparsity improvements.

Beyond the structure described above, in which both the underlying lattice and the recurrent coset pattern are rectangular, it should be possible to formulate the reconstruction algorithm for any geometry fitting the two-dimensional tiling structure. In particular, it is of interest to examine the use of the hexagonal, or equilateral-triangular lattice, commonly utilized in uniform planar arrays due to a grating lobe design condition resulting in a reduction in the number of elements by a factor of 15% compared with the rectangular geometry [63]. A simple example can be seen in Figure 9-5, in which the array Figure 9-4 is mapped onto the hexagonal lattice. This mapping implies a simple extension of

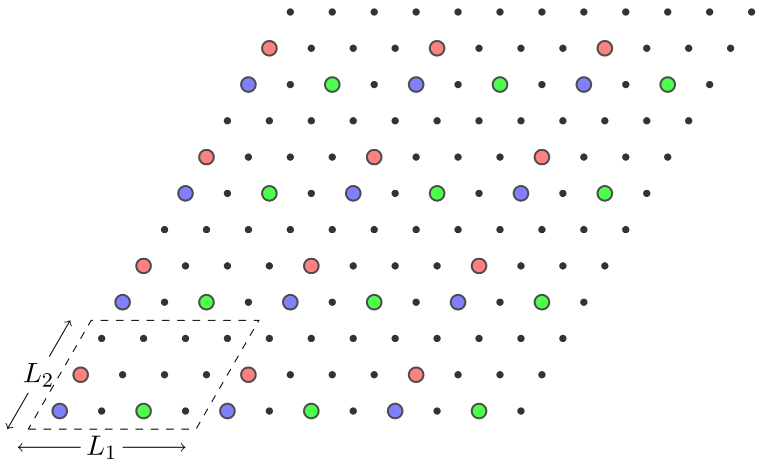

Figure 9-5: Planar multi-coset array on hexagonal lattice.

the processing technique for this geometry, yet a more complete analysis is warranted to determine what, if any, modifications to the design rules of the rectangular multi-coset array are necessary here. Ultimately, it should be determined whether the element reductions inherent in the uniform hexagonal geometry carry over to the multi-coset array.

9.4.2 Multi-coset MIMO radar

The type of imaging radar discussed in this thesis can be described as a *single-input multiple-output* (SIMO) system. In Figure 9-6a, the single-input takes the form of the red element which transmits some signal S_0. When this signal scatters off an object, the reflected signals reach the three blue receive elements, where the unique propagation distances from the transmit element to each of the receive elements appear result in phases φ_0, φ_1, and φ_2 in the multiple-output response of the receive array.

An equivalent scenario occurs in the *multiple-input single-output* (MISO) system shown in Figure 9-6b. In this case, signals S_0, S_1, and S_2 are transmitted from elements arranged such that the propagation distances to the single receive antenna are equal to the distances in Figure 9-6a, yielding a single-output containing a superposition of the three signals with their corresponding phase shifts. If the S_i are chosen such that the individual signal can be disentangled at the receiver, the φ_i can be extracted, providing the same information as in the SIMO system. In this sense, the SIMO receive array is termed the *virtual array* equivalent to the MISO system.

The *multiple-input multiple-output* (MIMO) radar system makes it possible to extend the MISO concept to obtain equivalent virtual arrays of greater aperture lengths; see e.g. [64,65]. In the example MIMO system shown in Figure 9-7a, an additional receive element is placed a distance of three element spacings from the original receive element such that the multiple-output response contains the phases associated with the six unique transmit-receive paths. When properly disentangled, this system is equivalent to the SIMO system shown in Figure 9-7b.

In general, an $N = N_t + N_r$ element SIMO system comprised of $N_t = 1$ transmit and N_r receive elements forms a receive aperture of $N_tN_r = N_r = N - 1$ elements (the same result holds for the virtual receive aperture in the N element MISO system), while the

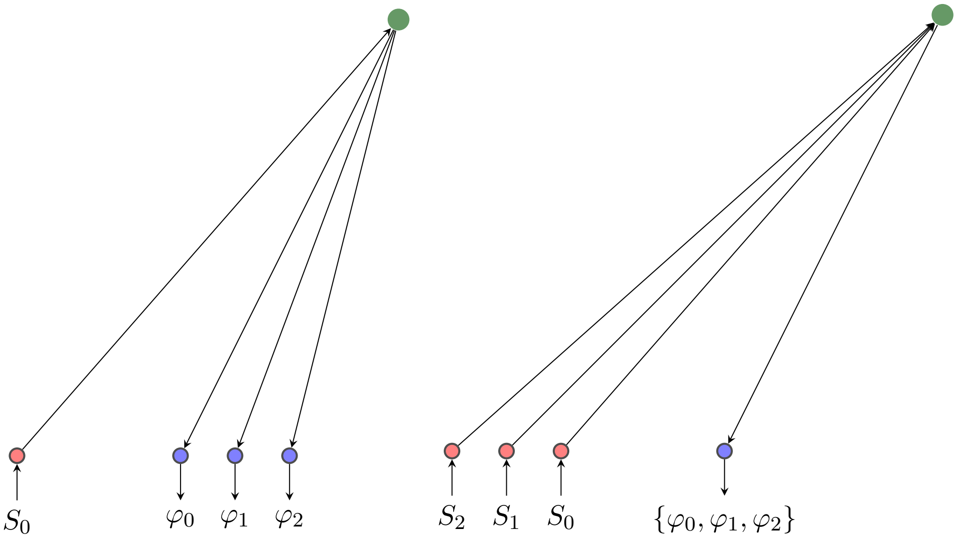

(a) SIMO (b) MISO

Figure 9-6: SIMO radar and equivalent MISO radar systems.

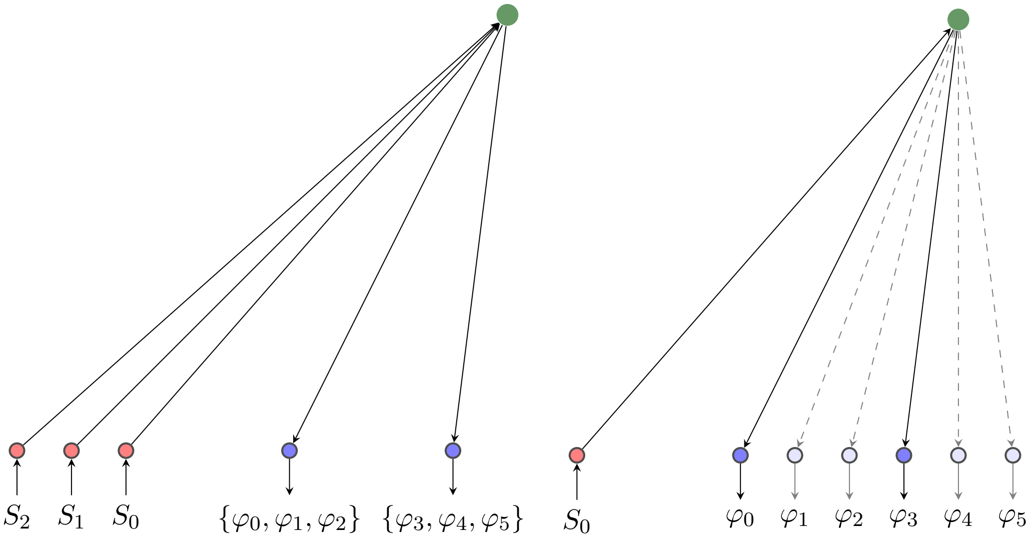

(a) MIMO (b) MIMO virtual equivalent

Figure 9-7: MIMO radar and equivalent virtual SIMO radar systems.

(a) MIMO multi-coset

(b) MIMO multi-coset virtual equivalent

Figure 9-8: MIMO radar and equivalent virtual MIMO equivalent.

Table 9.1: Total number of elements $N_t + N_r$ in the (SIMO) multi-coset and MIMO multi-coset systems for $M = 21$ coset periods of $L = 47$. Sparsity percentages shown in reference to total number of elements in the conventional SIMO system, $1 + ML = 988$.

Active Cosets, P	# multi-coset elements, $1 + MP$	# MIMO multi-coset elements, $P + M$
28	589 (60%)	48 (5.0%)
14	295 (30%)	35 (3.5%)
7	148 (15%)	28 (2.8%)
5	106 (11%)	26 (2.6%)

N element MIMO virtual array can contain up to $(N/2)^2$ elements. While the examples above concern only uniform arrays, the same principles apply whenever the spacing between receive elements is greater than the length of the transmit array[3]. This makes the use of MIMO radar especially appealing in the context of the multi-coset structure. Specifically, by designing the transmit array as a single coset pattern and the receive array as a sparse uniform array with a spacing given by the coset period, the resultant virtual array is an exact representation of a real multi-coset array, as seen in Figure 9-8. In Figure 9-8a, the red, blue, and green transmit elements are arranged according to the coset pattern $\mathcal{P} = \{0, 2, 6\}$, and the three receive elements are uniformly spaced by the coset period $L = 7$. In Figure 9-8b, we see the $N_t N_r = 9$ element virtual multi-coset receive array. In this example, the equivalent 10 element SIMO system is replaced by the 6 element MIMO system; and provided the transmitted waveforms are separable at the receiver, this data can be used in the exact manner as the SIMO multi-coset system.

This hybridization of the multi-coset and MIMO radar concepts has the potential of allowing significant additional array sparsity. As an example, Table 9.1 provides the element counts for the configurations used in the imaging results from Section 7.4. While these results highlight the remarkable possibilities of such a hybrid technique, additional research is necessary to ensure whether these system designs are tenable. Most importantly, the limiting factor is likely to be the maximum number of waveforms that can be reliably disentangled at the receiver, placing an upper limit on N_t. In addition, the multiple-input waveform design must be shown to be compatible with any other system requirements, such as the ability to perform pulse compression to allow range-dependent scene sparsity to be exploited.

---

[3] While other MIMO configurations may be used, these are not pertinent here.

9.4.3 Doppler-dependent sparsity

The idea of range dependent sparsity can be viewed more broadly as the sorting of the image data into a basis of orthogonal subsets. The disjoint nature of these subsets reframes the idea of angular sparsity to the occupancy level within each subset. This occupancy will be less than or equal to that of the entire data set, and conceivably, this reduction provides the ability to achieve a desirable level of array sparsity.

Another common radar use, Doppler radar, produces velocity data about target objects [66]. When a target moving with some radial velocity relative to the array is illuminated, the frequency of the reflected signal will exhibit a Doppler shift in proportion to this velocity. Upon receiving the reflected signals from some number of targets, the radar system distinguishes between the signal components having different Doppler frequencies, thus allowing the data to be sorted into separate velocity bins. As with the range sorting operation, each of these individual bins will possess a potentially lower occupancy and hence this provides a means of reducing the required multi-coset array density.

Pulse-Doppler radar allows the scene response to be sorted by *both* range and velocity. Application of this to the multi-coset array then redefines the appropriate definition of scene sparsity from the number of occupied sectors to the maximum number of sectors occupied by targets within the same range bin and moving at radial velocities relative to the array within the same Doppler bin. As a result, this has the potential to allow further reductions in the array element density.

Implementation of the joint range-velocity-dependent sparsity concept will require a thorough understanding of how such systems will be affected by *range-Doppler ambiguities.* This is a natural limitation of pulse Doppler radar that leads to a tradeoff in the fidelity of the range and velocity results. Hence, it is necessary to ensure that any advantages introduced by the use of velocity sorting are not outweighed by any losses due to compromises in the range sorting process. This entails an understanding of the appropriate waveform design tailored to the expected in situ characteristics of the scene.

Further questions arise regarding the significance of these Doppler ambiguities. The original intention of pulse-Doppler radar is to determine the velocity information in addition to the position of the targets, whereas here it is proposed as an additional tool for achieving improved array sparsity. Specifically, if the velocity data is not a desired output, it may be worthwhile to tolerate some presence of Doppler ambiguities rather than to sacrifice the range performance of the radar system.

Finally, it may be of advantage in certain situations to use the differential moving-target-indicator (MTI) radar approach [39] for distinguishing velocities. Rather than sorting responses into any number of velocity bins, as in the case of Doppler radar, this technique simply distinguishes between stationary and non-stationary targets. Though the potential benefits of this may be somewhat less than with Doppler radar, the computational complexities and ambiguity issues become less of a concern. Indeed, for applications in which targets that are stationary relative to the radar position are unimportant, the use of such differential cancellation techniques can be used to remove a great deal of targets and allow for a commensurately less dense multi-coset array.

Bibliography

[1] Boris Murmann, Christian Vogel, and Heinz Koeppl. Digitally enhanced analog circuits: System aspects. In *Circuits and Systems, 2008. ISCAS 2008. IEEE International Symposium on*, pages 560–563. IEEE, 2008.

[2] Saihua Lin, K.B. Ng, H. Wong, K.M. Luk, S.S. Wong, and A.S.Y. Poon. A 60GHz digitally controlled RF beamforming array in 65nm CMOS with off-chip antennas. In *Proc. IEEE Radio Frequency Integrated Circuits Symposium (RFIC)*, June 2011.

[3] H. Krishnaswamy, A. Valdes-Garcia, and Jie-Wei Lai. A silicon-based, all-passive, 60GHz, 4-element, phased-array beamformer featuring a differential, reflection-type phase shifter. In *Proc. IEEE Int. Symp. Phased Array Systems and Technology (ARRAY)*, pages 225–232, Oct. 2010.

[4] Dong Gun Kam, Duixian Liu, A. Natarajan, S. Reynolds, and B.A. Floyd. Low-cost antenna-in-package solutions for 60-GHz phased-array systems. In *Proc. IEEE Conf. Electrical Performance of Electronic Packaging and Systems (EPEPS)*, pages 93–96, Oct. 2010.

[5] A. Natarajan, A. Komijani, Xiang Guan, A. Babakhani, and A. Hajimiri. A 77-GHz phased-array transceiver with on-chip antennas in silicon: Transmitter and local LO-path phase shifting. *IEEE J. Solid-State Circuits*, 41(12):2807–2819, Dec. 2006.

[6] K. M. Nguyen, A. Accardi, G. W. Wornell, and C. G. Sodini. Digital phase tightening for millimeter-wave imaging. In *Proc. IEEE Custom Integrated Circuits Conf. (CICC)*, San Jose, CA, Sep. 2010.

[7] L. Khuon, E. W. Huang, C. G. Sodini, and G. W. Wornell. Integrated transceiver arrays for multiple antenna systems. In *Proc. Vehic. Technol. Conf. (VTC)*, Stockholm, Sweden, May 2005.

[8] M. Elkhouly, Chang-Soon Choi, S. Glisic, C. Scheytt, and F. Ellinger. Millimeter-wave beamforming circuits in SiGe BiCMOS. In *Proc. IEEE Bipolar/BiCMOS Circuits and Technology Meeting (BCTM)*, pages 129–132, Oct. 2010.

[9] Y. Sato, K. Fujita, H. Sawada, and S. Kato. Design and performance of beam-forming antenna with discrete phase shifter for practical millimeter-wave communications systems. In *Proc. Asia-Pacific Microwave Conference (APMC)*, pages 638–641, Dec. 2010.

[10] D. Ehyaie and A. Mortazawi. A new approach to design low cost, low complexity phased arrays. In *IEEE Int. Microwave Symposium (MTT-S) Digest*, pages 1270–1273, May 2010.

[11] S.R. Norsworthy, R. Schreier, and G.C. Temes. *Delta-Sigma Data Converters: Theory, Design, and Simulation.* IEEE Press, New York, NY, 1996.

[12] B. Almutairi and M. Kraft. Experimental study of single loop sigma-delta and multistage noise-shaping (MASH) modulators for MEMS accelerometer. In *Proc. IEEE Sensors*, pages 520–523, Oct. 2011.

[13] W. Almeida, G. Freitas, L. Palma, S. Catunda, R. Freire, H. Aboushady, F. Santos, and A. Oliveira. A constant temperature thermoresistive sigma-delta anemometer. In *Proc. Instrumentation, Measurement Technol. Conf. (IMTC)*, May 2007.

[14] S. Thoss, O. Machul, and B.J. Hosticka. A novel architecture for inductive proximity sensors using sigma delta modulation. In *Proc. European Solid State Circuits Conf. (ESSCIRC)*, pages 284–287, Sep. 2007.

[15] G.D. Altinok, M. Al-Janabi, and I. Kale. Improved sigma-delta ultrasound beamformers with adaptive low-pass decimation filters. In *Proc. IEEE Instrumentation, Measurement Technol. Conf. (IMTC)*, May 2011.

[16] H.S. Bilge and M. Karaman. Subarray delta-sigma beamforming for ultrasonic imaging. In *Proc. IEEE Ultrasonics Symp.*, volume 2, pages 1623–1626, Oct. 2002.

[17] P.M. Silva, V. Correia, S. Lanceros Mendez, and J.G. Rocha. Sigma-delta A/D converter for CMOS image sensors. In *Proc. Int. Conf. Microelectronics (ICM)*, pages 94–97, Dec. 2009.

[18] M. Kozak and M. Karaman. Digital phased array beamforming using single-bit delta-sigma conversion with non-uniform oversampling. *IEEE Trans. Ultrasonics, Ferroelectrics, Freq. Contr.*, 48(4):922–931, July 2001.

[19] H. Aomori, T. Otake, N. Takahashi, I. Matsuda, S. Itoh, and M. Tanaka. An oversampling 2D sigma-delta converter by cellular neural networks. In *Proc. IEEE Int. Symp. Circ., Syst. (ISCAS)*, pages 2566–2569, June 2010.

[20] T.D. Kite, B.L. Evans, A.C. Bovik, and T.L. Sculley. Digital halftoning as 2-D delta-sigma modulation. In *Proc. Int. Conf. Image Processing*, volume 1, pages 799–802, Oct. 1997.

[21] D.P. Scholnik, J.O. Coleman, D. Bowling, and M. Neel. Spatio-temporal delta-sigma modulation for shared wideband transmit arrays. In *Proc. IEEE Radar Conf.*, pages 85–90, April 2004.

[22] Y.T. Lo and S.W. Lee. *Antenna Handbook: Antenna Theory.* Van Nostrand Reinhold, New York, NY, 1993.

[23] Robert J Mailloux. *Phased array antenna handbook.* Artech House Boston, MA, 2005.

[24] J. S. Herd, S. M. Duffy, and H. Steyskal. Design considerations and results for an overlapped subarray radar antenna. In *Proc. IEEE Aerospace Conf.*, pages 1087–1092, 2005.

[25] R. O. Schmidt. Multipe emitter location and signal parameter estimation. *IEEE Trans. Antennas Propag.*, 34(3):276–280, Mar. 1986.

[26] Y. Kochman and G. W. Wornell. Finite multi-coset sampling and sparse arrays. In *Proc. ITA*, pages 1–7, La Jolla, CA, 2011.

[27] P. Pal and P. P. Vaidyanathan. Nested arrays: A novel approach to array processing with enhanced degrees of freedom. *IEEE Trans. Signal Process.*, 58(8):4167–4181, 2010.

[28] P. P. Vaidyanathan and P. Pal. Sparse sensing with co-prime samplers and arrays. *IEEE Trans. Signal Process.*, 59(2):573–586, 2011.

[29] P. Pal and P. P. Vaidyanathan. Coprime sampling and the MUSIC algorithm. In *Proc. IEEE Digital Signal Processing, Signal Processing Education Workshop (DSP/SPE)*, pages 289–294, 2011.

[30] S. Shakeri, D. D. Ariananda, and G. Leus. Direction of arrival estimation using sparse ruler array design. In *Proc. IEEE Workshop on Signal Processing Advances in Wireless Communications (SPAWC)*, pages 525–529, 2012.

[31] M. E. Dominguez-Jimenez, N. Gonzalez-Prelcic, G. Vazquez-Vilar, and R. Lopez-Valcarce. Design of universal multicoset sampling patterns for compressed sensing of multiband sparse signals. In *Proc. IEEE Int. Conf. Acoustics, Speech, Signal Process. (ICASSP)*, pages 3337–3340, 2012.

[32] D. Romero and G. Leus. Compressive covariance sampling. In *Proc. Information Theory and Applications Workshop (ITA)*, La Jolla, CA, 2013.

[33] E. J. Candes and M. B. Wakin. An introduction to compressive sampling. *IEEE Signal Process. Mag.*, 25(2):21–30, 2008.

[34] D.L. Donoho. Compressed sensing. *IEEE Trans. Inf. Theory*, 52(4):1289–1306, 2006.

[35] P. Feng and Y. Bresler. Spectrum-blind minimum-rate sampling and reconstruction of multiband signals. In *Proc. ICASSP*, volume 3, pages 1688–1691, Atlanta, GA, 1996.

[36] J.A. Kong. *Electromagnetic Wave Theory.* Higher Education Press, 2002.

[37] D. M. Pozar. *Microwave Engineering.* J. Wiley, India, 2005.

[38] I. Gupta and A. Ksienski. Effect of mutual coupling on the performance of adaptive arrays. *Antennas and Propagation, IEEE Transactions on*, 31(5):785–791, 1983.

[39] Merrill Ivan Skolnik. Radar handbook. 1970.

[40] H. L. Van Trees. *Optimum Array Processing (Detection, Estimation, and Modulation Theory, Part IV).* Wiley-Interscience, New York, NY, 2002.

[41] R. C. Hansen. *Phased Array Antennas.* Wiley Interscience, 2009.

[42] Alan V Oppenheim, Ronald W Schafer, John R Buck, et al. *Discrete-time signal processing*, volume 5. Prentice Hall Upper Saddle River, 1999.

[43] W. Wasylkiwskyj and W. Kahn. Theory of mutual coupling among minimum-scattering antennas. *IEEE Trans. Antennas, Propagation*, 18(2):204–216, 1970.

[44] Roger A Horn and Charles R Johnson. *Matrix analysis.* Cambridge university press, 2012.

[45] M. Mishali and Y. C. Eldar. Blind multiband signal reconstruction: Compressed sensing for analog signals. *IEEE Trans. Signal Process.*, 57(3):993–1009, 2009.

[46] J. Chen and X. Huo. Theoretical results on sparse representations of multiple-measurement vectors. *Signal Processing, IEEE Transactions on*, 54(12):4634–4643, 2006.

[47] S.F. Cotter, B.D. Rao, K. Engan, and K. Kreutz-Delgado. Sparse solutions to linear inverse problems with multiple measurement vectors. *Signal Processing, IEEE Transactions on*, 53(7):2477–2488, 2005.

[48] Kiryung Lee and Y. Bresler. Subspace-augmented MUSIC for joint sparse recovery with any rank. In *Proc. IEEE Workshop on Sensor Array, Multichannel Signal Process. (SAM)*, pages 205–208, 2010.

[49] M. E. Davies and Y. C. Eldar. Rank awareness in joint sparse recovery. *IEEE Trans. Inf. Theory*, 58(2):1135–1146, 2012.

[50] J. M. Kim, O. K. Lee, and J.-C. Ye. Compressive MUSIC: Revisiting the link between compressive sensing and array signal processing. *IEEE Trans. Inf. Theory*, 58(1):278–301, 2012.

[51] J. A. Tropp, A. C. Gilbert, and M. J. Strauss. Algorithms for simultaneous sparse approximation. Part I: Greedy pursuit. *Signal Processing*, 86(3):572–588, 2006.

[52] J. A. Tropp. Algorithms for simultaneous sparse approximation. Part II: Convex relaxation. *Signal Processing*, 86(3):589–602, 2006.

[53] D. Johnson and S. DeGraaf. Improving the resolution of bearing in passive sonar arrays by eigenvalue analysis. *IEEE Trans. Acoust., Speech, Signal Process.*, 30(4):638–647, 1982.

[54] A. Moffet. Minimum-redundancy linear arrays. *IEEE Trans. Antennas Propag.*, 16(2):172–175, 1968.

[55] S. Kirkpatrick, C. D. Gelatt, and M. P. Vecchi. Optimization by simulated annealing. *Science*, 220:671–680, 1983.

[56] A.F. Yegulalp. Fast backprojection algorithm for synthetic aperture radar. In *Radar Conference, 1999. The Record of the 1999 IEEE*, pages 60–65, 1999.

[57] T. T. Taylor. One parameter family of line-sources producing modified sin $(\pi u)/\pi u$ patterns. *Hughes Aircraft Co. Tech. Mem*, 324, 1953.

[58] T. T. Taylor. Design of line-source antennas for narrow beamwidth and low side lobes. *Antennas and Propagation, Transactions of the IRE Professional Group on*, 3(1):16–28, 1955.

[59] Hamid Krim and Mats Viberg. Two decades of array signal processing research: the parametric approach. *Signal Processing Magazine, IEEE*, 13(4):67–94, 1996.

[60] Alan Edelman and N Raj Rao. Random matrix theory. *Acta Numerica*, 14(1):233–297, 2005.

[61] Y. Bresler and Ping Feng. Spectrum-blind minimum-rate sampling and reconstruction of 2-d multiband signals. In *Image Processing, 1996. Proceedings., International Conference on*, pages 701–704 vol.1.

[62] R. Venkataramani and Y. Bresler. Further results on spectrum blind sampling of 2d signals. In *Image Processing, 1998. ICIP 98. Proceedings. 1998 International Conference on*, pages 752–756 vol.2.

[63] E. Sharp. A triangular arrangement of planar-array elements that reduces the number needed. *Antennas and Propagation, IRE Transactions on*, 9(2):126–129, 1961.

[64] Keith W Forsythe and Daniel W Bliss. Mimo radar: Concepts, performance enhancements, and applications. *MIMO Radar Signal Processing, J. Li and P. Stoica, Eds*, pages 65–121, 2008.

[65] Jian Li and Petre Stoica. *MIMO radar signal processing*. Wiley-IEEE Press, 2008.

[66] Edward J Barlow. Doppler radar. *Proceedings of the IRE*, 37(4):340–355, 1949.